UV laser modification of transparent materials for photonic applications

Dissertation
for the award of the degree
"Doctor rerum naturalium" (Dr. rer. nat.)
of the Georg-August-Universität Göttingen

within the doctoral program Physics
of the Georg-August University School of Science (GAUSS)

submitted by

Lukas Janos Richter

from Henstedt-Ulzburg

Göttingen, 2023

Thesis Committee

Prof. Dr. Hans Christian Hofsäss, II. Institute of Physics, Georg-August-Universität Göttingen, Germany

Dr. Jürgen Ihlemann, Short Pulses / Nanostructures, Institut für Nanophotonik Göttingen e.V., Germany

Prof. Dr. Michael Seibt, IV. Institute of Physics, Georg-August-Universität Göttingen, Germany

Members of the Examination Board

Reviewer: Prof. Dr. Hans Christian Hofsäss, II. Institute of Physics, Georg-August-Universität Göttingen, Germany

Second Reviewer: Dr. Jürgen Ihlemann, Short Pulses / Nanostructures, Institut für Nanophotonik Göttingen e.V., Germany

Further members of the Examination Board:

Prof. Dr. Alexander Egner, Institut für Nanophotonik Göttingen e.V., Göttingen, Germany

Prof. Dr. Vasily Moshnyaga, I. Institute of Physics, Georg-August-Universität Göttingen, Germany

Prof. Dr. Angela Rizzi, IV. Institute of Physics, Georg-August-Universität Göttingen, Germany

Prof. Dr. Michael Seibt, IV. Institute of Physics, Georg-August-Universität Göttingen, Germany

Date of the oral examination: 21.04.2023

Abstract

Photonic applications have experienced strong growth in recent years. Due to increasing digitalization and automation in all areas of life, further growth of photonics is expected in the future. The broad range of photonic applications supports this statement. While photonic applications used to be dominated by telecommunication through optical fibers, the use of photonic processes today is manifold. For example, new light sources have been developed in the form of LEDs (light-emitting diodes) or OLEDs (organic light-emitting diodes). Due to the ability to emit coherent and intense light, lasers (light amplification by stimulated emission of radiation) play a key role as a light source in photonics. In materials processing, for example, lasers enable the structuring or surface modification of materials. Lasers are also used in other areas of photonics. For all these applications, optically transparent materials are indispensable. From the design of a laser up to the optics for beam shaping, transparent materials are required. These are usually glasses, but can also be crystals, ceramics or polymers. In this thesis the modification of transparent materials by lasers is addressed. Glasses and amorphous thin films are structured and functionalized with UV lasers. Single pulse or repetitive laser heating with high spatial resolution enables processes which cannot easily be accomplished by other methods.

In the first part of the thesis an introduction to the relevant parts of photonics is provided. The basics of laser materials processing, e. g. laser ablation, are explained in section 1.1. Examples of laser materials processing are introduced and important experimental parameters for these applications are explained. In section 1.2, aspects of laser functionalization of surfaces are discussed. To that end an introduction to relevant physical properties of transparent materials is given. Subsequently an overview of laser-based implantation of metal nanoparticles in glass and laser marking of glass surfaces by several methods is presented. The last part of the introduction, section 1.3, deals with silicon photonics. The band structures of bulk silicon and silicon nanocrystals are explained and the resulting optical properties are discussed. A literature review on this topic is provided. At the end of this chapter, the references of the introduction are provided.

In chapter 2, the manuscripts of this cumulative dissertation are presented. In the first manuscript (section 2.1), the generation of a black marking on titanium oxide containing glass by ultraviolet (UV) excimer laser irradiation is presented. The black marking is partly caused by strong scattering by a microstructure on the glass surface. The laser-induced microstructure is accompanied by the formation of a titanium-rich and a silicon-rich phase on the glass surface. A further contribution to the black marking can be attributed to an increased absorption caused by an oxygen reduction of the titanium oxide. By this technique, for example, informative markings such as QR codes can be applied to the glass surface. The process of the fabrication of the marking as well as material analyses are presented. The other two manuscripts deal with silicon photonics. In section 2.2, a method for photoluminescence enhancement of silicon nanocrystals inside a silicon suboxide matrix by laser-based implantation of gold nanoparticles is presented. The results of photoluminescence measurements are discussed with the help of absorption, Raman and scanning electron

microscopy measurements. A coupling of the silicon nanocrystals to the plasmonically active gold nanoparticles leads to an enhancement of the photoluminescence. The third manuscript in section 2.3 also deals with the enhancement of photoluminescence of silicon nanocrystals by UV excimer laser-based methods. Laser irradiation of a silicon suboxide surface leads to an enhancement of the photoluminescence. The effects of laser irradiation on the silicon nanocrystals in the silicon suboxide matrix are analyzed by Raman spectroscopy and transmission electron microscopy, among others. Besides a slight photoluminescence enhancement due to structural changes of the silicon nanocrystals, there is an enhancement of the photoluminescence due to a reduction of losses caused by total internal reflection in the highly refractive silicon suboxide layer.

A summary and a discussion of the presented results is given in chapter 3. The chapter is divided into the two main topics of laser-based glass marking (section 3.1) and silicon photonics (section 3.2). For this section, the relevant literature is again provided at the end of the section.

Contents

1. Introduction 8

1.1 Laser materials processing 8
1.1.1 Light absorption 8
1.1.2 Laser ablation 10
1.1.3 Influence of the laser pulse length 10
1.1.4 Laser ablation with UV excimer lasers 12

1.2 Laser functionalization of surfaces 13
1.2.1 Transparent materials 13
1.2.2 Metal nanoparticle implantation in transparent materials 17
1.2.3 Glass marking by lasers 20

1.3 Silicon photonics 22
1.3.1 Silicon bandgap 23
1.3.2 Silicon nanocrystals 24

1.4 References of the Introduction 34

2. Manuscripts 42

2.1 UV laser generated micro structured black surface on commercial TiO_2-containing glass 43

2.2 Photoluminescence enhancement of silicon nanocrystals by excimer laser implanted gold nanoparticles 53

2.3 Excimer laser surface patterning for photoluminescence enhancement of silicon nanocrystals 62

3 Summary & Discussion 85

3.1 Laser marking of TiO_2 containing glass 85

3.2 Photoluminescence enhancement of silicon nanocrystals 86

3.3 References of the Discussion 89

Acknowledgements 90

Curriculum vitae 91

1. Introduction

The 20th century was marked by an unprecedented development, that of electronics. It was a long way from the first programmable computer, invented by Konrad Zuse in 1941, to modern silicon-based microelectronics on the nanometer scale [1]. The 21st century will be marked by a new key technology: That of photonics. This field was paved by the development of the first laser in 1960 [2 p. 22]. The development of the first LED and optical fibers for information transmission greatly expanded the field of photonics. Today, the field of photonics is still growing rapidly. Major fields include: Laser manufacturing, sensing applications, data transmission, biophotonics and display technology. As a result, photonics applications accompany us through our everyday lives and have become an indispensable part of industry and research.

In this thesis the focus lies on laser materials processing. This field includes, among others, the laser processes of ablation, melting, welding, cutting or pulsed laser deposition (PLD). Here, the sub-areas of surface functionalization and micro- and nanostructuring of transparent materials is treated. This implies the fabrication of structures on material surfaces with lateral structure sizes ranging from one millimeter to several hundred nanometers and heights of a few micrometers and smaller by pulsed laser irradiation. The basic physical processes of laser material structuring are explained in the following section.

1.1 Laser materials processing

1.1.1 Light absorption

The interaction of light with solid state material depends on the absorption of light. For a homogeneous medium, the material- and wavelength-dependent absorption coefficient "α" defines the absorption. It can be calculated by the imaginary part of the complex refractive index "κ" and the wavelength "λ_0" [3 p. 221]:

$$\alpha = \frac{4\,\pi\,\kappa}{\lambda_0} \tag{1}$$

In general, the attenuation of radiation as it traverses a medium can be described by the Lambert-Beer law. The drop in intensity "I" after a depth "z" is given by the differential equation [3 p. 221]:

$$\frac{dI}{dz} = -\alpha\, I \tag{2}$$

The solution is an exponential decay function with initial Intensity "I_0":

$$I(z) = I_0 \cdot e^{-\alpha z} \tag{3}$$

However, the Lambert-Beer law only holds for linear processes and loses its validity in this form for multiphoton absorption. Since multiphoton absorption is not discussed in this work, a more detailed description of this process is omitted.

There are several reasons for light absorption in solid state material. Dominant in many cases is the interaction of photons with electrons. However, also other processes, like the interaction of photons with phonons, can contribute to light absorption. For metals the photon absorption can be described by the interaction of photons with free electrons. As no metal processing is treated in this thesis, this will not be further explained. For solid state materials with a bandgap, like semiconductors or isolators, the photon energy $\mathrm{E_{ph}} = \mathrm{h} \cdot \mathrm{f}$ (“h” and “f” denote the Planck constant and the frequency, respectively) and the electronic band structure, i. e. the bandgap “$\mathrm{E_g}$”, of the material are the decisive properties for light absorption. In simple terms, for a photon to excite an electron from the valence band to the conduction band, i. e. an interband transition, the energy of the photon must exceed the bandgap:

$$\mathrm{E_{ph}} \geq \mathrm{E_g} \tag{4}$$

Hereby the photon is absorbed and induces a non-equilibrium electronic distribution. Via electron-phonon or electron-electron interactions the energy is converted into thermal energy in the material [2 p. 23]. The transition probability rates for the interband transition of an electron by photon absorption can be calculated by Fermi´s golden rule. Detailed calculations can be found in many textbooks. An important result is the dependency of the optical absorption coefficient on the energy difference between the photon energy and the bandgap of the material. For direct bandgap materials the absorption coefficient is proportional to the square root of the energy difference [4 p. 467]:

$$a_{dir} \propto \sqrt{\mathrm{E_{ph}} - \mathrm{E_g}} \tag{5}$$

For indirect bandgap materials the optical absorption coefficient is proportional to the quadratic energy difference. The energy of a phonon “$\mathrm{E_{pn}}$” of proper momentum and energy has also to be taken into account using the Bose-Einstein distribution “$\mathrm{f_{BE}}$” [4 p. 468]:

$$a_{ind} \propto \mathrm{f_{BE}}\,(\mathrm{E_{ph}} - \mathrm{E_g} + \mathrm{E_{pn}})^2 + (1 - \mathrm{f_{BE}})\,(\mathrm{E_{ph}} - \mathrm{E_g} - \mathrm{E_{pn}})^2 \tag{6}$$

The absorption of photons by interaction with electrons thus depends mainly on the photon energy and the band structure of the material. A more detailed description of the difference between a direct and an indirect band gap will be explained later in section 1.3.1 using silicon as an example. At this point it should be noted that indirect bandgap materials absorb light less effectively than direct bandgap materials.

In practice, defects and impurities are crucial in the process of light absorption for many non-metal materials, since they have a significant influence on the band structure and thus often make the effective absorption of light possible in the first place [5 p. 196]. In experiments an enhanced absorption at the surface is measured compared to that of bulk material. This has several origins: On the one hand, defects occur at the interface between the solid and the air.

Furthermore, chemical impurities or physical imperfections at the surface increase the absorption [5 p. 196] [6].

1.1.2 Laser ablation

Sufficiently high energy deposition per time and volume in the material causes removal of the material. This process is called laser ablation. It is attributed to several factors. Such factors are, for example, laser-supported absorption waves, breaking of chemical bonds or recoil pressure effects [2 p. 21]. However, it is usually sufficient to assume an increased temperature as the cause. The increased temperature of the material can lead to a melting process or at even higher temperatures to a vaporization of the material. At high energy densities a plasma is formed on the surface. These processes can lead to a local removal of material, i. e. ablation. To reach the necessary energy densities in the material, the energy transfer from the light to the material has to be sufficient. In practical applications this can be reached by different methods. Theoretically, the easiest way would be to choose a sufficiently high laser fluence (energy per area) for materials processing. For almost perfectly transparent materials very high fluences would be necessary. This leads to practical problems, since the available laser power is naturally limited. Therefore, in practice, other experimental parameters must be selected for laser ablation. On the one hand, very short light pulses (femtoseconds) can be used. This leads to a very high-power density for a short time and can induce nonlinear processes, such as multiphoton absorption. Another possibility is to vary the laser wavelength. Materials that are optically transparent in the visible spectrum, such as glass, are often highly absorbent in the ultraviolet (UV) range. These materials can be processed much more easily with a UV laser than with a laser in the visible spectrum. UV lasers have the additional advantage that the achievable structure sizes due to the diffraction limitation are smaller than those of visible or infrared (IR) lasers. Ultra-short pulse lasers (femtoseconds regime) or pulsed UV lasers, such as excimer lasers, are therefore commonly used for the micro- and nanostructuring of solids. Besides absorption, the thermal conductivity of a material is an important property in laser processing to achieve sufficiently high local energy deposition. The thermal diffusion length “z_{th}” is proportional to the root of the laser pulse length “τ” and material constants “C” (thermal diffusivity) [2 p. 29] [7 p. 21]:

$$z_{th} = \sqrt{\tau \cdot C} \tag{7}$$

The pulse duration of the laser is therefore an important criterion in materials processing. Since the pulse length of excimer lasers (nanoseconds) is different from the pulse length of femtosecond lasers, there are significant differences in materials processing. These will be explained in the following.

1.1.3 Influence of the laser pulse length

Ablation with femtosecond (fs) laser pulses can be described as a direct solid-vapor transition [8]. As the thermal relaxation of the electrons is in the picosecond range, the ablation takes place after the absorption of the laser pulse is completed. Therefore, thermal conduction is negligible and the energy input is highly localized (cf. equation (7)). This is schematically sketched in the top row of Figure 1. In the first image the fs laser pulse hits the material surface. In a time-scale of nanoseconds (ns), i. e. significantly after the arrival of the laser

pulse, the affected material vaporizes, as can be seen in the second image. In the resulting structure the heat-affected zone and the molten area are very limited (third image). The fourth image shows a scanning electron microscope (SEM) image of a steel foil structured with a 200 fs laser pulse [8]. The resulting structure shows clear edges, although the thermal conductivity of steel is high. This becomes particularly clear in comparison to the processing of the same sample with ns laser pulses. This process is shown in the lower part of Figure 1. Due to the longer pulse duration, material ablation already occurs during the impact of one laser pulse. This is indicated in the second image. Parts of the incoming laser pulse are shielded by the already ablated material (plasma shielding). As the thermal relaxation is faster than the pulse length, the heat-affected zone is much larger than the ablated material. Beyond that, only the material that reaches the vaporization temperature evaporates. Since the melting temperature is significantly lower than this, a considerable part of the material is merely melted. This can also be seen in the SEM image. Again, a steel foil was structured. Here, laser pulses of 3.3 ns length were used [8]. It can be clearly seen that the non-ablated material is also affected. Melting edges have formed around the structure.

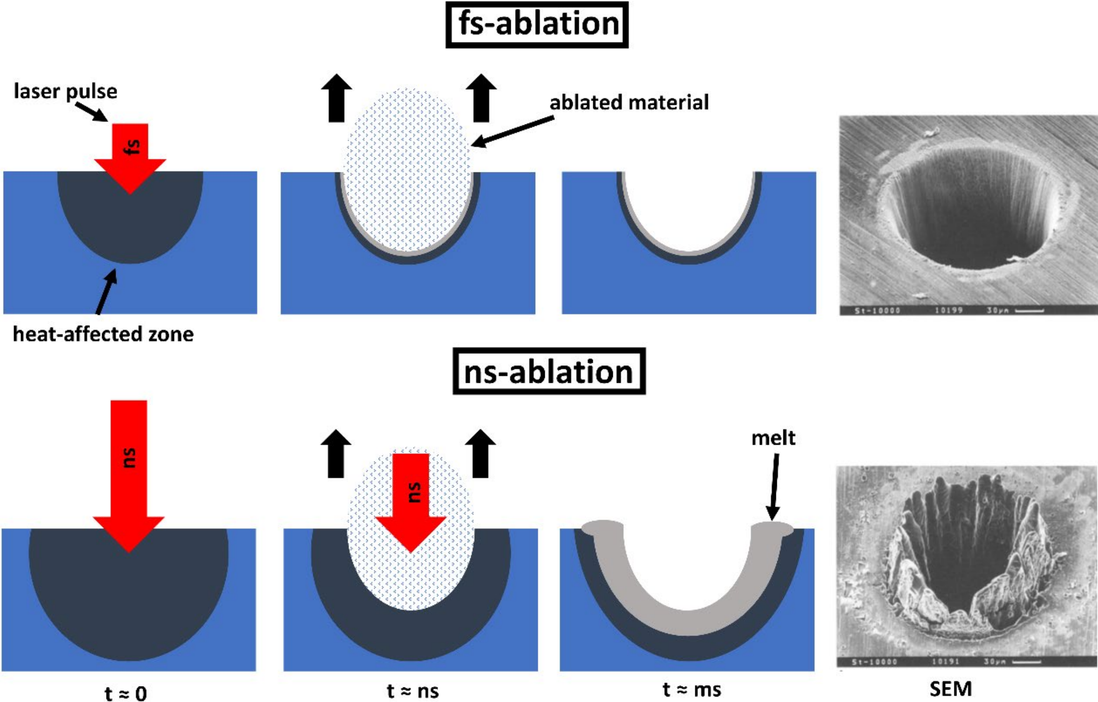

Figure 1 Schematic representation of the time progression of materials processing with an fs and an ns laser pulse. Exemplary SEM images of a steel foil are shown in each case. The schematic sketch is self-made, the SEM pictures are from [8].

It is therefore evident that the laser pulse duration has a significant influence on the resulting structure. Structuring with fs laser pulses ensures instant vaporization of the material, which also enables the processing of materials with high thermal conductivity, such as metals. In contrast, a ns laser pulse causes the material to heat up. As a result, the heat-affected zone significantly exceeds the ablated area. This is especially disadvantageous for the structuring of metals. However, an ns laser pulse, on the other hand, enables other applications that are not possible with fs laser pulses. An overview of such applications with ns laser pulses will be given

in the following. The focus will be on the widely used UV excimer lasers. These lasers have a typical pulse duration of 20 ns.

1.1.4 Laser ablation with UV excimer lasers

A detailed description of the operation principle of excimer lasers is omitted here. These are described in detail in the literature. In summary, these gas lasers generate laser pulses with typical pulse lengths around 20 ns at UV wavelengths of $\lambda = 157$ nm, 193 nm, 248 nm or 308 nm, achieving high absorption coefficients in many materials transparent in the visible range. The ablation rate per laser pulse is determined by the laser fluence "ϕ", i. e. the energy per area. To achieve substantial material ablation, a certain threshold fluence "ϕ_{th}" must be reached. Increasing the laser fluence above the threshold value increases the ablation rate per laser pulse. To specify material properties regarding the ablation behavior, the so-called effective absorption coefficient "α_{eff}" is often used [9]. It is assumed that with each laser pulse material is ablated up to the depth "d" until the fluence drops below the threshold fluence. According to equation (3) the ablation depth is calculated by the formula [9]:

$$d = \alpha_{eff}^{-1} \ln(\phi/\phi_{th}) \tag{8}$$

Since silicon suboxide (SiO_x, x ≈ 1) is used in this thesis later on, experimental data on the ablation behavior of this material is shown in Figure 2 [9]. Here, the ablation rate of SiO_x is plotted against the laser fluence for the excimer wavelengths $\lambda = 193$ nm, 248 nm and 308 nm. A clear rise in the ablation rate is evident for higher fluences. The trend is logarithmic, as stated in equation (8). For high fluences, the increase of the ablation rate turns into saturation. Here, processes such as the shielding of the laser pulse by the resulting plasma at the surface dominate. Overall, ablation rates of roughly 100 nm/laser pulse result for SiO_x at moderate fluences for these excimer wavelengths. The thermal diffusion length of SiO_x was calculated using equation (7) and is approximately 170 nm [9]. For other materials, of course, different thermal diffusion lengths and ablation rates result.

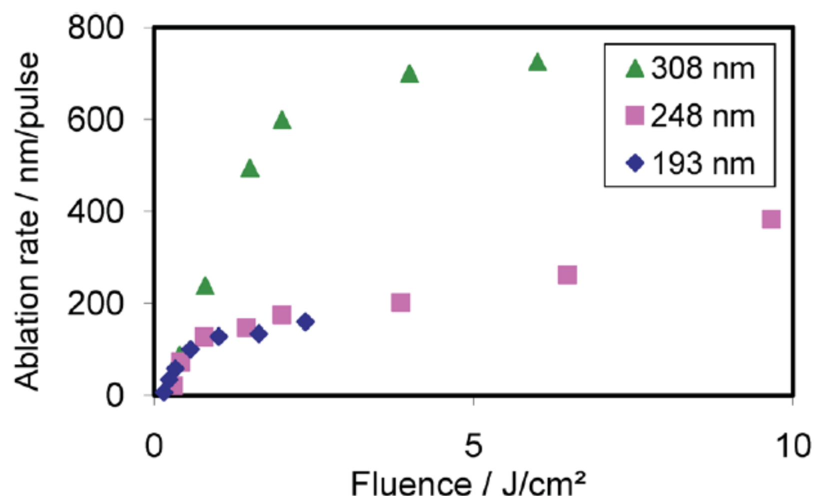

Figure 2 Ablation rate of SiO_x as a function of laser fluence for excimer wavelengths 193 nm, 248 nm and 308 nm. [9]

Alternative methods have also been developed for excimer laser processing of materials with low absorption coefficients. This makes it possible, for example, to ablate silicon dioxide

(SiO_2). This material is suitable for many applications due to its high transmission from UV to IR. At the same time, this property makes laser ablation considerably more difficult. The utilization of other materials nevertheless enables the structuring of such transparent materials. An example is the usage of a plasma generated from a laser irradiated metal sample for material removal from SiO_2 [10]. This process is called "laser-induced plasma assisted ablation" (LIPAA). Other techniques use the addition of highly absorbing materials, like polymers, to increase the absorption on the sample surface. An example is "laser-induced backside wet-etching" (LIBWE) [11]. Other methods include techniques like "laser etching at a surface adsorbed layer" (LESAL) [12] or "laser-induced backside dry etching" (LIBDE) [13]. The fabrication of microstructures in SiO_2 is also possible by another technique. The much higher absorption coefficient of SiO_x is used for laser structuring in this process. After the structurization of SiO_x it can then be converted to SiO_2 by thermal oxidation [14]. For example, SiO_2 multi-level phase elements have been produced with roughnesses of 3 nm [15].

1.2 Laser functionalization of surfaces

Lasers can also be used for the functionalization of surfaces. The fields of application are manifold. Examples can be found in microfluidics [16], in polishing or roughening of surfaces [17] [18], in coating technology [19] or in oxidation processes [20]. It is also known that ns laser pulses can introduce stress into glass. This can be used to develop methods for figure correction [21]. Two other applications will be discussed in more detail below, since parts of the manuscripts of this thesis involve these functionalizations. These are the implantation of metal nanoparticles in transparent materials and the marking of glass surfaces. Since both applications refer to transparent materials, an overview of this topic is given first.

1.2.1 Transparent materials

Transparent materials, as the name suggests, are characterized by high optical transmission. This usually refers to transmission in the visible spectrum, but of course spectral ranges outside the visible spectrum are also relevant for applications. Transparent materials are mainly glasses, as we know them from everyday life. They are used in a variety of applications, from windows and displays to insulating layers in the semiconductor industry. In addition to glass, optical crystals, like BBO (beta barium borate) or LBO (lithium triborate), also exhibit high transmission and are used, for example, in nonlinear optics for frequency doubling. Polymers and ceramics can also exhibit high transmission. In the following, physical properties of transparent materials will be explained. Subsequently, glasses and silicon oxides will be discussed in more detail, since they are relevant to this dissertation.

1.2.1.1 Physical properties of transparent materials

In general, the optical transmission of solid-state materials is related to the electronic band gap. Metals, as electrical conductors, have free conduction electrons. This results in a high interaction between electrons and photons. As already explained in section 1.1.1, this leads to high absorption. Semiconductors do not have free conduction electrons but have a relatively small band gap, like 1.12 eV for silicon or 1.42 eV for gallium arsenide [5 pp. 360-361]. Photons with higher energy than the bandgap can excite electrons for an interband transition and can thus be absorbed (see equation (4)). Insulating materials, such as glass, have a significant higher band gap, like 4.4 eV for borosilicate glass or 7.5 eV for fused silica

[22 p. 179]. This means that interband transitions of electrons by photon absorption are not possible except at high photon energies, resulting in high transmission over a wide spectral range.

The thermal properties of a material are related to its band structure. In a solid, heat transport takes place on the one hand through lattice vibrations (phonons). If free conduction electrons are present, as in metals, these also contribute to heat transport. This means that high electrical and thermal conductivity are linked. For metals, this is also known as the Wiedemann-Franz law [3 p. 47]. Electrical insulators with high optical transparency, such as glasses, have often significantly lower thermal conductivity than opaque materials, such as metals. As shown in section 1.1.3, this is decisive for the laser ablation of a material. For the laser ablation of transparent materials, the heat diffusion is therefore often less decisive than for metals.

In summary, high absorption is usually accompanied by high thermal conductivity. This is true for metals. High transmission, as in the case of glasses, is also associated with low thermal conductivity and high electrical insulation. It should be noted, however, that there are also exceptions. Diamond, for example, has a very high thermal conductivity, but is an electrical insulator. This is caused by the large phonon mean free path [23]. Materials with high electrical conductivity without significant thermal conductivity, however, are difficult to realize because of the contribution of free conduction electrons to thermal conductivity.

Besides optical properties, thermal and mechanical properties of transparent materials are decisive for many applications. Ceramics and silicate glasses, for example, are characterized by significantly higher melting temperatures compared to soda-lime glasses. This limits the range of application of soda-lime glasses. For materials processing with lasers, the thermal expansion of a material is important. In materials with a high thermal expansion coefficient, cracks easily form during heating and subsequent cooling. This aspect must therefore also be taken into account in certain applications. The use of transparent materials in chemistry also makes chemical resistance an important criterion.

1.2.1.2 Glasses

The most commonly used transparent materials are glasses. Since they are also used in this work, glasses will be discussed in more detail here. Glasses are amorphous solids produced by rapid cooling of a glass melt. The high cooling rate prevents crystallization of the material. This results in the same chemical bonding as in crystals, but there is no long-range periodicity as with crystals. This is shown in Figure 3 using the example of silicon oxide, on which many glasses are based [24 p. 42]. In silicon oxide four oxygen atoms and one silicon atom form $\mathrm{SiO_4}$ tetrahedrons. These form a network with each other. Each silicon atom is bonded to four oxygen atoms and each oxygen atom is bonded to two silicon atoms. This results in a composition of $\mathrm{SiO_2}$ [22 pp. 5,22]. In part a) of Figure 3 crystalline quartz is depicted. The crystalline periodic structure is preserved on large length scales. In part b) quartz glass is depicted. It exhibits the same chemical bonds as crystalline quartz without showing a long-range periodic structure.

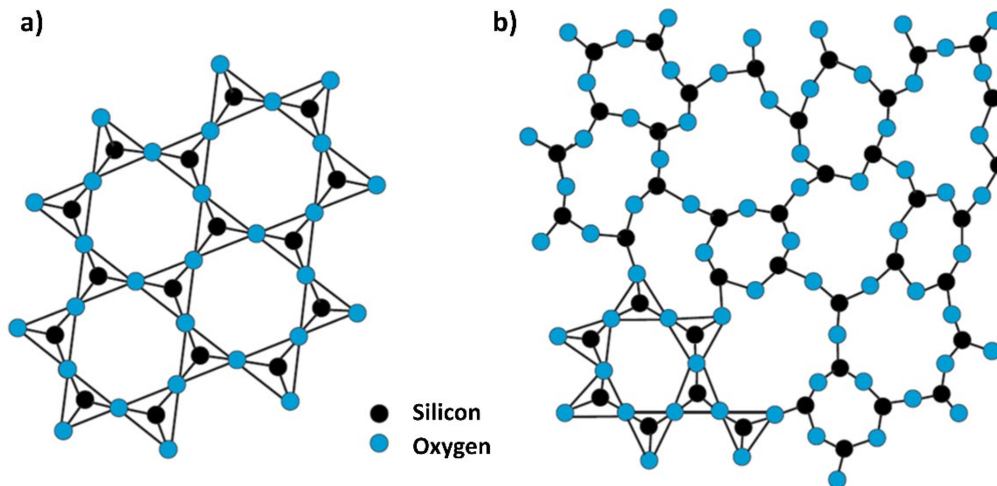

Figure 3 Schematic structure of SiO_4 tetrahedrons in a) crystalline quartz and b) amorphous quartz glass. Crystalline quartz has an ordered periodic structure while amorphous quartz glass has locally the same bonds but without a periodic structure on large length scales. Image modified after [24 p. 42].

Besides silicon oxide, other components are also added in glasses. Depending on the desired properties of the glass, different compositions are used. For example, sodium carbonate (Na_2CO_3), boron trioxide (B_2O_3) or lead oxide (PbO) are added [22 pp. 29-30]. In this way, properties such as the melting point, the mechanical properties or the refractive index can be adjusted. Since glass with titanium oxide components is used in parts of this work, titanium oxide will be discussed in more detail.

1.2.1.3 Titanium oxide glass

Titanium oxide is primarily known for its photocatalytic properties [25]. For example, it is used as a coating for window panes for a self-cleaning effect [26]. However, it is also used as an additive in glasses. In the past, lead oxide was added to glasses to increase the refractive index [24 p. 43]. Because of the harmful properties of lead oxide for health and environment, the addition is now largely avoided. Instead, titanium oxide is often used. Titanium dioxide's high refractive index (approximately 2.6 in the visible spectrum) also leads to a high refractive index when added to glass [27]. This is shown in Figure 4 [28]. The refractive index for various glass mixtures is plotted against the TiO_2 concentrations. A clear increase in the refractive index for higher TiO_2 concentrations can be measured.

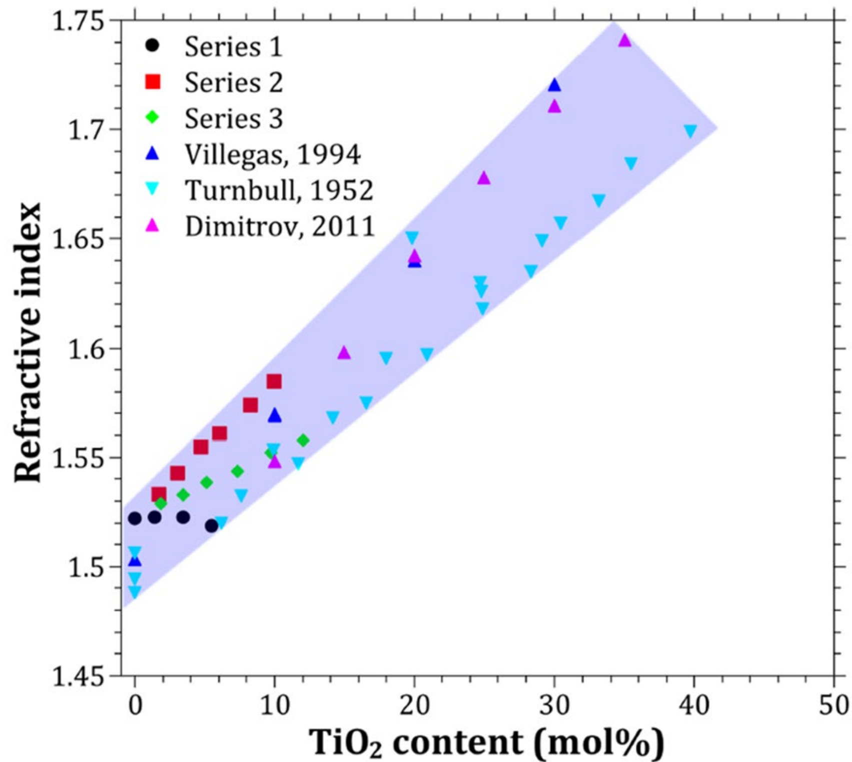

Figure 4 The refractive index is plotted against the TiO_2 concentration for different glass mixtures. An increase in the refractive index for higher TiO_2 content is measured. Image modified after [28].

Titanium dioxide occurs mainly in the rutile and anatase phases, with band gaps of 3.03 eV and 3.2 eV, respectively [29]. Since this thesis deals with laser processing, an overview of laser processing of titanium oxide and glasses containing titanium oxide is presented.

The formation of rutile titanium dioxide in glass (containing 20 mol % TiO_2) was observed by femtosecond laser irradiation. It was possible to write continuous lines or periodic structures of rutile phase in the glass bulk [30] [31]. Crystallization was observed by irradiating thin amorphous TiO_2 coatings with pulsed UV lasers. Anatase phases were detected for low fluences. An increase in fluence caused a transition to a rutile phase [32]. An increase in the surface-to-volume ratio due to laser-induced crystallization has been proposed for photocatalytic applications [33] and investigated in sol-gel titania thin films [34]. A partial oxygen reduction of TiO_2 by laser irradiation and associated absorption increase has also been studied [35]. The increased absorption may enhance the photocatalytic effect [36]. The formation of a micro network on custom mixed titania-rich glasses was observed by pulsed irradiation with an excimer laser ($\lambda = 248\ \mathrm{nm}$). A crystalline phase could be generated on the surface upon irradiation in helium or nitrogen atmospheres. The photocatalytic properties of these structures were also investigated [37].

1.2.1.4 Silicon oxides

Besides glasses containing titanium oxide, silicon oxides are also treated in this thesis. Therefore, properties of silicon oxides are discussed in this section. In addition to the use of SiO_2 as a base material for many glasses, SiO_2 is also used in the semiconductor industry. Due to its high electrical insulation and easy handling in silicon-based processes, SiO_2 is suitable in

many semiconductor applications. SiO_2 is often produced by thermally induced oxidation of silicon or silicon suboxides. In the following, silicon suboxides are discussed.

Silicon monoxide (SiO) was first produced by Potter in 1905 [38]. In 1949, SiO was used for the first time as a protective coating for mirrors by vapor deposition of thin SiO layers [39]. Since then, the range of applications has expanded. In optics, SiO is usually applied as a coating. Due to the scratch-resistivity of SiO, it is still used as a protective coating. Because of its high absorption in the UV, it is well suited for laser structuring with UV excimer lasers. The fabrication of micro-optical elements from SiO is therefore well possible. Since SiO can be thermally oxidized to SiO_2, the fabrication of micro-optical SiO_2 components is also possible, as mentioned before [15]. For thermal oxidation, the SiO layers are heated to high temperatures in air (e. g. 1000°C). The incorporation of oxygen into the SiO matrix leads to an increase in the layer thickness, which has been determined experimentally to be about 35 % [40]. The increase in volume "V" can be calculated in a simplified way using the molecular weight "M" and the densities "ρ" of SiO and SiO_2 [40]:

$$\frac{V_{SiO_2}}{V_{Sio}} = \frac{M_{SiO_2}\,\rho_{SiO_2}}{M_{Sio}\,\rho_{Sio}} = \frac{30\,\frac{g}{mol}\;2.18\,\frac{g}{cm^3}}{22\,\frac{g}{mol}\;2.2\,\frac{g}{cm^3}} = 1.35 \qquad (9)$$

While the structural properties of SiO_2 are known, as explained above, the structural composition of SiO and silicon suboxide ($SiO_x, x < 2$) is still up to debate. It is known that SiO thin films are of amorphous structure. There are different models for describing the structure. In the "Mixture-Model", a composition of Si and SiO_2 is assumed. The oxygen concentration of SiO_x results from the fraction of SiO_2 in the mixture [41]. Not all experimental measurements can be described with this model, however [42]. Another model is the "Random-Bond-Model", which was proposed in 1970 [43]. With this model, optical measurements could be described better than with the "Mixture-Model". In the "Random-Bond-Model", it is assumed that intermediate oxygen states exist in addition to Si and SiO_2. In total, the five oxygen states "Si-(O_4); Si-(SiO_3); Si-(Si_2O_2); Si-(Si_3O); Si-(Si_4)" are specified. Later, a mixture of both models was proposed to form the so-called "Interface-Cluster-Mixture-Model". Here, SiO consists of Si and SiO_2 clusters surrounded by a suboxide matrix [44]. Experimental measurements confirm the presence of intermediate oxide states between Si and SiO_2 [45].

1.2.2 Metal nanoparticle implantation in transparent materials

This section provides an introduction to metal nanoparticles and the incorporation of metal nanoparticles in transparent materials. Metal nanoparticles are particles in the nanometer range, mostly consisting of gold or silver, but also of other metals such as titanium or copper. They thus form an intermediate stage between individual atoms and the bulk material of metals and therefore show distinctive features. The use of such nanoparticles (Np) goes back a long way. The Romans were already able to color glass by adding gold (Au) and silver (Ag) [46]. Of course, the cause of the coloration was not clear to them. Until 1908, there was no correct theoretical model for the optical properties of metal Np. Gustav Mie used multipole expansions of the electric and magnetic fields to solve Maxwell equations [47]. Since then, interest in metal Np has grown strongly and further discoveries have greatly expanded the field of application. Due to new developments, it was possible to fabricate specific Np (size,

shape, bimetallic Np). A very well-known application is surface enhanced Raman spectroscopy. This allows the measurement of Raman signals on single molecules. This is made possible by amplifications due to plasmonic resonances of the Np [48]. Plasmonic resonance is the ability of electrons in the metal Np to oscillate at the same frequency as an external electric field. Since the electrons can move in the metal Np in a limited way, the plasmon resonance depends on the size and shape of the metal Np. This is shown as an example in Figure 5. Here, absorption spectra of Au-Np are shown. The respective shape of the particle is shown graphically. For spherical particles, the absorption maximum is around 530 nm. The position of the peak depends only slightly on the size of the spherical particles. However, if there is an anisotropy of the particle, as shown here by nanorods, two plasmon resonances are formed. In addition to the oscillation frequency, which leads to an absorption around 530 nm, another oscillation frequency arises. This leads to a longer wavelength absorption and can be controlled by the aspect ratio of the nanorod. Higher aspect ratios, i. e. longer nanorods, lead to a red-shifted absorption [49].

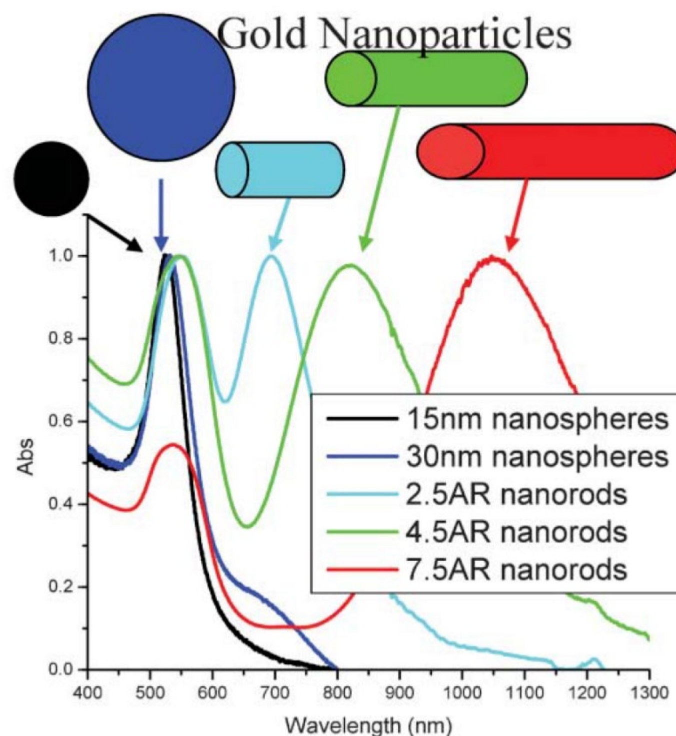

Figure 5 Absorption spectra of Au-Np. Spherical Au-Np show an absorption maximum at about 530 nm. The absorption spectra only slightly depend on the size of the spherical particle. Anisotropy of the Au-Np, e. g. nanorods, leads to a second absorption maximum at higher wavelengths. This second maximum can be controlled by the aspect ratio (AR) of the nanorod. [49]

As mentioned before, Mie theory offers an analytical way to calculate absorption spectra of metal nanoparticles. For a spherical particle, the absorbance depends on the geometric factors, i. e. the radius “R”, as well as on the material properties. The wavelength “λ” dependent material properties, i. e. the complex and real refractive index, can be summarized in the extinction efficiency “$Q_{ext}(\lambda)$” [50]. For spherical particles in a solution the absorbance can be calculated with the optical path length “l” and a number density “N” [50]:

$$A(\lambda) = \frac{\pi\, R^2\, Q_{ext}(\lambda)\, l\, N}{\ln(10)} \quad (10)$$

The experimental measurement of material parameters is easily possible only for bulk material. However, if the mean free path of electrons in the bulk material becomes comparable to the size of the nanoparticles, further assumptions for the dielectric constants have to be made. Besides the analytical solution of Maxwell's equations, numerical approaches for modeling the optical properties of metal Np are also possible. Examples are discrete dipole approximation (DDA) or finite element simulations.

The production of metal Np is possible in many ways. The following explanation is limited to the fabrication of Np incorporated in transparent materials. In one technique aluminum oxide and silicon oxide thin films doped with gold were fabricated by using pulsed laser deposition of a gold and the respective oxide target. Subsequent laser treatment of the samples results in different optical properties and morphology, depending on the laser parameters [51]. In sodium silicate glasses, the introduction of silver atoms into the glass matrix by ion exchange ($Ag^+ \leftrightarrow Na^+$) is possible [52]. Also possible is the introduction of metal atoms by ion implantation [53]. In both cases, subsequent thermal treatment leads to the formation of metal Np inside the glass. Another method can be used for spatially resolved metal Np implantation. For this purpose, the glass surface is coated with a thin metal layer and subsequently irradiated with a laser. The laser irradiation heats up the metal and glass surface resulting in metal Np incorporation in the glass. This process was demonstrated using CO_2 lasers (continuous wave lasers) [54] or pulsed excimer lasers [55]. In Figure 6, Au-Np implantation by pulsed excimer laser irradiation is schematically shown. Excimer laser irradiation with fluences below the ablation threshold of the glass results in the Au-Np being introduced close to the glass surface. The first laser pulses lead to the formation of Au-Np, which are introduced into the glass matrix during further pulses. An increased temperature leads to softening of the glass and melting of the Au-Np and thus incorporation of the Au-Np in the glass. By this method spatial control of the gold implantation in the µm-range is possible [55]. This process was also demonstrated for silver and silver-gold alloys [56].

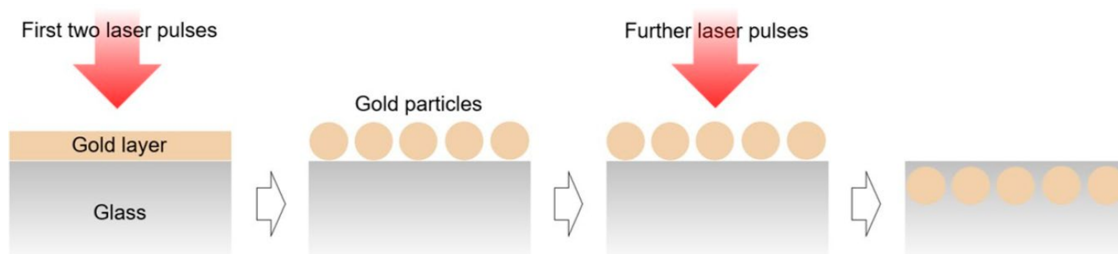

Figure 6 Schematic diagram of the Au-Np implantation process. A thin layer of gold is coated on a glass surface. The first laser pulses initiate the dewetting of the gold layer into gold particles, which are then implanted under the glass surface by further laser pulses. [55]

For the practical application of coloring glasses by laser metal Np implantation, coating the glass surface with a metal layer, which requires a vacuum process, is a laborious process. It has been shown that the process of vacuum coating can be avoided. For this purpose, metal is transferred from a polymer film to the glass surface and then implanted into the glass by laser irradiation. This process uses a metal-coated polymer film as a donor. By one laser pulse

the metal from the polymer film is transferred to the glass surface. Further laser pulses implant the metal into the glass and form Np. This method has been demonstrated with Au-Np implantation in soda lime, borofloat and flint glass [57]. This avoids the need for vacuum coating and makes the process more applicable in practice.

In parts of this thesis, the implantation of gold in $\mathrm{SiO_x}$ was used. This process was first demonstrated by Stolzenburg et al. [58]. There, a $\mathrm{SiO_x}$ surface was coated with 22 nm gold using magnetron sputtering. ArF excimer laser pulses (λ = 193 nm) were used for Au-Np implantation. After implantation, the spots show a blue-gray coloration, as can be seen in the microscope image in Figure 7 a). After a subsequent heating step (900 °C), a reddish coloration results (Figure 7 b)). This suggests that the heating step causes the Au-Np in the material to reform, resulting in more plasmonically active particles. The laser pulses and fluences used are shown in Figure 7 c). The laser spots were cleaned after irradiation by wiping with a paper tissue and isopropanol. Thus, the superficial gold particles, which were not implanted into the $\mathrm{SiO_x}$, were removed. In Figure 7 d), the cross-section of the sample by a TEM measurement is shown. For this, the sample had to be coated with a Pt-C compound. It is visible that Au-Np with a size distribution of 10 nm to 60 nm were implanted at a depth of roughly 50 nm. The authors also report a coarsening of the particles caused by the heating step.

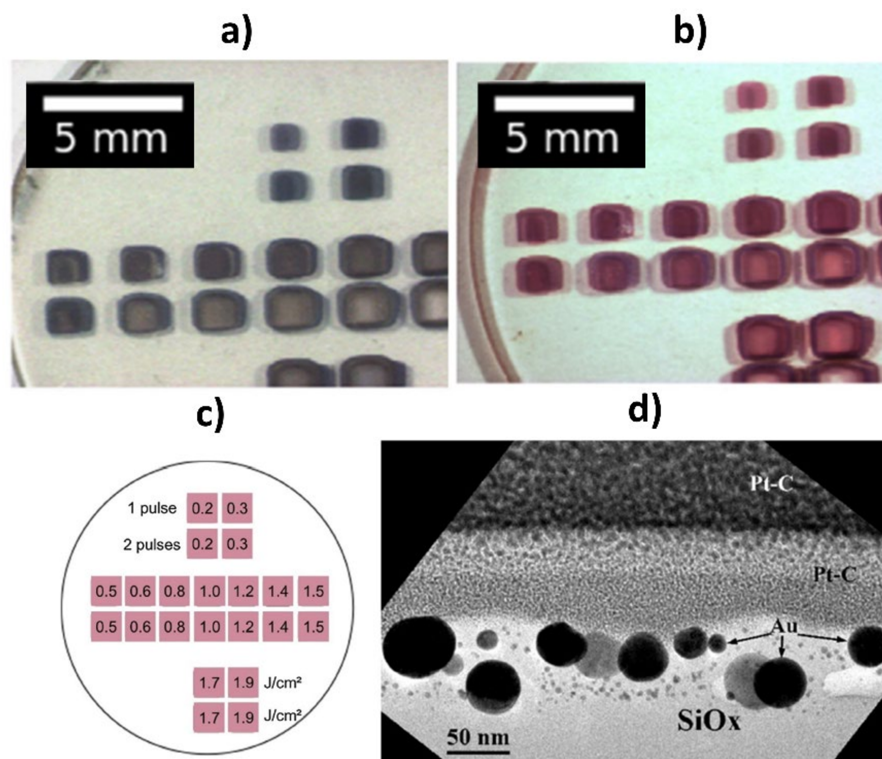

Figure 7 Results of the implantation of Au-Np in $\mathrm{SiO_x}$ are shown. Parts a) and b) show the coloration caused by the Au-Np after implantation, respectively before and after a subsequent heating step at 900 °C. In part c) the pulse numbers and fluences used for the implantation with an ArF excimer laser (λ = 193 nm) are shown. In part d) a TEM image of a cross-section shows the implanted Au-Np in the $\mathrm{SiO_x}$. [58]

1.2.3 Glass marking by lasers

In this section, laser marking of glasses is discussed. The marking of glasses with lasers is possible in various forms, for example in the glass volume as well as on the glass surface. In

the following, some relevant methods for marking glass surfaces will be discussed. A standard procedure for marking glass is carried out using a CO_2 laser [59]. This continuous wave laser operates at $\lambda = 10.6$ µm and achieves high powers. The high laser power causes the glass to heat up. High powers cause the surface material to melt. After cooling, this results in marking of the glass due to light scattering. This can also result in crack formation in the material. CO_2 lasers can be used to mark large areas quickly. For this reason, they are mainly used for marking applications in industry. However, due to the wavelength, the structure resolution that can be achieved is too large for some applications. If small structure sizes are required, lasers with shorter wavelengths must be used. The creation of scattering effects in the glass surface is of course also possible with other lasers, such as excimer lasers.

Besides marking by scattering effects, there are also other methods. One method utilizes periodic structures on the glass surface for diffractive effects. An example of such a marking can be seen in Figure 8 a) [60]. Illumination with white light results in different colored markings depending on the angle of observation. This is schematically sketched in Figure 8 b). The diffraction effect here is caused by a line grating with a period of P = 3.75 µm. A SEM image of the grating surface is visible in Figure 8 c). This structure was produced in float glass using an excimer laser. With this method, significantly higher resolution can be produced than with CO_2 lasers. Thus, highly precise and high-contrast markings can be produced, depending on the observation optics.

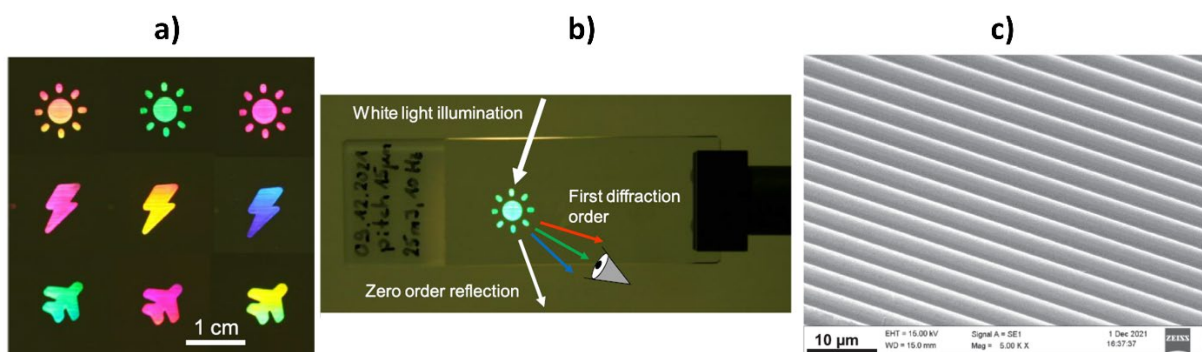

Figure 8 Diffractive markings on float glass are shown. In part a) photographs of diffractive markings are shown. The different colors result from different observation angles, as it is schematically depicted in part b). In part c) a SEM image of the grating in the glass surface is shown. The diffractive effect is caused by a line grating with a period of P = 3.75 µm. [60]

As mentioned before, plasmonic effects by metal Np can lead to coloration in the glass. Thus, colored markings can be produced with metal Np. Based on the material, size and shape of the Np, customizable absorption peaks result. Thus, markings of different colors can be produced. An example of such a marking is shown in Figure 9 [57]. QR-codes were produced by implanting gold in soda lime glass. The aforementioned transfer from a foil to the glass was used. Depending on the laser parameters, different particle densities and marking intensities result. This method thus enables the colored marking of glasses. Here, too, markings with the size of a few µm can be produced [55]. In addition to the production of colored markings by introducing metals, markings can also be fabricated by burning in dyes in glass surfaces using laser irradiation [61]. Besides the marking of glasses, the thesis also deals with silicon nanocrystals. Therefore, an introduction to silicon photonics will be given in the following.

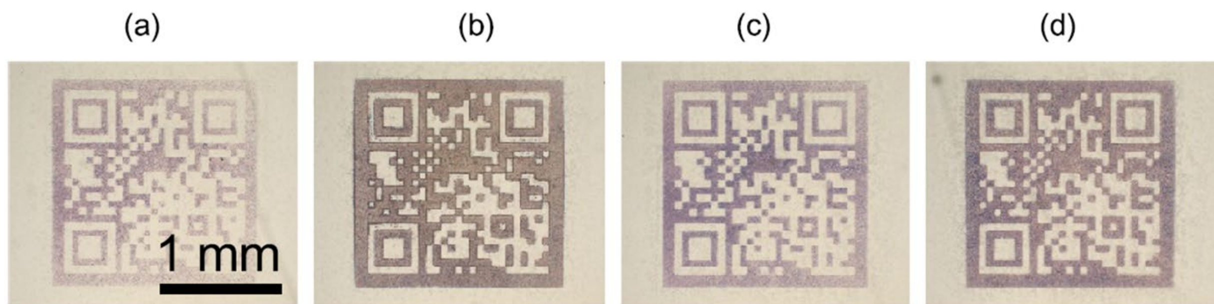

Figure 9 QR-codes produced by Au-Np implantation in soda lime glass with excimer laser irradiation. 40 nm of Au on LDPE foil was used with a) 1 pulse at 1 $\mathrm{J/cm^2}$ and 10 pulses at 0.25 $\mathrm{J/cm^2}$, b) 2 pulses at 1 $\mathrm{J/cm^2}$ and 10 pulses at 0.25 $\mathrm{J/cm^2}$, c) 1 pulse at 1 $\mathrm{J/cm^2}$ and 50 pulses at 0.25 $\mathrm{J/cm^2}$ and d) 2 pulses at 1 $\mathrm{J/cm^2}$ and 50 pulses at 0.25 $\mathrm{J/cm^2}$. The intensity of the marking can be influenced by the laser parameters. [57]

1.3 Silicon photonics

The use of microelectronics has grown exponentially in recent decades. Smartphones, video streaming or search queries have become an integral part of everyday life. This results in a strong growth of data volumes, which have to be calculated and transmitted in servers. This is shown in Figure 10 on the basis of data traffic [62]. Here, the global monthly data traffic in the years 2008 - 2018 is shown. An end to this data growth is not in sight due to increasing digitalization. The processing of the data is based on silicon-based microelectronics. This implies data transport by means of charge carriers, i. e. electrons. It is accompanied by a large loss of energy due to heat generation. A large proportion of the energy consumed by servers must therefore be used for cooling [63]. Photonic solutions offer a significant improvement in efficiency compared to electrical signals. First, communication is more efficient with optical fibers due to signal splitting, amplification, etc. [64 p. 2]. For this reason, optical fibers have prevailed over electrical signals in telecommunications. In addition, losses due to heat are greatly reduced compared to electronic signals. The use of light at the micro level, i. e. also in the chip area, would therefore significantly increase efficiency. For practical applications, however, cost factors must also be taken into account. Here, the use of silicon-based photonics would make sense. Low-cost processes with large production numbers are already available for silicon. Furthermore, silicon is a cheap and non-toxic raw material. In addition, silicon-based photonics would enable the integration of photonics into microelectronics [65 p. 1]. In the following section, the basics of the silicon bandgap are discussed.

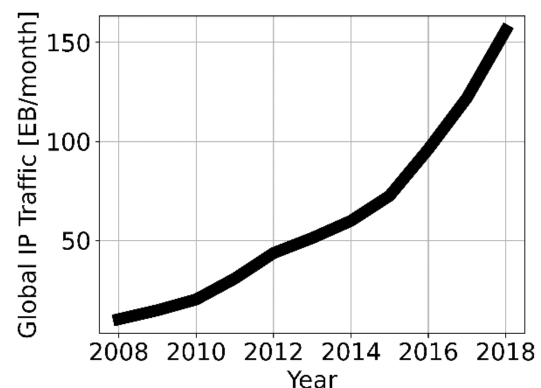

Figure 10 Global IP traffic in Exabyte per month in the years 2008 – 2018. Data from [62].

1.3.1 Silicon bandgap

Silicon is not useful for active photonic applications due to its low efficiency of light emission. This is due to the band gap and shall be explained with the help of Figure 11. Here, the process of photoluminescence is considered. However, analogous considerations also apply to electroluminescence or similar.

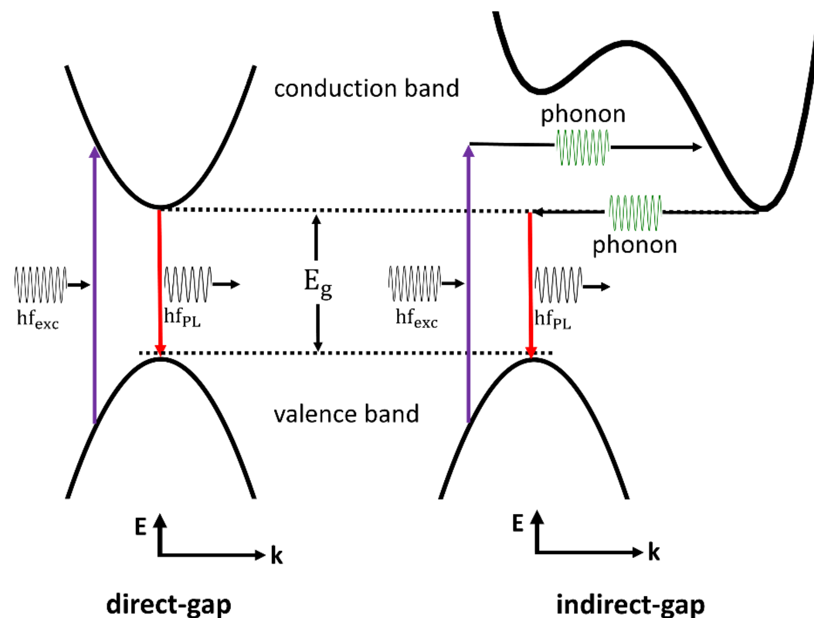

Figure 11 Schematic diagram of the band models of a direct-gap and indirect-gap material in a photoluminescence process. The energy is plotted vertically. The energy of the band gap “E_g” is marked between the conduction band and the valence band. The momentum is plotted horizontally. In both cases, a photon (hf_{exc}) excites an electron, which emits a PL photon (hf_{PL}) at lower energy when it decays into the valence band. In the indirect bandgap, a phonon must be involved to preserve momentum.

In the schematic diagram, the energy is plotted vertically and the momentum is plotted horizontally. In the left case a direct bandgap is shown. This means that the minimum of the conduction band is above the maximum of the valence band. Thus, there is no difference in momentum and a photon is sufficient for an interband transition. In the PL process an excitation photon excites an electron from the valence band into the conduction band (violet arrow). For this, the energy of the excitation photon (hf_{exc}) must be at least as large as the energy of the bandgap (E_g). The electron is thereby excited into states of higher energy in the conduction band. It then quickly drops to the state of lowest energy in the conduction band by emitting phonons, satisfying conservation of energy and momentum. This decay usually occurs in the sub-picosecond time period [5 p. 116]. On the time scale of nanoseconds, i. e. much later, a radiative decay of the electron from the conduction band into the valence band then occurs. A photon is emitted which has a longer wavelength, i. e. lower energy, than the excitation photon. An example of material with a direct band gap is gallium arsenide (GaAs) [5 p. 116]. For the indirect band gap, the same processes happen in photoluminescence. However, the minimum of the conduction band does not sit above the maximum of the valence band in the momentum space. This results in a difference in momentum, which must be compensated for by the participation of a phonon (shown in green). The simultaneous

participation of a photon and a phonon for the band transition significantly increases the radiative lifetime. This increases the probability of a non-radiative recombination of the electron. The radiative lifetime for direct materials is in the nanosecond (10^{-9} s) or even picosecond (10^{-12} s) range [5 p. 116], [66]. For silicon, the radiative lifetime is in the millisecond (10^{-3} s) range [67]. In contrast, the non-radiative lifetime in silicon is in the range of nanoseconds [68]. The efficiency for photoluminescence, or internal quantum efficiency, η_R can be expressed using the radiative lifetime (τ_R) and the non-radiative lifetime (τ_{NR}) [5 p. 115]:

$$\eta_R = \frac{1}{1 + \tau_R/\tau_{NR}} \qquad (11)$$

For high luminescence efficiency, the radiative lifetime must therefore be as low as possible compared to the non-radiative lifetime. For silicon, this results in a low efficiency in the range of $\eta_R \sim 10^{-6}$. Silicon is therefore not suitable as a light emitter.

1.3.2 Silicon nanocrystals

Since the efficiency of light emission from silicon depends on the band structure, the efficiency can be changed by influencing the band structure. A confinement of the charge carriers in a structure changes the density of states. This is schematically sketched in Figure 12 [4 p. 288].

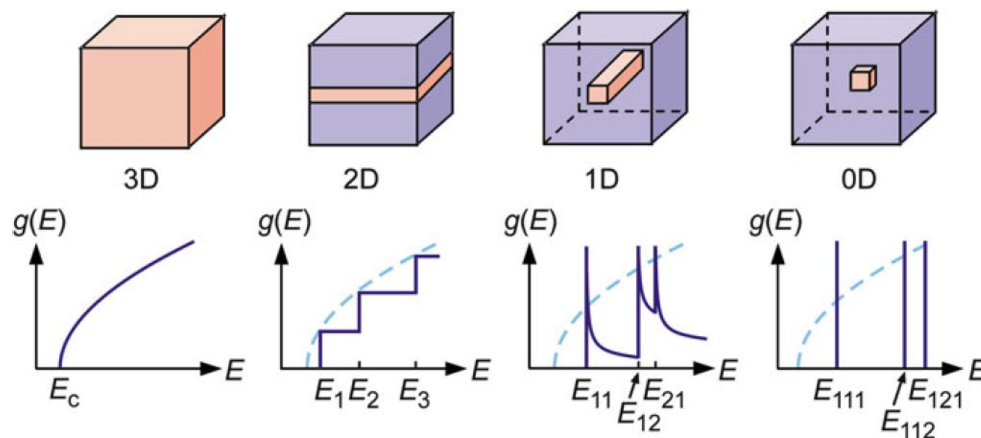

Figure 12 The electronic density of states g(E) of semiconductors (red) is shown for different dimensionalities. A boundary (blue) results in a discretion of the density of states. The dashed curve indicates the density of states for the 3D case. [4 p. 288]

The continuous electronic density of state (DOS) in a 3D material results from the quasi-infinite periodic lattice structure of the material. By confinement of the material the DOS changes dramatically, as can be seen in the sketch for quantum wells (2D), quantum wires (1D) or quantum dots/nanocrystals (0D). The three-dimensional confinement in a quantum dot restricts carrier motion in all directions, leading to a fully quantized DOS [4 p. 290]. The confinement effect is often referred to as quantum confinement. Of course, the quantum confinement is strongly dependent on the size. Confinement in a nanocrystal becomes relevant at sizes of about the Bohr radius of an exciton [4 pp. 85, 292]:

$$R_{B,Ex} = \frac{h^2 \varepsilon \varepsilon_0}{\pi \mu e_0^2} \tag{12}$$

With “h” being the Planck constant, “ε” and “ε_0” being the relative permittivity of the solid and the vacuum, respectively, “μ” being the reduced mass of the exciton and “e_0” being the charge of an electron. For silicon, this results in a size of 4.9 nm [65 p. 43]. Crystalline silicon in this size range is called silicon nanocrystals (Si-Nc). Si-Nc have the potential to effectively emit light. This is due to several facts. On the one hand, the confinement of the carriers reduces the probability of an interaction with non-radiative recombinative centers. Thus, the quantum efficiency for light emission increases. Furthermore, a confinement in the position space leads to an expansion in the momentum space. This is caused by Heisenberg’s uncertainty relation of the space “x” and the momentum “p” [69 p. 102]:

$$\Delta x \cdot \Delta p \geq \hbar \tag{13}$$

Thus, a quasi-direct band gap results, as schematically shown in Figure 13. As a result, interband transition without phonons are possible [70]. Therefore, radiative lifetimes are significantly shorter. For Si-Nc, these are in the range of microseconds (10^{-6} s) [67]. The band structure, thus also the band gap E_g, depends on the size of the Si-Nc. In Figure 14 results of different experiments are collected [65 p. 24]. The band gap is plotted against the Si-Nc diameter. A clear increase in the band gap can be measured for smaller diameters. The wavelength of the light emission from Si-Nc can therefore be varied by adjusting the Si-Nc diameter.

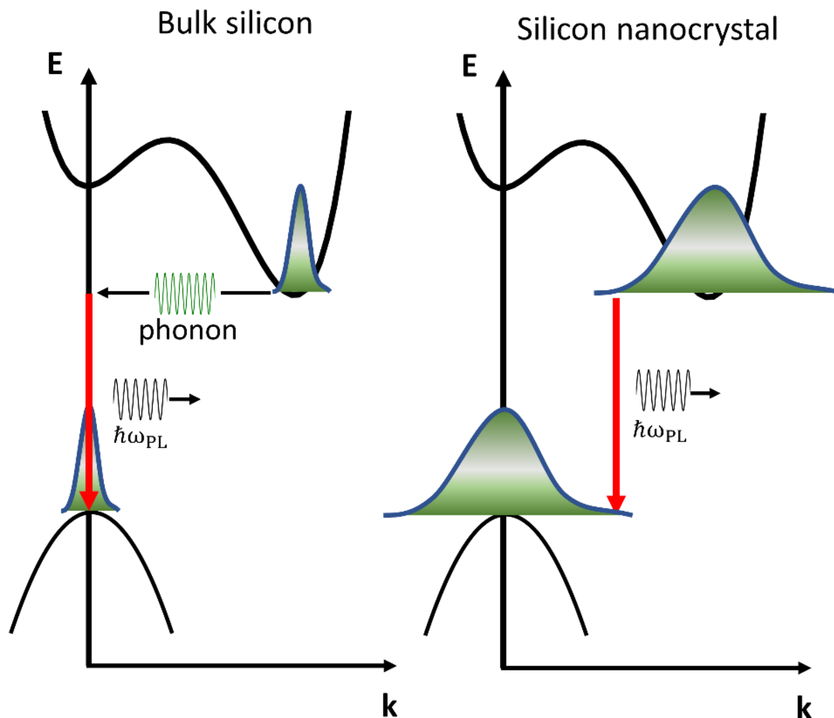

Figure 13 Simplified band models of bulk silicon (left) and Si-Nc (right). The wavefunction of the electrons is shown in green. Silicon as a bulk material has an indirect bandgap. Electron interband transitions require a phonon for momentum conservation. Due to the carrier confinement in the Si-Nc the uncertainty in the momentum space spreads. A quasi-direct bandgap results, i. e. an electron interband transition is possible without a phonon.

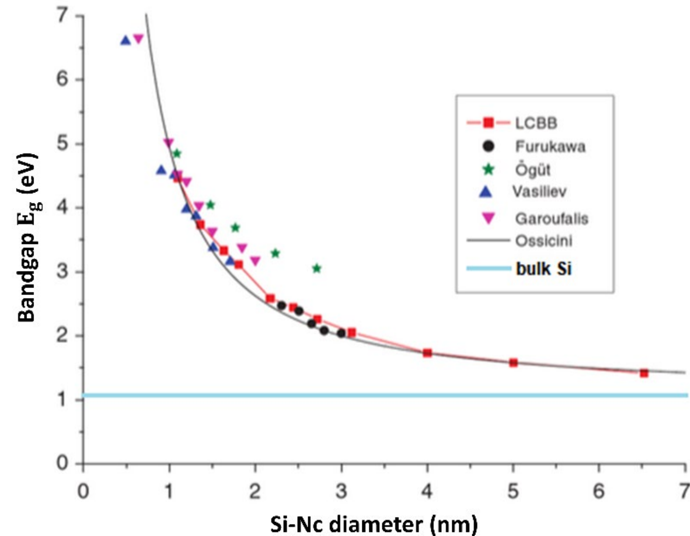

Figure 14 Results of different experiments show a clear increase in the bandgap for decreasing Si-Nc diameters. The bright blue line indicates the bandgap of bulk silicon. Image modified after *[65 p. 24]*.

In addition to the quantum confinement effect, the surface of Si-Nc also plays a crucial role in light emission. Measurements on Si-Nc also show various surface state emissions as causes. The exact cause for the light emission of Si-Nc is therefore not yet clear. However, it is certain that a variety of influences are involved in the light emission. In addition to the size of the Si-Nc, these include, for example, defect states on the Si-Nc surface or the band structure of the surrounding matrix.

Although Si-Nc have a significantly higher quantum efficiency than bulk silicon, it is still not sufficient for practical applications. Therefore, various methods have been investigated to further increase quantum efficiency and to realize practical application. Since this topic is important for many applications, it has received a lot of attention. Therefore, a complete overview of the literature is not possible in this thesis. Instead, an overview of the most important topics for this work will be given.

1.3.2.1 Surface effects

For smaller particles, the importance of the particle surface increases due to the ratio of surface area to volume. Therefore, the surface area of Si-Nc, or interface to the surrounding matrix, is of crucial importance for light emission.

An important role for the efficiency of light emission from Si-Nc are defects that provide non-radiative channels for electron-hole recombination. If these occur at the interface of the crystalline silicon with the surrounding matrix, the probability of non-radiative recombination is very high, due to the high surface-to-volume ratio. Thus, the efficiency of light emission is very low. If Si-Nc are embedded in a $\mathrm{SiO_2}$ matrix, for example, $\mathrm{P_b}$ centers, i. e. silicon dangling bonds, reduce the efficiency of light emission. Saturation of the dangling bonds with hydrogen atoms, so-called hydrogen passivation, increases the efficiency of light emission. This hydrogen passivation is a standard process in the semiconductor industry [71]. In addition to hydrogen passivation, passivation by oxygen, nitrogen or carbon is also possible [72].

Defect states can contribute not only to the non-radiative recombination of Si-Nc, but also to radiative recombination and thus influence the spectrum of the PL. Examples are bridging oxygen bonds (Si-O-Si) or silicon-oxygen double bonds (Si=O) [73] [74]. Also point-defects or color-centers in a SiO_2 matrix can generate PL bands [73].

Another effect influencing the PL of Si-Nc is surface functionalization of Si-Nc. For example, alkyl-terminated Si-Nc, oxidized alkyl-terminated Si-Nc, or alkylamine-terminated Si-Nc have been used to tune the PL spectrum from 450 nm to 850 nm [74]. Also, the so-called doping, i. e. the introduction of foreign atoms (e. g. phosphorus or boron) into the surrounding matrix, changes the PL spectrum of Si-Nc [72].

In summary, the influence of the surrounding matrix and the surface of the Si-Nc on the PL of Si-Nc is related to many causes. Not all aspects have been conclusively clarified. However, it is clear that for different sample systems, individual considerations need to be used to identify the causes of respective PL spectrum.

1.3.2.2 Production methods

In this section, different production methods of Si-Nc are described. One common method is the thermally induced phase separation of silicon suboxide (SiO_x). In this process, a coating is deposited on a substrate and then heated in an inert atmosphere. Depending on the heating temperature, different crystal sizes are formed [65 p. 255]. The phase separation proceeds according to the following scheme [75]:

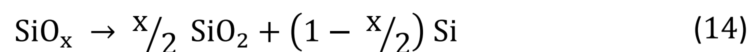

$$SiO_x \rightarrow {}^{x}/_{2}\ SiO_2 + \left(1 - {}^{x}/_{2}\right) Si \qquad (14)$$

Si-Nc are thus formed in a silicon oxide matrix. However, it has been shown that the phase separation does not proceed completely. Due to stress in the layers caused by the phase separation, only a partial phase separation occurs [76].

By using this method, the production of Si-Nc is possible with a simple method. A disadvantage is the large size distribution of the Si-Nc. With a more complex approach using a superlattice consisting of SiO_2 and SiO_x, the crystal sizes and the density of the Si-Nc can be specifically adjusted. This is shown in Figure 15 in part a). The multilayer system is shown in a cross-sectional transmission electron micrograph (TEM). By a heating process, Si-Nc are formed in the SiO_x layers, as shown in part b). The size of the Si-Nc, and thus the PL spectrum of the Si-Nc, can be controlled by the layer spacing. PL measurements on different large Si-Nc are shown in part c). The density of the Si-Nc can be controlled by the oxygen content of the SiO_x, i. e. the “x” [75].

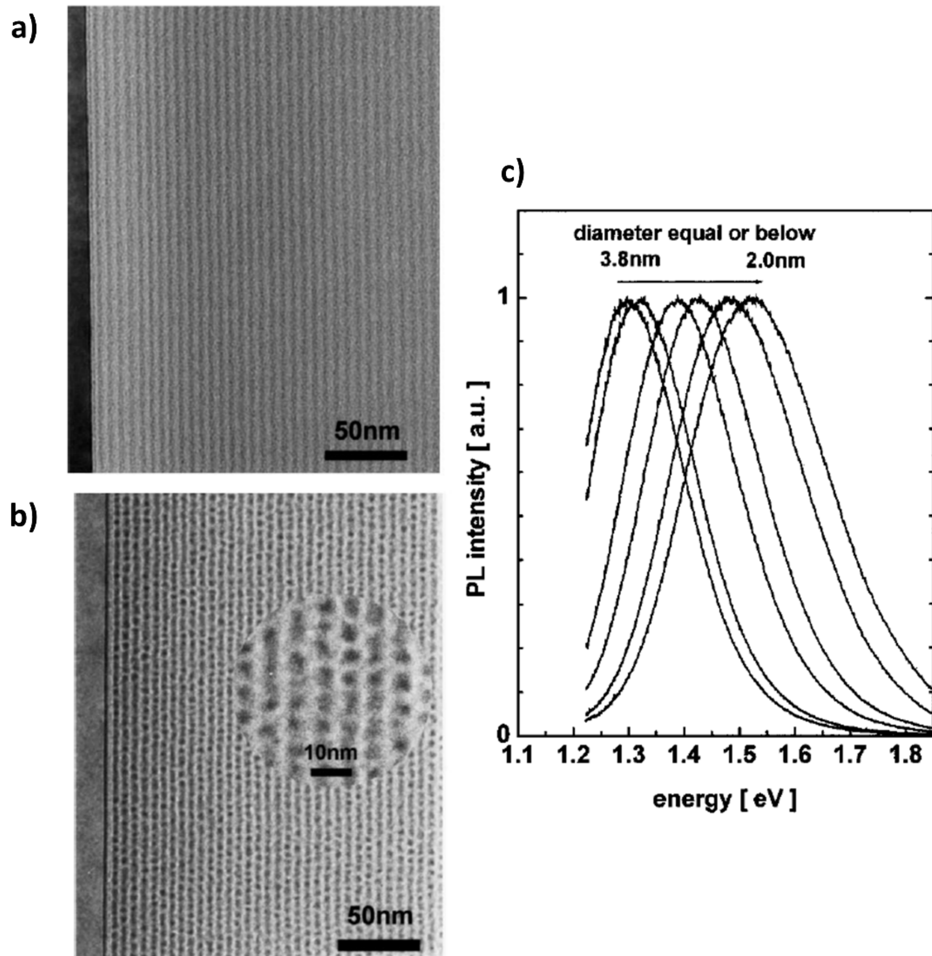

Figure 15 TEM images of the cross section of the $\mathrm{SiO_2}$ and $\mathrm{SiO_x}$ multilayer are shown. In part a) the multilayer is as coated. In part b) Si-Nc have formed in the $\mathrm{SiO_x}$ layers by thermal annealing. The Si-Nc size can be adjusted by the layer thickness. Thereby, the PL spectrum of the Si-Nc can be adjusted as shown in part c). Image modified after [75].

Another possibility for the production of Si-Nc is to achieve an excess of silicon in a $\mathrm{SiO_2}$ matrix by silicon ion implantation. In this case, the depth at which the Si-Nc are formed in a subsequent heating process can be controlled by the implantation energy of the ions [65]. In this way, spatially resolved production of Si-Nc is theoretically also possible. However, the implantation of ions is a time-consuming and cost-intensive process. A less complex method uses a commercial laser to induce a phase separation in $\mathrm{SiO_x}$ to produce Si-Nc [77]. In this process, a continuous-wave laser (λ = 405 nm) is focused on $\mathrm{SiO_x}$. At power densities of $1.2 \cdot 10^5\ \mathrm{W/cm^2}$, Si-Nc are formed without the surface of the film becoming degraded. Thus, locally resolved production of Si-Nc is possible, as can be seen in the PL mapping image in Figure 16. The photoluminescent line is produced by laser writing with a laser spot size of 6 µm at a speed of 300 µm/s, corresponding to an irradiation time of 20 ms. A laser power of 30 mW was used.

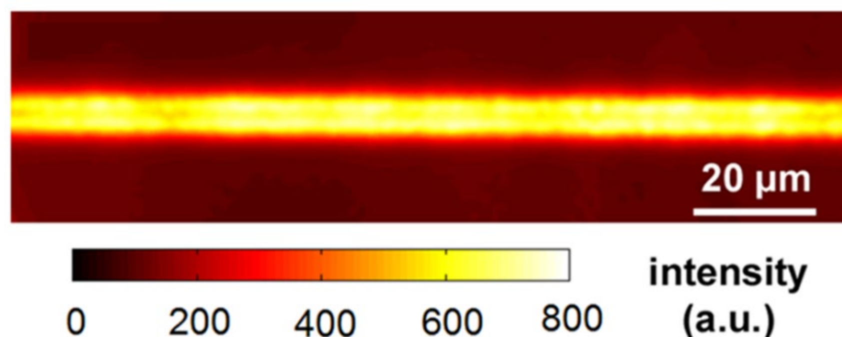

Figure 16 PL mapping images of laser-produced Si-Nc in SiO_x. The laser (λ = 405 nm) is focused to a spot with a diameter of 6 µm at a power of 30 mW. A scanning speed of 300 µm/s was used to induce Si-Nc formation. Image modified after [77].

Other possibilities for Si-Nc production are, for example, sputtering [78] or plasma-enhanced chemical vapor deposition [79]. Since the host matrix has a decisive influence on the PL spectrum of the Si-Nc, the different production methods also result in Si-Nc with different PL spectra.

1.3.2.3 Plasmon enhancement

In this section, methods for enhancing the photoluminescence of Si-Nc by plasmonic particles are described. Plasmonic effects through metal nanoparticles offer a possibility to increase the efficiency of light emission from Si-Nc. Various attempts have been made in the literature to increase the PL of Si-Nc in this way, mostly using gold or silver Np.

If the metal Np are placed close to the Si-Nc, they can influence the optical density of states of the Si-Nc. Thus, the spontaneous emission rate of the Si-Nc can be increased, which increases the efficiency of the PL. This is also known as Purcell effect [80 p. 254]. The metal Np can also ensure that non-radiative emission energy from the Si-Nc is radiatively decoupled by an energy transfer to the surface plasmons of the metal Np. In this way, the fraction of energy which is radiatively decoupled is increased [81]. The following section reviews some important conclusions of such experiments in the literature.

A connection between the distance of Si-Nc to metal Np and the enhancement of PL of Si-Nc was first shown by Biteen et al. [81]. For this purpose, Si-Nc were prepared by Si ion implantation in quartz at a depth of about 20 nm followed by a heating process. To minimize defect states, the Si-Nc were passivated with hydrogen. The enhancement of the PL was investigated by a nanoporous gold layer, which was prepared by evaporation of an Ag-Au layer followed by an etching process. The distance between the Si-Nc and the nanoporous gold layer was varied in 2.5 nm steps by an etching process. A scanning electron microscope image (SEM) of the nanoporous gold layer is shown in Figure 17 a). In part b), the schematic structure of the sample system is shown. The PL is excited with a wavelength of 488 nm. The resulting enhancement of the PL signals are visible in part c). The enhancement of the PL “η_{PL}” at 780 nm is plotted against the etch depth. The enhancement reaches a maximum at a separation distance of about 10 nm. The enhancement is partly attributed to an increase in the radiative decay rate of the Si-Nc. It is also mentioned that very small distances between Si-Nc and Au-Np can lead to a quenching of the PL, or in the case of direct contact by electronic

charge transfer to the extinction of the PL [81] [82] [83]. The separation distance between the Si-Nc and the metallic Np is thus an important parameter for the PL enhancement.

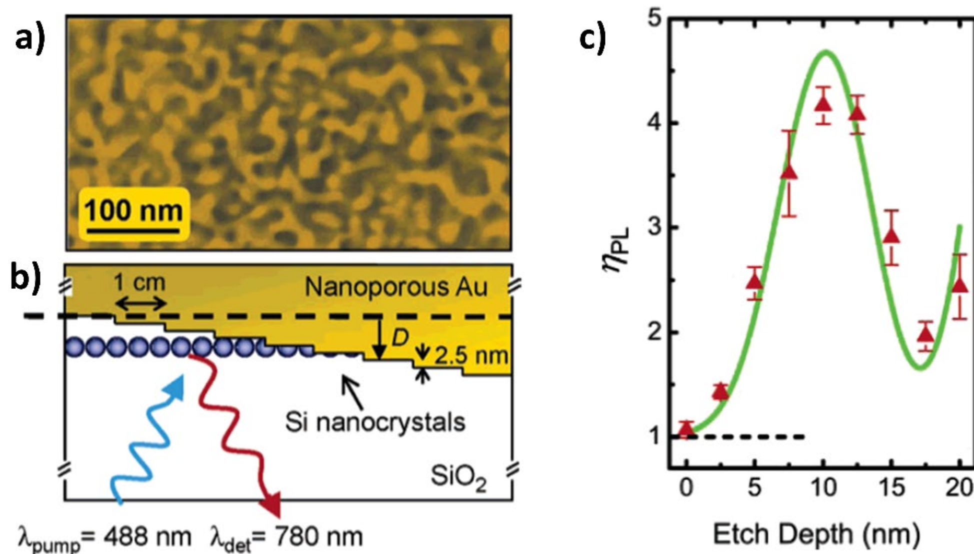

Figure 17 In part a) a SEM image of the nanoporous gold on top of the Si-Nc containing quartz substrate is shown. In part b) a schematic diagram of the sample is depicted. The PL is excited at 488 nm. The distance of the Si-Nc, which are located at a depth of about 20 nm in the quartz, to the Au-Np is varied in 2.5 nm steps. In part c) the enhancement of the PL "η_{PL}" at 780 nm is plotted against the etch depth. A maximum enhancement at a distance of about 10 nm is measured. Image modified after [81].

Goffard et al. have shown that the enhancement of the PL of Si-Nc can be adjusted by variation of the Au-Np size [84]. Si-Nc were prepared by vapor deposition of multilayers consisting of SiO_2 and SiO layers followed by thermal annealing. The Au-Np were prepared by electron beam lithography. Figure 18 a) shows a schematic sketch of the sample system. The red dots depict the Si-Nc, which are located under the Au-Np. The size of the Au-Np was varied, this is shown as an example in part b) in a SEM image. The variation of the Au-Np size is accompanied by a shift of the plasmon resonance and thus of the absorption peak of the Au-Np. This is shown in part c). In part d) the PL spectrum of the Si-Nc is plotted without the influence of the Au-Np. When comparing the enhancement of the PL with the absorption peak of the Au-Np a clear correlation can be seen. This is shown in part e). For smaller Au-Np a blue shift of the absorption peak and the PL enhancement results. Therefore, for a strong enhancement of the PL, there should be a match as good as possible between the PL of the Si-Nc and the absorption peak of the Au-Np, i. e. the plasmon resonance.

In another study Köthemann et al. showed the influence of Au-Np and their surrounding matrix on the PL of Si-Nc [85]. Si-Nc were prepared in silicon oxygen nitride (SiON) thin films by thermal annealing. By electron beam lithography Au-Np were fabricated on top of the SiON layer. A reduction in PL signal by the Au-Np was measured. The authors attribute the reduction of the PL to the Au-Np not being in resonance with the PL of the Si-Nc and thus acting as random scattering centers. In a next step the Au-Np were overgrown with a further Si-Nc containing SiON film resulting in PL enhancement. The size of the Au-Np was varied and the PL enhancement depends on the spectral overlap of the Au-Np resonance and the PL signal of

the Si-Nc. The authors further stated, that the higher refractive index of the surrounding material of the Au-Np increases the resonance to the PL of the Si-Nc.

Another possibility for the enhancement of the PL of Si-Nc by metallic Np can be achieved via the interaction with the PL excitation light. Gardelis et al. have produced Si-Nc in a multilayer system between SiO_2 layers [86]. Silver Np with an absorption around 400 nm were deposited on the surface. This absorption partially overlaps with the PL spectrum of Si-Nc, but a larger overlap is given with the excitation wavelength (457.9 nm) of the PL. This is visible in part a) in Figure 19. Here the absorption spectrum of the Ag-Np is plotted. In part b) the PL spectrum of the Si-Nc is plotted with the dashed line. It is shown magnified by a factor of 20x. The solid line shows the PL spectrum of the Si-Nc in interaction with the Ag-Np. An increase of the PL by a factor of 20x is measurable. Additionally, a clear blue shift is detected. The enhanced PL is attributed on the one hand to an increased recombination rate due to the plasmonic coupling. This can also explain the blueshift, since the overlap of the PL of the Si-Nc with the plasmon resonance is stronger in the shorter wavelength region. Furthermore, an increased absorption cross section of the Si-Nc by the Ag-Np with the excitation light is mentioned as a cause. It is thus shown that an enhancement of the PL by plasmonic effects is possible even without a match between the plasmon resonance of the metal Np and the PL spectrum of the Si-Nc.

In the following, the literature for the introduction is provided. Subsequently the manuscripts of the cumulative dissertation are presented in the second chapter.

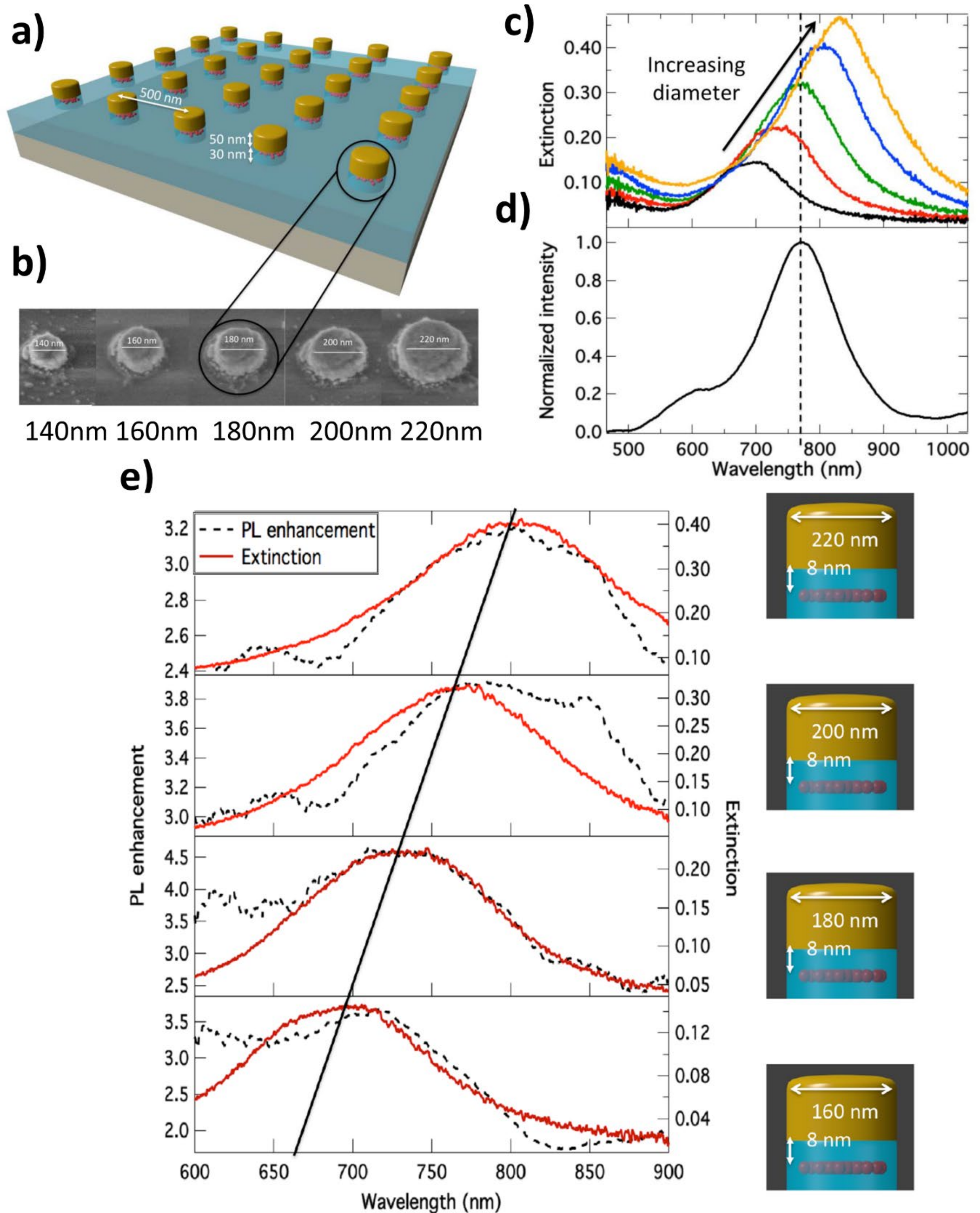

Figure 18 A sample with Au-Np on top of Si-Nc (red dots) is schematically shown in part a). The size of the Au-Np is varied, as it is shown in SEM images in part b). The variation of the Au-Np diameter is accompanied by the spectral shift of the plasmon resonance (part c)). The PL spectra of the Si-Nc without the influence of the Au-Np is shown in part d). The resulting PL enhancement by the interaction of the Au-Np with the Si-Nc is shown in part e). A correlation of the PL enhancement with the extinction of the Au-Np is shown. Image modified after [84].

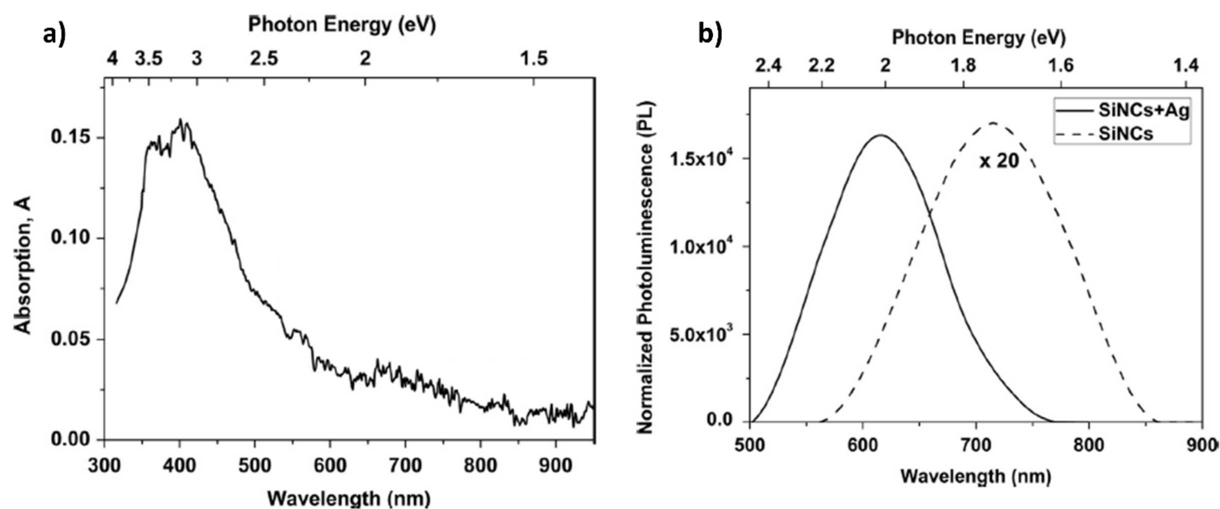

Figure 19 The absorption spectra of the Ag-Np is plotted in part a). An absorption between 365 nm and 443 nm is measurable. In part b) the PL spectra of the Si-Nc is shown as the dashed line, magnified by a factor of 20x. The PL spectra of the Si-Nc in interaction with the Ag-Np is shown in the solid line. An enhancement by 20 and a blueshift is shown. [86]

1.4 References of the Introduction

1. *Konrad Zuse.* **W. Karl, K. Waldschmidt and H. Zuse.** 2011, Informatik Spektrum, Vol. 34, pp. 551, DOI: https://doi.org/10.1007/s00287-011-0580-5.

2. *Laser Processing of Materials.* **P. Schaaf.** Heidelberg : Springer, 2010. ISBN 978-3-642-13280-3.

3. *Experimentalphysik 2.* **W. Demtröder.** Berlin-Heidelberg : Springer, 2004, Vol. 3. ISBN 3-540-20210-2.

4. *Semiconductor Physics.* **K. W. Böer and U. W. Pohl.** Naples and Berlin : Springer, 2018. ISBN 978-3-319-69148-0.

5. *Optical Properties of Solids.* **M. Fox.** Oxford : Oxford University Press, 2001, Vol. 2nd. ISBN 978-0-19-957337-0.

6. *Laser-Induced Electric Breakdown in Solids.* **N. Bloembergen** 1974, IEEE Journal of Quantum Electronics, Vol. 10, pp. 375, DOI: https://doi.org/10.1109/JQE.1974.1068132.

7. *Laser Processing and Chemistry.* **D. Bäuerle.** Heidelberg Dordrecht London New York : Springer, 2011, Vol. 4. ISBN 978-3-642-17612-8.

8. *Femtosecond, picosecond and nanosecond laser ablation of solids.* **B. N. Chichkov, C. Momma, S. Nolte, F. von Alvensleben and A. Tünnermann** 1996, Appl. Phys. A, Vol. 63, pp. 109, DOI: https://doi.org/10.1007/BF01567637.

9. *Excimer laser ablation of thick SiO_x-films: Etch rate measurements and simulation of the ablation threshold.* **J. Ihlemann, J. Meinertz and G. Danev** 2012, Appl. Phys. Lett., Vol. 101, pp. 091901, DOI: https://doi.org/10.1063/1.4748127.

10. *Direct fabrication of microgratings in fused quartz by laser-induced plasma-assisted ablation with a KrF excimer laser.* **J. Zhang, K. Sugioka and K. Midorikawa** 1998, Opt. Lett., Vol. 23, pp. 1486, DOI: https://doi.org/10.1364/ol.23.001486.

11. *One-step microfabrication of fused silica by laser ablation of an organic solution.* **J. Wang, H. Niino and A. Yabe** 1998, Appl. Phys. A, Vol. 68, pp. 111, DOI: https://doi.org/10.1007/s003390050863.

12. *Laser etching of fused silica using an adsorbed toluene layer.* **K. Zimmer, R. Böhme and B. Rauschenbach** 2004, Appl. Phys. A, Vol. 79, pp. 1883, DOI: https://doi.org/10.1007/s00339-004-2961-y.

13. *Laser induced backside dry etching of transparent materials.* **B. Hopp, C. Bass and T. Smausz** 2007, Appl. Surf. Sci., Vol. 253, pp. 7922, DOI: https://doi.org/10.1016/j.apsusc.2007.02.068.

14. *Laser patterning of SiO_x-layers for the fabrication of UV diffractive phase elements.* **M. Schulz-Ruhtenberg, J. Ihlemann and J. Heber** 2005, Appl. Surf. Sci., Vol. 248, pp. 190, DOI: https://doi.org/10.1016/j.apsusc.2005.03.096.

15. *Laser Processing of Silicon Suboxide for the Fabrication of Multilevel Fused Silica Diffractive Phase Elements.* **L. J. Richter, C. M. Beckmann, J. Meinertz and J. Ihlemann** 2018, Journal of Laser Micro/Nanoengineering, Vol. 13, pp. 249, DOI: http://dx.doi.org/10.2961/jlmn.2018.03.0018.

16. *On-chip laser processing for the development of multifunctional microfluidic chips.* **H. Wang, Y. Zhang, W. Wang, H. Ding and H. Sun** 2017, Laser Photonics Rev., Vol. 11, pp. 1600116, DOI: https://doi.org/10.1002/lpor.201600116.

17. *Laser polishing and laser shape correction of optical glass.* **C. Weingarten, A. Schmickler, E. Willenborg, K. Wissenbach and R. Poprawe** 2017, J. Laser Appl., Vol. 29, pp. 011702, DOI: https://doi.org/10.2351/1.4974905.

18. *Transparten laser-structured glasses with superhydrophilic properties for anti-fogging applicaitons.* **M. Domke, G. Sonderegger, E. Kostal, V. Matylitsky and S. Stroj** 2019, Appl. Phys. A, Vol. 125, pp. 675, DOI: https://doi.org/10.1007/s00339-019-2953-6.

19. *Pulsed Laser Deposition: Fundamentals, Applications, and Perspectives.* **F. Craciun, T. Lippert and M. Dinescu** 2020, pp. 1291 - 1323. ISBN 978-3-030-63647-0.

20. *Photo-oxidation of silicon monoxide to silicon dioxide with pulsed far-ultraviolet (193 nm) laser radiation.* **S. E. Blum, K. H. Brown and R. Srinivasan** 1983, Appl. Phys. Lett., Vol. 43, pp. 1026, DOI: https://doi.org/10.1063/1.94216.

21. *Figure correction of borosilicate glass substrates by nanosecond UV excimer laser irradiation.* **C. M. Beckmann and J. Ihlemann** 2020, Optics Express, Vol. 28, pp. 18681, DOI: https://doi.org/10.1364/OE.393626.

22. *Microstructuring of Glasses.* **D. Hülsenberg, A. Harnisch and A. Bismarck.** Berlin Heidelberg New York : Springer, 2008. ISBN 978-3-540-26245-9.

23. *Thermal conductivity of isotopically modified single crystal diamond.* **Lanhua Wei, P. K. Kuo, R. L. Thomas, T. R. Anthony and W. F. Banholzer** 1993, Phys. Rev. Lett., Vol. 70, pp. 3764, DOI: https://doi.org/10.1103/PhysRevLett.70.3764.

24. *Optiktechnologie.* **J. Bliedtner and G. Gräfe.** Leipzig : Carl Hanser Verlag, 2009, Vol. 2. ISBN 978-3-446-42215-6.

25. *Electrochemical Photolysis of Water at a Semiconductor Electrode.* **A. Fujishima and K. Honda** 1972, Nature, Vol. 238, pp. 37, DOI: https://doi.org/10.1038/238037a0.

26. *Pilkington Activ (TM).* **Pilkington.** Head Office - 3-5-27 Mita Minato-ku Tokyo : Nippon Sheet Glass Co., Ltd., Visited 07.03.2023: URL - https://www.pilkington.com/de-at/at/produkte/produktkategorien/selbstreinigung/pilkington-activ.

27. *Refractive Indices of Rutile and Sphalerite.* **J. R. DeVore** 1951, J. Opt. Soc. Am., Vol. 41, pp. 416, DOI: https://doi.org/10.1364/JOSA.41.000416.

28. *Effect of TiO_2 on optical properties of glasses in the soda-lime-silicate system.* **S. Karlsson, L. G. Bäck, P. Kidkhunthod, K. Lundstedt and L. Wondraczek** 2016, Opt. Mater. Express, Vol. 6, pp. 1198, DOI: https://doi.org/10.1364/OME.6.001198.

29. *Band alignment of rutile and anatase TiO_2.* **D. O. Scanlon, C. W. Dunnill, J. Buckeridge, S. A. Shevlin, A. J. Logsdail, S. M. Woodley, C. R. A. Catlow, M. J. Powell, R. G. Palgrave, I. P. Parkin, G. W. Watson, T. W. Keal, P. Sherwood, A. Walsh and A. A. Sokol** 2013, Nature Mater., Vol. 12, pp. 798, DOI: https://doi.org/10.1038/nmat3697.

30. *Femtosecond laser direct writing of TiO_2 crystalline patterns in glass.* **Y. Liu, L. Wang, Y. Dai, H. Ma, G. Lakshminarayana and K. Qiu** 2008, Appl. Phys. B, Vol. 93, pp. 613, DOI: https://doi.org/10.1007/s00340-008-3166-4.

31. *Three-dimension direct writing TiO_2 crystalline patterns in Bi-free glass using femtosecond laser.* **P. Zhou, H. Ma, Y. Du, Y. Han, B. Lu and M. Zhong** 2011, Appl. Phys. A, Vol. 102, pp. 295, DOI: https://doi.org/10.1007/s00339-010-6112-3.

32. *Phase transitions in thin titanium oxide films under the action of excimer laser radiation.* **P. Mitrev, G. Benvenuti, P. Hofman, A. Smirnov, N. Kaliteevskaya and R. Seisyan** 2005, Tech. Phys. Lett., Vol. 31, pp. 908, DOI: https://doi.org/10.1134/1.2136949.

33. *Crystallisation of TiO_2 thin films induced by excimer laser irradiation.* **O. Van Overschelde, R. Snyders and M. Wautelet** 2007, Appl. Surf. Sci., Vol. 254, pp. 971, DOI: https://doi.org/10.1016/j.apsusc.2007.08.018.

34. *Excimer laser processing as a tool for photocatalytic design of sol–gel TiO_2 thin films.* **K. Starbova, V. Yordanova, D. Nihtianova, W. Hintz, J. Tomas and N. Starbov** 2008, Appl. Surf. Sci., Vol. 254, pp. 4044, DOI: https://doi.org/10.1016/j.apsusc.2007.12.036.

35. *Ultraviolet laser irradiation induced chemical reactions of some metal oxides.* **C. Sol and R. J. D. Tilley** 2001, J. Mater. Chem., Vol. 11, pp. 815, DOI: https://doi.org/10.1039/B006787N.

36. *Shedding light on black titania.* **V. Glezakou and R. Rousseau** 2018, Nature Mater., Vol. 17, pp. 856, DOI: https://doi.org/10.1038/s41563-018-0150-1.

37. *Formation of a TiO_2 Micronetwork on a UV-Absorbing SiO_2-Based Glass Surface by Excimer Laser Irradiation.* **A. Narazaki, Y. Kawaguchi, H. Niino, M. Shojiya, H. Koyo and K. Tsunetomo** 2005, Chem. Mater., Vol. 17, pp. 6651, DOI: https://doi.org/10.1021/cm0518372.

38. *Silicon Monoxide, Monox.* **H. N. Potter.** 1907, Trans. Electrochem. Soc., Vol. 12, p. 191.

39. *Silicon Monoxide Protected Front-Surface Mirrors .* **G. Hass and N. W. Scott** 1949, J. Opt. Soc. Am., Vol. 39, pp. 179, DOI: https://doi.org/10.1364/JOSA.39.000179.

40. *Optical Properties of Silicon Monoxide in the Wavelength Region from 0.24 to 14.0 Microns.* **G. Hass and C. D. Salzberg** 1954, J. Opt. Soc. Am., Vol. 44, pp. 181, DOI: https://doi.org/10.1364/JOSA.44.000181.

41. *Darstellung, Charakterisierung und Oberflächenmodifizierung von Siliziumnanopartikeln in SiO_2.* **U. Kahler** 2001, Dissertation, DOI: http://dx.doi.org/10.25673/2920.

42. *Structure of Amorphous Silicon Monoxide.* **J. A. Yasaitis and R. Kaplow** 1974, J. Appl. Phys., Vol. 43, pp. 995, DOI: https://doi.org/10.1063/1.1661320.

43. *Optical properties of non-crystalline Si, SiO, SiO_x and SiO_2.* **H. R. Philipp** 1971, J. Phys. Chem. Solids, Vol. 32, pp. 1935, DOI: https://doi.org/10.1016/S0022-3697(71)80159-2.

44. *An interface clusters mixture model for the structure of amorphous silicon monoxide (SiO).* **A. Hohl, T. Wieder, P. A. van Aken, T. E. Weirich, G. Denninger, M. Vidal, S. Oswald, C. Deneke, J. Mayer and H. Fuess** 2003, J Non-Cryst. Solids, Vol. 320, pp. 255, DOI: https://doi.org/10.1016/S0022-3093(03)00031-0.

45. *Atomic-scale disproportionation in amorphous silicon monoxide.* **A. Hirata, S. Kohara, T. Asada, M. Arao, C. Yogi, H. Imai, Y. Tan, T. Fujita and M. Chen** 2016, Nat. Commun., Vol. 7, pp. 11591, DOI: https://doi.org/10.1038/ncomms11591.

46. *The Lycurgus Cup - A Roman Nanotechnology.* **I. Freestone, N. Meeks, M. Sax and C. Higgitt** 2007, Gold Bulletin, Vol. 40, pp. 270, DOI: https://doi.org/10.1007/BF03215599.

47. *Optical properties of metal clusters.* **U. Kreibig and M. Vollmer.** Berlin Heidelberg New York : Springer, 1993. ISBN 3-540-57836-6.

48. *Surface-Enhanced Raman Spectroscopy.* **P. L. Stiles, J. A. Dieringer, N. C. Shah and R. P. Van Duyne** 2008, Annu. Rev. Anal. Chem., Vol. 1, pp. 601, DOI: https://doi.org/10.1146/annurev.anchem.1.031207.112814.

49. *Why gold nanoparticles are more precious than pretty gold: Noble metal surface plasmon resonance and its enhancement of the radiative and nonradiative properties of nanocrystals of different shapes.* **S. Eustis and M. A. El-Sayed** 2005, Chemical Society Reviews, Vol. 35, pp. 209, DOI: https://doi.org/10.1039/B514191E.

50. *Effect of particle size distributions on absorbance spectra of gold nanoparticles.* **J. Doak, R. K. Gupta, K. Manivannan, K. Ghosh and P. K. Kahol** 2010, Physica E, Vol. 42, pp. 1605, DOI: https://doi.org/10.1016/j.physe.2010.01.004.

51. *Laser induced morphological and optical properties changes in Au doped aluminum oxide and silicon oxide thin films.* **N. N. Nedyalkov, Y. Nakajima, A. Takami, M. Koleva, D. Karashanova and M. Terakawa** 2016, Optics & Laser Technology, Vol. 79, pp. 179, DOI: https://doi.org/10.1016/j.optlastec.2015.12.008.

52. *Ag/Na ion exchange in soda-lime glasses and the formation of small Ag nanoparticles.* **M. Dubiel, J. Haug, H. Kruth, H. Hofmeister and K.-D. Schicke** 2008, Materials Science and Engineering: B, Vol. 149, pp. 146, DOI: https://doi.org/10.1016/j.mseb.2007.11.035.

53. *Silver diffusion and precipitation of nanoparticles in glass by ion implantation.* **M. Dubiel, H. Hofmeister, G. L. Tan, K.-D. Schicke and E. Wendler** 2003, Eur. Phys. J. D, Vol. 24, pp. 361, DOI: https://doi.org/10.1140/epjd/e2003-00178-5.

54. *Thermostimulated implantation of nanoscaled Ag particles into a quartz glass using a CO_2 laser beam.* **L. A. Ageev, V. K. Miloslavsky, E. D. Makovetsky, K. S. Beloshenko and A. V. Stronsky** 2007, Funct. Mater., Vol. 14, pp. 24, URI: http://dspace.nbuv.gov.ua/handle/123456789/136425 .

55. *Excimer Laser Induced Spatially Resolved Formation and Implantation of Plasmonic Particles in Glass.* **M. Heinz, H. Meinertz, M. Dubiel and J. Ihlemann** 2018, Nanomaterials, Vol. 8, pp. 1035, DOI: http://dx.doi.org/10.3390/nano8121035.

56. *Laser implantation of plasmonic nanostructures into glass.* **S. J. Henley, M. J. Beliatis, V. Stolojan and S. R. P. Silva** 2013, Nanoscale, Vol. 5, pp. 1054, DOI: https://doi.org/10.1039/C2NR33629D.

57. *Glass marking by laser transfer implantation (LTI) of plasmonic nanoparticles.* **J. Ihlemann, L. J. Richter, J. Meinertz, J. Wunderlich, N. Schindler, A. Günther, B. Oberleiter and T. Rainer** 2022, Optics and Laser Technology, Vol. 155, pp. 108371, DOI: https://doi.org/10.1016/j.optlastec.2022.108371.

58. *Implantation of plasmonic nanoparticles in SiO_2 by pulsed laser irradiation of gold films on SiO_x-coated fused silica and subsequent thermal annealing.* **H. Stolzenburg, P. Peretzki, N. Wang, M. Seibt and J. Ihlemann** 2016, Appl. Surf. Sci., Vol. 374, pp. 138, DOI: https://doi.org/10.1016/j.apsusc.2015.10.092.

59. *Studies on CO_2 laser marking.* **M. Ueda, Y. Saitoh, H. Hachisuka, H. Ishigaki, Y. Gokoh and H. Mantani** 1990, Optics and Lasers in Engineering, Vol. 12, pp. 245, DOI: https://doi.org/10.1016/0143-8166(90)90020-A.

60. *Fast fabrication of diffractive patterns on glass by excimer laser ablation.* **J. Meinertz, A. Gödecke, L. J. Richter and J. Ihlemann** 2022, Optics & Laser Technology, Vol. 152, pp. 108148, DOI: https://doi.org/10.1016/j.optlastec.2022.108148.

61. *New process of tempering color printed glass by using laser irradiation.* **L. Altan and G. Waibel** 2018, Procedia CRIP, Vol. 74, pp. 390, DOI: https://doi.org/10.1016/j.procir.2018.08.154.

62. *Cisco Visual Networking Index.* **CISCO Systems.** 2008-2018, Visited 07.03.2023: URL - https://www.cisco.com.

63. *Uptime Institute global data center survey 2020.* **Uptime Institute.** 2020, Visited 07.03.2023: URL - https://uptimeinstitute.com/2020-data-center-industry-survey-results.

64. *Silicon Nanophotonics.* **L. Khriachtchev.** Singapore : Pan Stanford Publishing, 2009. ISBN 978-981-4241-11-3.

65. *Silicon nanocrystals.* **L. Pavesi and R. Turan.** Weinheim : Wiley-VCH, 2010. ISBN 978-3-527-32160-5.

66. *Enhanced Radiative Recombination of Free Excitons in GaAs Quantum Walls.* **B. Deveaud, F. Clérot, N. Roy, K. Satzke, B. Sermage and D. S. Katzer** 1991, Phys. Rev. Lett., Vol. 67, pp. 2355, DOI: https://doi.org/10.1103/PhysRevLett.67.2355.

67. *Optical Gain in Silicon Nanocrystals.* **L. Pavesi, L. Dal Negro, C. Mazzoleni, G. Franzò and F. Priolo** 2000, Nature, Vol. 408, pp. 440, DOI: https://doi.org/10.1038/35044012.

68. *Silicon-Based Light Sources for Silicon Integrated Circuits.* **L. Pavesi** 2008, Advances in Optical Technologies, pp. 12, DOI: https://doi.org/10.1155/2008/416926.

69. *Experimentalphysik 3 : Atome, Moleküle und Festkörper.* **W. Demtröder.** Heidelberg : Springer, 2010. ISBN 978-3-642-03910-2.

70. *Red spectral shift and enhanced quantum efficiency in phonon-free photoluminescence from silicon nanocrystals.* **W. D. A. M. de Boer, D. Timmermann, K. Dohnalová, I. N. Yassievich, H. Zhang, W. J. Buma and T. Gregorkiewicz** 2010, Nature Nanotech, Vol. 5, pp. 878, DOI: https://doi.org/10.1038/nnano.2010.236.

71. *Elucidation of the surface passivation role on the photoluminescence emission yield of silicon nanocrystals embedded in SiO_2.* **M. López, B. Garrido, C. García, P. Pellegrino, A. Pérez-Rodríguez and J. R. Morante** 2002, Appl. Phys. Lett., Vol. 80, pp. 1637, DOI: https://doi.org/10.1063/1.1456970.

72. *Synthesis, properties, and applications of silicon nanocrystals.* **L. Mangolini** 2013, J. Vac. Sci. Technol. B, Vol. 31, pp. 020801, DOI: https://doi.org/10.1116/1.4794789.

73. *Emission Mechanisms of Si Nanocrystals and Defects in SiO_2 Materials.* **J. A. Rodríguez, M. A. Vásquez-Agustín, A. Morales-Sánchez and M. Aceves-Mijares** 2014, Journal of Nanomaterials, Article ID 409482, DOI: https://doi.org/10.1155/2014/409482.

74. *Revisiting an Ongoing Debate: What Role Do Surface Groups Play in Silicon Nanocrystal Photoluminescence?* **R. Sinelnkov, M. Dasog, J. Beamish, A. Meldrum and J. G. C. Veinot** 2017, ACS Photonics, Vol. 4, pp. 1920, DOI: https://doi.org/10.1021/acsphotonics.7b00102.

75. *Size-controlled highly luminescent silicon nanocrystals: A SiO/SiO_2 superlattice approach.* **M. Zacharias, J. Heitmann, R. Scholz and U. Kahler** 2002, Appl. Phys. Lett., Vol. 80, pp. 661, DOI: https://doi.org/10.1063/1.1433906.

76. *Role of the internal strain on the incomplete Si/SiO_2 phase separation in substoichiometric silicon oxide films.* **A. La Magna, G. Nicotra, C. Bongiorno and C. Spinella, M. G. Grimaldi and E. Rimini** 2007, Appl. Phys. Lett., Vol. 90, pp. 183101, DOI: https://doi.org/10.1063/1.2734398.

77. *Generation of silicon nanocrystals by damage free continuous wave laser annealing of substrate-bound SiO_x films.* **T. Fricke-Begemann, N. Wang, P. Peretzki, M. Seibt and J. Ihlemann** 2015, J. Appl. Phys., Vol. 118, pp. 124308, DOI: https://doi.org/10.1063/1.4931670.

78. *Spectroscopic ellipsometry analyses of sputtered Si/SiO_2 nanostructures.* **S. Charvet, R. Madelon, F. Gourbilleau and R. Rizk** 1999, J. Appl. Phys., Vol. 85, pp. 4032, DOI: https://doi.org/10.1063/1.370307.

79. *The origin of photoluminescence from thin films of silicon-rich silica.* **A. J. Kenyon, P. F. Trwoga, C. W. Pitt and G. Rehm** 1996, J. Appl. Phys., Vol. 79, pp. 9291, DOI: https://doi.org/10.1063/1.362605.

80. *Semiconductor Nanophotonics Materials, Models, and Devices.* **M. Kneissl, A. Knorr, S. Reitzenstein and A. Hoffmann** Berlin : Springer, 2020, Vol. 194. ISBN 978-3-030-35655-2.

81. *Enhanced Radiative Emission Rate and Quantum Efficiency in Coupled Silicon Nanocrystal-Nanostructured Gold Emitters.* **J. S. Biteen, D. Pacifici, N. S. Lewis and H. Atwater** 2005, Nano Letters, Vol. 5, pp. 1768, DOI: https://doi.org/10.1021/nl051207z.

82. *Quenching of Si nanocrystal photoluminescence by doping with gold or phosphorous.* **A. L. Tchebotareva, M. J. A. de Dood, J. S. Biteen, H. A. Atwater and A. Polman** 2005, J. Lumin., Vol. 114, pp. 137, DOI: https://doi.org/10.1016/j.jlumin.2004.12.014.

83. *Field-effect electroluminescence in silicon nanocrystals.* **R. J. Walters, G. I. Bourianoff and H. A. Atwater** 2005, Nature Mater., Vol. 4, pp. 143, DOI: https://doi.org/10.1038/nmat1307.

84. *Plasmonic engineering of spontaneous emission from silicon nanocrystals.* **J. Goffard, D. Gérad, P. Miska, A.-L. Baudrion, R. Deturche and J. Plain** 2013, Sci. Rep., Vol. 3, pp. 2672, DOI: https://doi.org/10.1038/srep02672.

85. *Influence of Gold Nanoantennas on the Photoluminescence of Silicon Nanocrystals.* **R. Köthemann, C. Golla, H. Qu and C. Meier** 2022, Photonics, Vol. 9, pp. 985, DOI: https://doi.org/10.3390/photonics9120985.

86. *Twenty-fold plasmon-induced enhancement of radiative emission rate in silicon nanocrystals embedded in silicon dioxide.* **S. Gardelis, V. Gianneta and A. G. Nassiopoulou** 2016, J. Lumin., Vol. 170, pp. 282, DOI: https://doi.org/10.1016/j.jlumin.2015.10.029.

2. Manuscripts

In this chapter, the three manuscripts of the cumulative dissertation are presented. Information on the publication of the manuscripts in the respective journals is given. The main aspects of the manuscript are summarized. The share of the work of the individual authors in the preparation of the manuscript is indicated for each manuscript.

2.1 UV laser generated micro structured black surface on commercial TiO_2-containing glass

This manuscript was published by the authors Lukas Janos Richter, Clemens Martin Beckmann and Jürgen Ihlemann under the title "*UV laser generated micro structured black surface on commercial TiO_2-containing glass*" in the journal *Applied Surface Science* (Volume 601) by the publisher Elsevier in November 2022. It is available on the website https://www.sciencedirect.com/science/article/abs/pii/S0169433222017664 or under the digital object identifier (DOI) *10.1016/j.apsusc.2022.154231*. The article is licensed by Elsevier.

The formation of a micro-structured, black surface upon excimer laser irradiation of $\mathrm{TiO_2}$-containing glasses is demonstrated. The process is based on a phase separation of Ti- and Si-rich phases accompanied by a partial reduction of $\mathrm{TiO_2}$ to $\mathrm{TiO_x}$. It requires neither vacuum nor a special gas environment. Widely used, commercially available glass types are used. The research considers material properties on the atomic and molecular level, based on experimental investigations by energy dispersive X-ray spectroscopy and Raman spectroscopy. The possible application of the studied process for glass marking is addressed.

The share of the authors work in the preparation of the manuscript is as follows: The planning of the experiments was done by Lukas Janos Richter (LJR), Clemens Martin Beckmann (CMB) and Jürgen Ihlemann (JI). LJR carried out the laser, cleaning and oven experiments. LJR did the microscope, transmission, SEM and Raman analysis and performed the processing of these data and the preparation of the respective figures. CMB carried out the EDX measurements and performed the processing of the EDX data and the preparation of the EDX figures. LJR, CMB and JI discussed the measurement results. JI wrote the original draft. Revision and correction of the final manuscript was done by LJR, CMB and JI.

The authors declare the following financial interests/personal relationships which may be considered as potential competing interests: LJR, CMB, JI have patent pending to Institut für Nanophotonik Göttingen e.V.

Applied Surface Science 601 (2022) 154231

Contents lists available at ScienceDirect

Applied Surface Science

journal homepage: www.elsevier.com/locate/apsusc

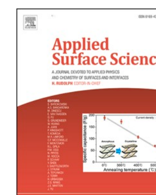

Full Length Article

UV laser generated micro structured black surface on commercial TiO_2-containing glass

Lukas Janos Richter, Clemens M. Beckmann, Jürgen Ihlemann *

Institut für Nanophotonik Göttingen e.V., Göttingen, Germany

ARTICLE INFO

Keywords:
TiO_2-containing glass
Excimer laser
Surface micro structure
Black marking

ABSTRACT

ArF excimer laser (193 nm, 20 ns) irradiation of commercially available TiO_2-containing glasses in ambient air leads to a darkening of the surface and a bumpy surface micro structure. This process goes along with a phase separation between silicon-rich and titanium-rich phase near the glass surface. The black appearance can be attributed to the light scattering of the micro structured surface and absorption due to partial reduction of the titanium oxide. The process can be applied for marking the glass surface with high contrast.

1. Introduction

Laser functionalization of glass surfaces has developed into many directions. Laser based deposition of coatings [1], ablation patterning [2], polishing [3], roughening [4], nanoparticle implantation [5], and phase separation [6] are examples of such processes. These processes are applied for glass marking, modifying the wettability, creating self-cleaning or biocompatible surfaces, or generating optical functionalities like antireflection or wave guiding. Laser processes provide the possibility of integrated functionalization in microfluidic chips [7]. Of special interest are processes that go along without adding supplementary material which would increase the complexity of the process and could promote wear or damage of the glass surface. Laser induced periodic surface structures on glass with sub-wavelength-, wavelength- and supra-wavelength periods have been generated mainly by femtosecond laser irradiation [8,9]. Ordered hill-like structures have been obtained by nanosecond excimer irradiation of glass [10]. One type of glass functionalization is the generation of photocatalytic activity. This has been mainly achieved by special, in many cases TiO_2-based coatings [11,12]. Narazaki et al. have generated a titania enriched surface network on uncoated, custom made Ti-containing glass [13]. They irradiated the glass surface with a KrF excimer laser at 248 nm. The so called laser-induced superficial phase separation leading to a rutile crystalline phase was only obtained for irradiation in helium or nitrogen flow, but not in ambient air atmosphere. The formation of rutile-type TiO_2 inside glass has been demonstrated by femtosecond laser processing [14,15]. The observed darkening of the laser treated regions is well known from the laser treatment of pure TiO_2 films with KrF excimer laser [16], however, in this case mostly the anatase phase of TiO_2 has been observed [17]. The darkening effect is assumed to be due to partial reduction and defect generation (oxygen deficiencies), i.e. sub-stoichiometric titanium oxide in the laser treated area [18,19]. Due to the extension of the optical absorption range, this dark/black titania exhibits a more efficient photocatalytic activity compared to the transparent, fully oxidized TiO_2 [20]. Irradiation of amorphous TiO_2 films at 193 nm leads to anatase formation at low fluence and rutile formation at somewhat higher fluence [21]. The advantage of such laser processes compared to other heating processes is the spatial control of the induced modification, e.g. for applying specific marks or for locally controlled on-chip integration of photocatalytic micro reactors [7].

In this paper we show that this darkening effect can also be obtained on commercially available TiO_2-containing glasses by ArF excimer laser irradiation in ambient air. The process can be applied for marking the glass surface with high resolution and high contrast. Many commercial glasses with high refractive index contain TiO_2 in substantial amounts. This is partly due to the intentions to avoid and substitute lead oxide because this is a “substance of very high concern” (SVHC). Examples treated here are N-F2, SF11, and N-SF11 from Schott. “F” means “flint” and “SF” means “dense flint” (“schweres Flintglas” in German).

High contrast marks on glass are highly desirable as visually detectable or machine readable identifying features for product traceability or fraud protection. Especially in those cases, where the introduction of foreign material into the glass is undesirable or not permitted, for example in medicine (e.g. implantable hermetic glass encapsulations of micro devices) or in pharmaceutical packaging, a method operational without additives is necessary. Such marks in the form of text, codes,

* Corresponding author.
E-mail address: juergen.ihlemann@ifnano.de (J. Ihlemann).

https://doi.org/10.1016/j.apsusc.2022.154231
Received 5 April 2022; Received in revised form 1 July 2022; Accepted 10 July 2022
Available online 12 July 2022
0169-4332/© 2022 Elsevier B.V. All rights reserved.

logos or pictorial elements can be applied for informative or decorative purposes.

2. Materials and methods

Irradiation of polished glass surfaces of Schott SF11, N-SF11, F2 and N-F2 was performed with an ArF excimer laser (Lambda Physik LPXpro, wavelength 193 nm, pulse duration 20 ns) in combination with a mask projection setup (Fig. 1) in ambient air. A homogeneous part of the beam was selected by a circular (3-mm-diameter) or rectangular (2–5 mm side length) aperture, which was imaged on the sample surface by a fused silica lens of 100 mm focal length (demagnification ~ 10:1). The fluence was adjusted by a variable attenuator consisting of a rotatable fused silica plate with a dielectric coating, whose transmission depends on the incident angle. This enables a fluence variation without changing beam or spot size. The fluence was determined by dividing the measured pulse energy reaching the sample by the area of the laser spot. For each glass type (cf. Table 1) a set of irradiation spots under variation of fluence and number of pulses was applied. After laser processing, the samples were cleaned with a KOH-based cleaning agent (Deconex 15PF-x in water (1:2), ultrasonic bath at 50 °C for 10 min) to remove debris from the surface.

The irradiated samples were investigated by optical microscopy (Zeiss Imager.Z2m) and scanning electron microscopy (Zeiss, EVO MA10). Optical transmission of the irradiated samples was measured using a HeNe-Laser and placing a photodetector (Ophir PD 300-3W) close behind the sample, so that nearly all transmitted light including the forward scattered light is collected.

The material composition and its spatial distribution within the irradiated spots was investigated by Raman spectroscopy (XploRA PLUS, Horiba, excitation 532 nm, 35–75 mW, spot size ≤ 3 μm) and by energy dispersive x-ray (EDX) spectroscopy (Bruker Quantax system with an XFlash 410-M detector at 20 kV acceleration voltage of the incident electrons).

3. Results

All Ti-containing glasses exhibit a surface modification in form of a micro-structure and a black appearance after irradiating them with ArF laser pulses at moderate fluences (Fig. 2 (a)). The threshold for this surface modification is around 200 mJ/cm^2 for all glasses; at high fluence substantial material ablation takes place leading to a flat surface (ablation rate 50 – 100 nm/pulse at 1 J/cm^2). Within the fluence range of about 200 to 400 mJ/cm^2, after about 50 pulses some bump pattern evolves, which turns into a pattern of cones or ridges with valleys in between when applying more pulses (Fig. S1 in supplementary material). The "period" of this not strongly periodic pattern as well as the depth of the valley amounts to some μm (Figs. 2, 3).

Table 1
Glass types, their (weight) content of titanium oxide and lead oxide stated in the technical safety information [22] and measured by EDX (this work) and their refractive index n_d at the He d-line. Fluence range of structure formation (at 193 nm).

Schott glass	Titanium oxide		Lead oxide		n_d (587.6 nm)	Structure formation
	[22]	This work	[22]	This work		
SF11	1–10%	4.8%	60–70%	64%	1.785	200–400 mJ/cm^2
N-SF11	20–30%	28%	–	–	1.785	200–450 mJ/cm^2
F2	–	–	40–50%	47%	1.620	–
N-F2	10–20%	15%	–	–	1.620	200–400 mJ/cm^2

For a quantitative analysis of the evolution of the period of the structures with increasing pulse number, 2D-Fast Fourier Transformation (2D-FFT) of the SEM images was performed. Fig. 4 (a) shows the SEM image used here as an example. This image is Fourier transformed, the essential section of this transformation is shown in Fig. 4 (b). It is axially symmetrical, i.e. the pattern shows no preferred direction. The data for the graph in Fig. 4 (c) are determined along the line drawn in red. With these data, the predominant period of the structure is determined by means of the indicated Lorentzian-fits to the side peaks. The periods determined in this way are plotted against the pulse number for the three glasses SF11, N-SF11 and N-F2 in Fig. 4 (d). Starting from a period of 1–3 μm at 30 pulses the pattern evolves to a period of 4–5 μm after 1000 pulses.

These modified spots have a black appearance when looking at the surface with the naked eye as well as under an optical microscope with low NA objective. For comparison, F2-glass, optically very similar to N-F2, but containing no titanium, does not show microstructure formation or darkening.

In order to investigate, to which extent the black appearance is due to light absorption in a surface near layer of the sample or due to scattering by the bumpy surface, transmission experiments have been performed. Irradiating the sample with a HeNe-laser and placing a photodetector close behind the sample, so that nearly all transmitted light including the forward scattered light is collected, a transmission value of 91% is obtained in case of a non-irradiated N-F2 sample (9% loss due to Fresnel reflection). In case of a modified sample (N-F2, 300 mJ/cm^2, 500

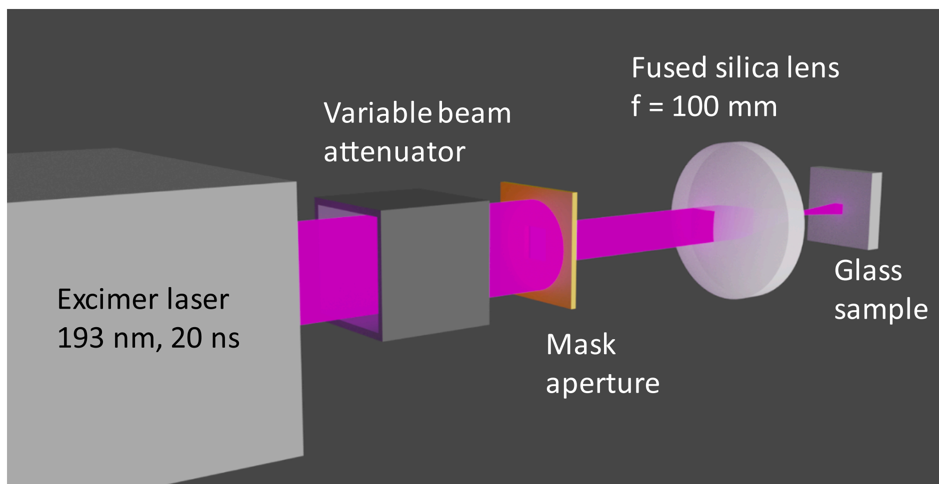

Fig. 1. Setup of the laser irradiation experiments.

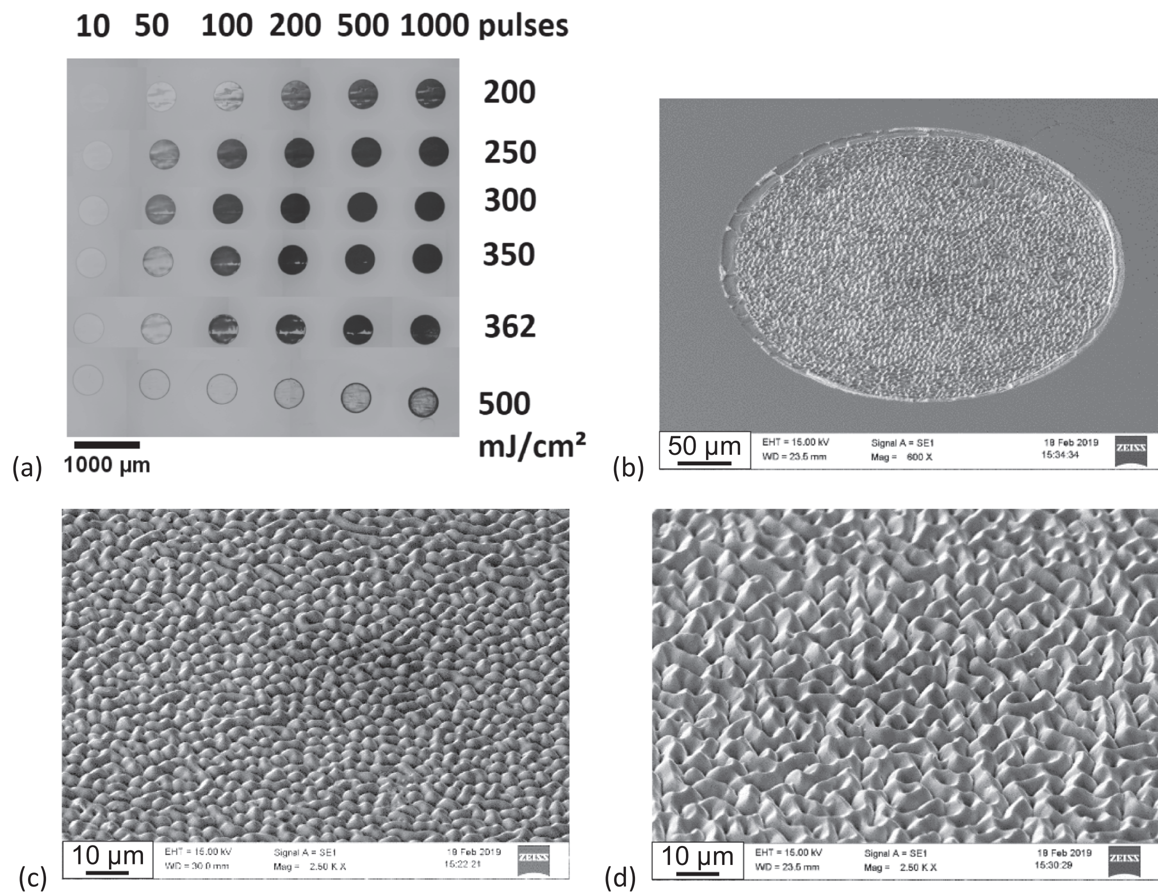

Fig. 2. ArF excimer laser modified surface of N-F2 glass. (a) Microscope image (reflected light) of spots generated under variation of fluence and number of pulses after cleaning. Spot diameter: 450 µm. Background pattern due to stitching modus of image recording. (b)-(d) Scanning electron microscope images of spots irradiated at 250 mJ/cm^2; viewing angle 45°: (b) 1000 pulses overview; (c) 200 pulses; (d) 1000 pulses.

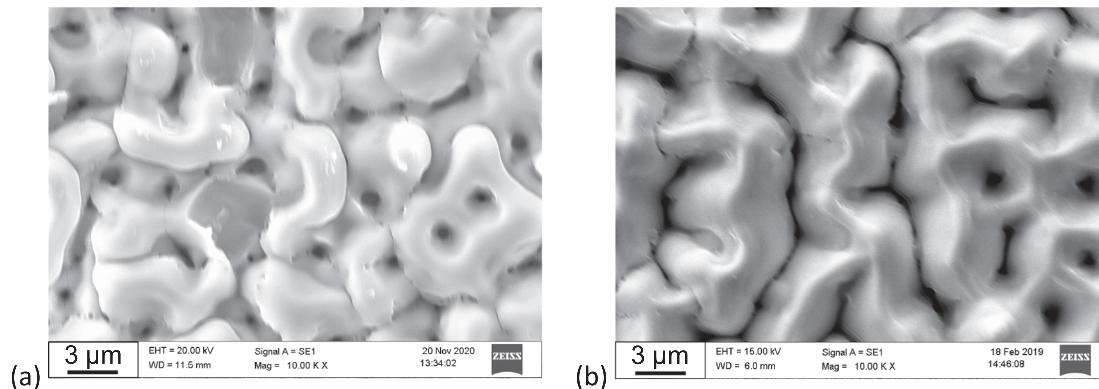

Fig. 3. Scanning electron microscope images of the laser induced surface modification of Ti-containing glass. Laser parameters: 193 nm, 250 mJ/cm^2, 1000 pulses. (a) N-SF11; (b) N-F2.

pulses), a transmission of 43% is obtained. If the photodetector is placed at a greater distance (~1 m) so that the scattered light is not measured, a transmission of almost 0% is measured. Neglecting the differences in reflection of raw and modified sample, this means that roughly half of the light is absorbed and half of it is scattered. This absorption indicates the postulated reduction of TiO_2 to sub-stoichiometric titanium oxide by laser irradiation [18,19]. In order to check the stability of the black appearance, the samples were heated at 500 °C in air. After 24 h, no significant visible change has been observed yet. After 72 h at 500 °C in air, a transmission of 61% has been measured. This increase indicates a re-oxidation of the titanium oxide as similarly observed for TiO_x films in the same temperature range [23]. The microstructure is still present after this heating process, the visible appearance changed from black to light grey to white. A comparison of spots before and after thermal processing is shown in Fig. 5. Further data confirming the re-oxidation are provided in Tab. S1 in the supplementary material.

In order to investigate, whether the structure formation comes along with a phase separation as shown in [13], studies by Raman spectroscopy and by energy dispersive x-ray (EDX) spectroscopy have been performed. Fig. 6 (a) displays the Raman spectra of the three glasses exhibiting structure formation. Two major peaks appearing in all spectra around 430 cm^{-1} and 610 cm^{-1} can be clearly assigned to the rutile

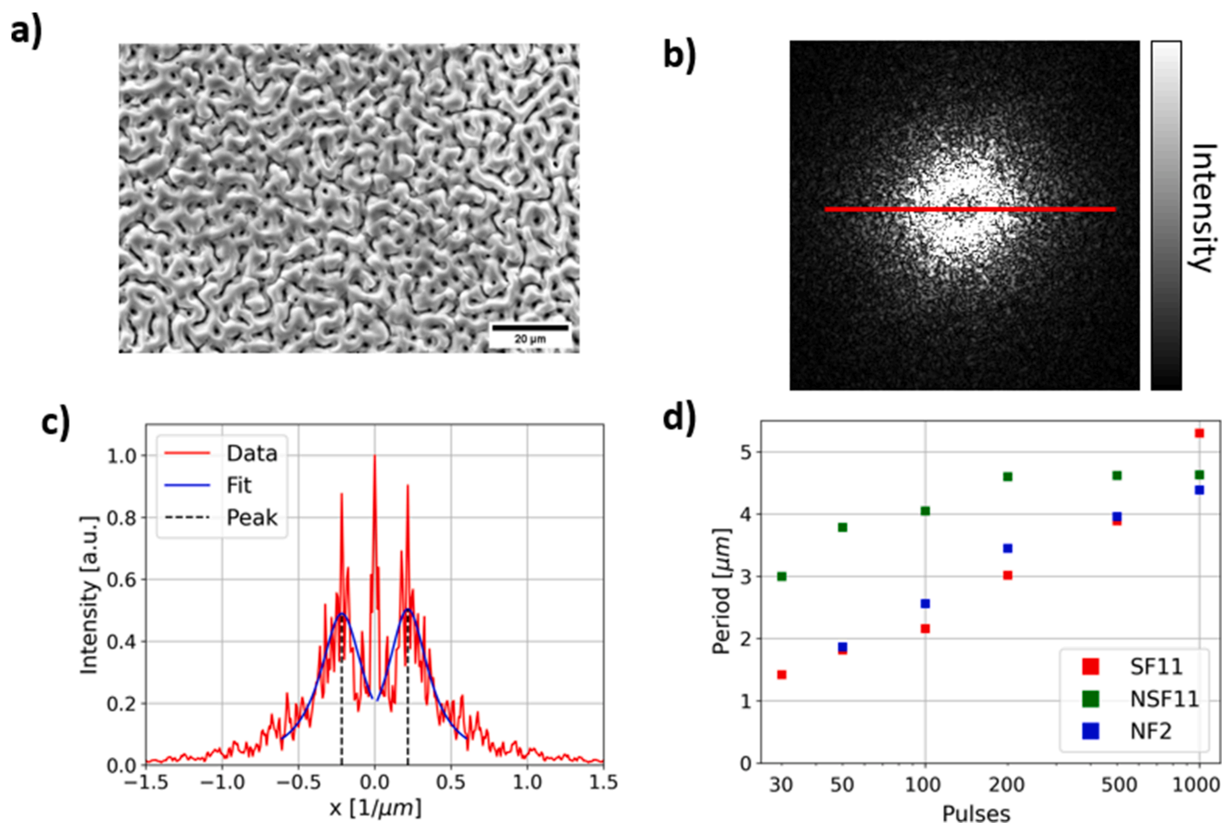

Fig. 4. Period determination by means of 2D-FFT using the example of a structure in N-SF11 glass irradiated with 500 pulses at 300 mJ/cm^2. (a) shows the SEM image of the surface. In (b) the corresponding Fourier transformed image is depicted. Image (c) shows the intensity along the red line indicated in (b). The period of the structure is determined using the peak positions of the Lorentzian fits shown. Graph (d) presents the predominant periods of the three glasses plotted against the pulse number. (For interpretation of the references to colour in this figure legend, the reader is referred to the web version of this article.)

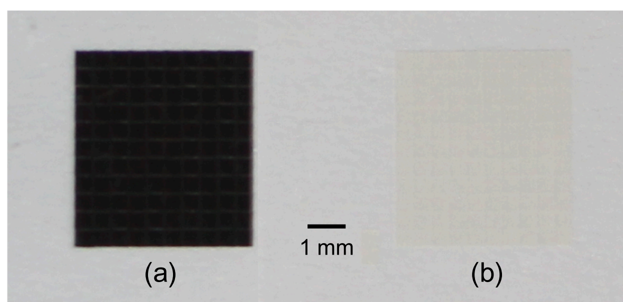

Fig. 5. Photograph of the laser irradiated spots (arrays of 10 × 10 spots) on N-SF11 glass; laser parameters: 300 mJ/cm^2, 200 pulses. (a) as irradiated; (b) irradiated and subsequently heated to 500 °C for 144 h in air.

polymorph of TiO_2 [24,25]. The redshift especially of the 430 cm^{-1}-peak with respect to the tabulated rutile mode at 448 cm^{-1} indicates an oxygen deficiency [26]. Fig. 6 (b) shows that this rutile rich phase is located mainly on the top of the structure. In the valleys a rather unspecific spectrum similar to that of the non-irradiated glass is obtained. The EDX measurements agree very well with these observations. The mappings of the elemental distributions in Fig. 7 demonstrate that the material is separated in a Ti-rich phase (red) near the hills of the structure and a Si-rich phase (green) near the valleys.

4. Discussion

The mechanism of structure formation seems to be very similar to that observed by Narazaki et al. in the case of 248 nm irradiation [13]. They assume that upon laser heating of the glass, the alkali oxide evaporates more easily than TiO_2 and SiO_2, shifting the composition of the glass to a binary SiO_2-TiO_2. At high temperature (around 2000 °C), this system has a wide immiscibility region [27]. Cooling down, at about 1780 °C a rutile crystalline phase and a SiO_2-rich melt is formed. Preferential SiO_2 evaporation during cooling down leads to the formation of TiO_2-rich bumps connecting to a network after repetitive heating cycles by multiple pulses. At the same time, TiO_2 is reduced to TiO_x ($x < 2$) via laser induced formation of oxygen vacancies [18]. A similar phase separation leading to rutile phase TiO_2 has also been obtained by femtosecond laser irradiation of aluminoborate glass containing 20% TiO_2 [14]. In this case the rutile formation inside the glass has been accomplished by the cumulative heating induced by focusing the highly repetitive laser irradiation into the glass.

At 248 nm wavelength, according to Narazaki et al. [13], a flow of He or N_2 is required for structure formation. The authors assume that without this gas flow, debris redeposition will inhibit the process. At 193 nm, we observe phase separation and structure formation in air without gas flow. Presumably, the stronger absorbance of the glass at 193 nm leads to stronger fragmentation and less debris formation. This is also supported by the observation of a very smooth microstructure surface in comparison with the rather porous structure in the case of 248-nm-irradiation.

The laser induced blackening can be applied for the marking of glass surfaces. Black marks are very desirable as they provide high contrast compared to e.g. just flat ablated spots. However, this normally works only by adding some supplementary material like for instance graphite [28], and such additives are highly unwanted in many applications. Fig. 8 displays a black QR-code fabricated with our method on N-SF11 glass. Each pixel has been generated by 200 pulses at 300 mJ/cm^2.

The critical parameters of the method are especially the laser fluence, the laser pulse number and the Ti-content of the glass material.

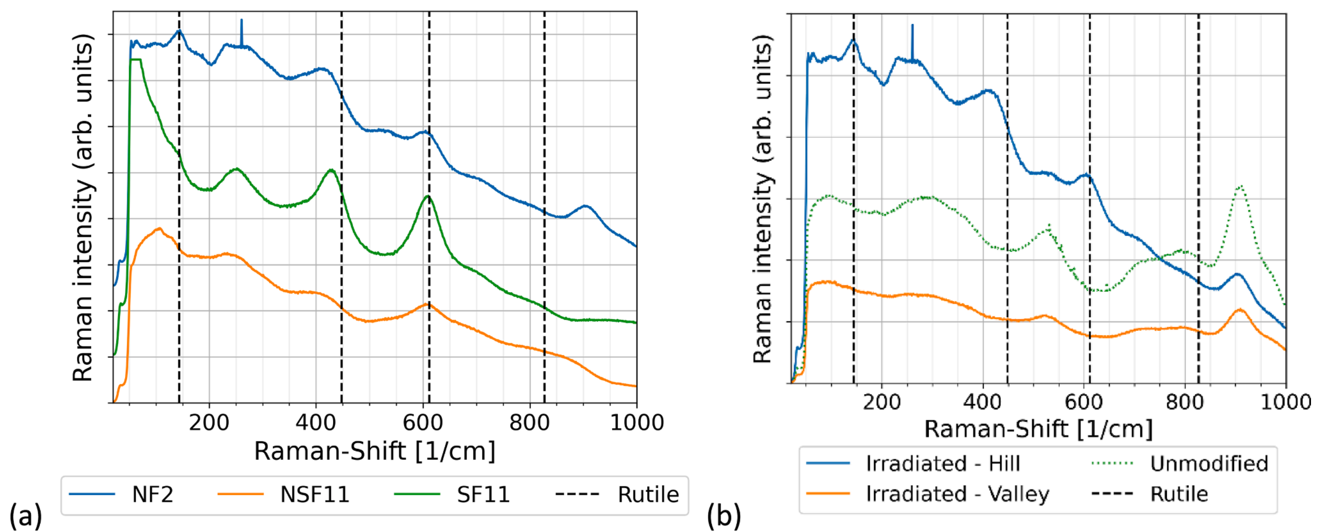

Fig. 6. Raman spectra of surfaces irradiated at a fluence of 300 mJ/cm^2 and 1000 pulses. The dashed lines indicate the Raman peaks of rutile [24,25]. (a) Comparison of the spectra of the three glasses showing structure formation (recorded on the hills). (b) Spectra of N-F2 recorded on a hill of the structure (blue), in the valley of the structure (orange), and in a non-irradiated, flat surface (green). (For interpretation of the references to colour in this figure legend, the reader is referred to the web version of this article.)

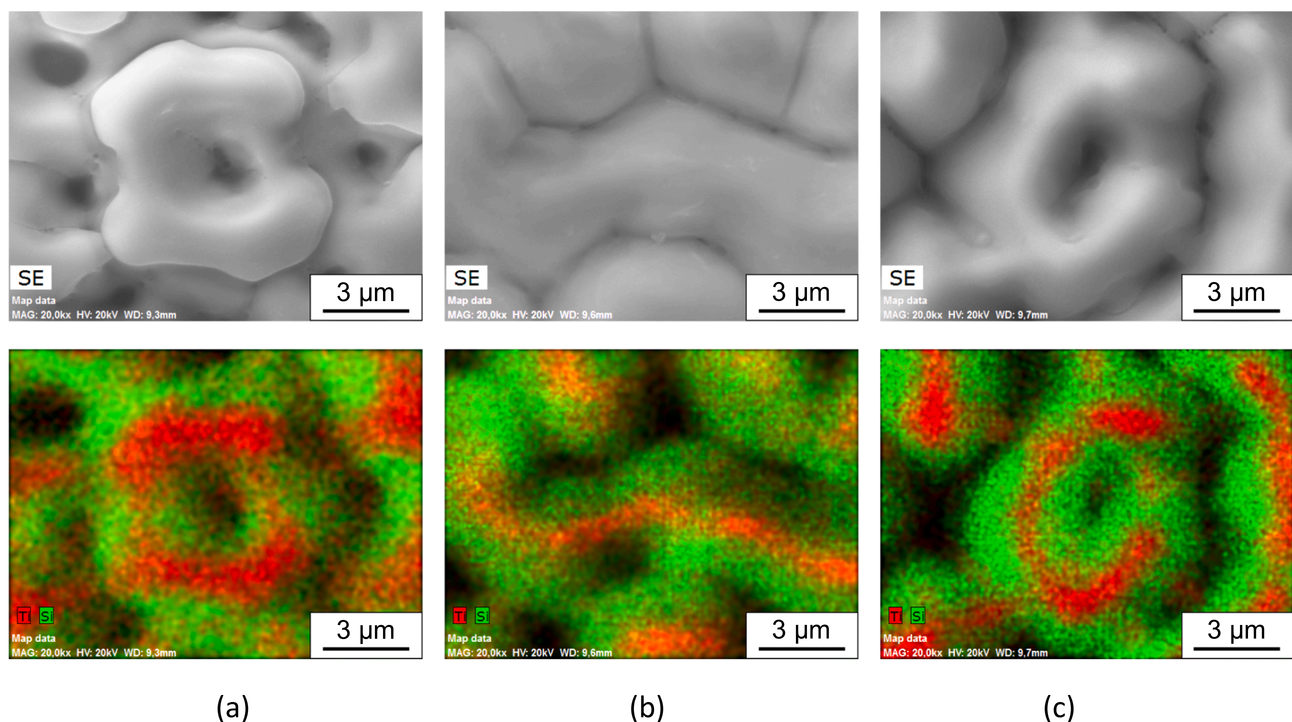

Fig. 7. Scanning electron micrographs and corresponding element mappings (Ti: red, Si: green) of the laser irradiated surfaces recorded by EDX. (a) N-SF11, 193 nm, 250 mJ/cm^2, 1000 pulses. (b) SF11, 193 nm, 300 mJ/cm^2, 1000 pulses. (c) N-F2, 193 nm, 260 mJ/cm^2, 1000 pulses. (For interpretation of the references to colour in this figure legend, the reader is referred to the web version of this article.)

The influence of laser fluence and laser pulse number on the blackening can be seen in Fig. S2 in the supplementary material. Below about 200 mJ/cm^2, the glass shows no significant change. Above about 450 mJ/cm^2, substantial material ablation is observed, i.e. successive pulses will remove the modified material caused by the preceding pulses. At low laser pulse numbers ($<$100 pulses), only a weak material change occurs. If the TiO_2-content is too low, the method does not work either. About 5% TiO_2 seems to be sufficient (c.f. SF11, table 1), but for example another glass, Schott SSK2, which contains 1.5% TiO_2, shows only a rather weak blackening effect.

5. Conclusion

ArF excimer laser (193 nm) irradiation of Ti containing, commercially available glasses with fluences near the ablation threshold leads to the development of a surface microstructure and a black appearance. In contrast to the case using a KrF laser (248 nm), this process can be accomplished in a standard air environment and does not require vacuum or inert gas. It is based on a phase separation into Ti-rich and Si-rich phases and a partial reduction of TiO_2 to sub-stoichiometric TiO_x. The blackening is stable and can be used for the marking of glass surfaces.

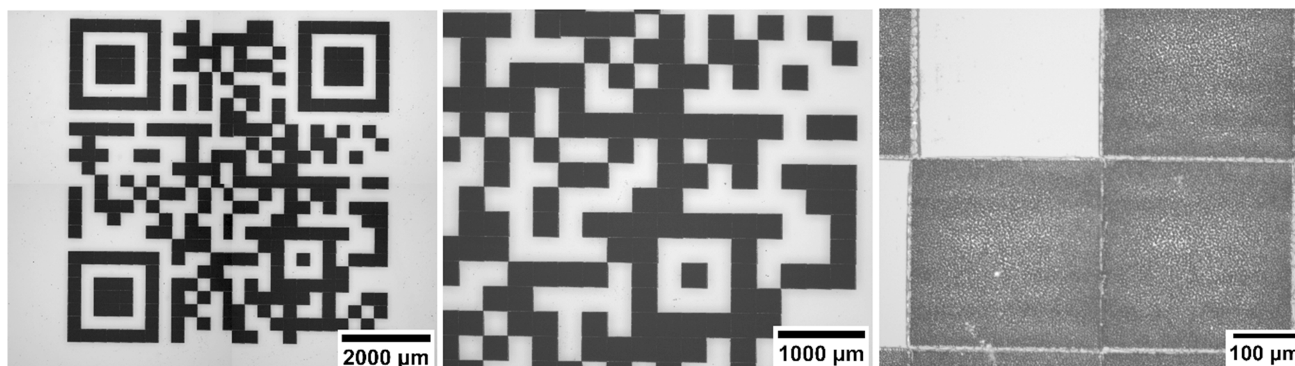

Fig. 8. Microscope images of a QR code made by laser modification of N-SF11 glass. Laser parameters: 193 nm, 300 mJ/cm^2, 200 pulses/pixel.

CRediT authorship contribution statement

Lukas Janos Richter: Methodology, Validation, Formal analysis, Investigation, Writing – review & editing, Visualization. **Clemens M. Beckmann:** Methodology, Formal analysis, Investigation, Writing – review & editing, Visualization. **Jürgen Ihlemann:** Conceptualization, Writing – original draft, Writing – review & editing, Supervision, Project administration.

Declaration of Competing Interest

The authors declare the following financial interests/personal relationships which may be considered as potential competing interests: LJR, CMB, JI have patent pending to Institut für Nanophotonik Göttingen e.V.

Appendix A. Supplementary data

Supplementary data to this article can be found online at https://doi.org/10.1016/j.apsusc.2022.154231.

References

[1] F. Craciun, T. Lippert, M. Dinescu, Pulsed Laser Deposition: Fundamentals, Applications, and Perspectives, 2020.
[2] R. Karstens, A. Gödecke, A. Prießner, J. Ihlemann, Fabrication of 250-nm-hole arrays in glass and fused silica by UV laser ablation, Opt. Laser Technol. 83 (2016) 16–20, https://doi.org/10.1016/j.optlastec.2016.03.020.
[3] C. Weingarten, A. Schmickler, E. Willenborg, K. Wissenbach, R. Poprawe, Laser polishing and laser shape correction of optical glass, J. Laser Appl. 29 (1) (2017), 011702, https://doi.org/10.2351/1.4974905.
[4] M. Domke, G. Sonderegger, E. Kostal, V. Matylitsky, S. Stroj, Transparent laser-structured glasses with superhydrophilic properties for anti-fogging applications, Appl. Phys. A Mater. Sci. Process. 125 (10) (2019) 1–10, https://doi.org/10.1007/s00339-019-2953-6.
[5] M. Heinz, J. Meinertz, M. Dubiel, J. Ihlemann, Excimer laser induced spatially resolved formation and implantation of plasmonic particles in glass, Nanomaterials 8(12) (2018), doi: 10.3390/NANO8121035.
[6] M. Shimizu, et al., Space-selective phase separation inside a glass by controlling compositional distribution with femtosecond-laser irradiation, Appl. Phys. A Mater. Sci. Process. 100 (4) (2010) 1001–1005, https://doi.org/10.1007/s00339-010-5879-6.
[7] H. Wang, Y.L. Zhang, W. Wang, H. Ding, H.B. Sun, On-chip laser processing for the development of multifunctional microfluidic chips, Laser Photonics Rev. 11(2) (2017), doi: 10.1002/lpor.201600116.
[8] G. Seifert, M. Kaempfe, F. Syrowatka, C. Harnagea, D. Hesse, H. Graener, Self-organized structure formation on the bottom of femtosecond laser ablation craters in glass, Appl. Phys. A Mater. Sci. Process. 81 (4) (2005) 799–803, https://doi.org/10.1007/s00339-004-2867-8.
[9] S. Gräf, C. Kunz, F.A. Müller, Formation and properties of laser-induced periodic surface structures on different glasses, Materials (Basel). 10(8) (2017), doi: 10.3390/ma10080933.
[10] S. Panahibakhsh, S. Jelvani, M. Jaberi, Micro- and nanostructures formation on glass surface with different parameters of excimer laser irradiation, Opt. Eng. 58 (01) (2018) 1, https://doi.org/10.1117/1.oe.58.1.011005.
[11] C.H.A. Tsang, et al., Titanium oxide based photocatalytic materials development and their role of in the air pollutants degradation: Overview and forecast, Environ. Int. 125 (January) (2019) 200–228, https://doi.org/10.1016/j.envint.2019.01.015.
[12] Y. Hendrix, A. Lazaro, Q. Yu, J. Brouwers, Titania-Silica Composites: A Review on the Photocatalytic Activity and Synthesis Methods, World J. Nano Sci. Eng. 05 (04) (2015) 161–177, https://doi.org/10.4236/wjnse.2015.54018.
[13] A. Narazaki, Y. Kawaguchi, H. Niino, M. Shojiya, H. Koyo, K. Tsunetomo, Formation of a TiO2 micronetwork on a UV-absorbing SiO 2-based glass surface by excimer laser irradiation, Chem. Mater. 17 (26) (2005) 6651–6655, https://doi.org/10.1021/cm0518372.
[14] Y. Liu, et al., Femtosecond laser direct writing of TiO2 crystalline patterns in glass, Appl. Phys. B Lasers Opt. 93 (2–3) (2008) 613–617, https://doi.org/10.1007/s00340-008-3166-4.
[15] P. Zhou, H. Ma, Y. Du, Y. Han, B. Lu, M. Zhong, Three-dimension direct writing TiO2 crystalline patterns in Bi-free glass using femtosecond laser, Appl. Phys. A Mater. Sci. Process. 102 (2) (2011) 295–299, https://doi.org/10.1007/s00339-010-6112-3.
[16] H.Y. Zheng, H.X. Qian, W. Zhou, Analyses of surface coloration on TiO 2 film irradiated with excimer laser, Appl. Surf. Sci. 254 (7) (2008) 2174–2178, https://doi.org/10.1016/j.apsusc.2007.09.005.
[17] O. Van Overschelde, R. Snyders, M. Wautelet, Crystallisation of TiO 2 thin films induced by excimer laser irradiation, Appl. Surf. Sci. 254 (4) (2007) 971–974, https://doi.org/10.1016/j.apsusc.2007.08.018.
[18] C. Sol, R.J.D. Tilley, Ultraviolet laser irradiation induced chemical reactions of some metal oxides, J. Mater. Chem. 11 (3) (2001) 815–820, https://doi.org/10.1039/b006787n.
[19] K. Starbova, V. Yordanova, D. Nihtianova, W. Hintz, J. Tomas, N. Starbov, Excimer laser processing as a tool for photocatalytic design of sol-gel TiO 2 thin films, Appl. Surf. Sci. 254 (13) (2008) 4044–4051, https://doi.org/10.1016/j.apsusc.2007.12.036.
[20] V.A. Glezakou, R. Rousseau, Shedding light on black titania, Nat. Mater. 17 (10) (2018) 856–857, https://doi.org/10.1038/s41563-018-0150-1.
[21] P. Mitrev, G. Benvenuti, P. Hofman, A. Smirnov, N. Kaliteevskaya, R. Seĭsyan, Phase transitions in thin titanium oxide films under the action of excimer laser radiation, Tech. Phys. Lett. 31 (11) (2005) 908–911, https://doi.org/10.1134/1.2136949.
[22] Schott, Technical Safety Information, Data files: SF11_SDS_EN_V5_201505, N-SF11_SDS_EN_V5_201505, F2_SDS_EN_V5_201505, N-F2_SDS_EN_V5_201505, 2015.
[23] R.A. Henning, et al., Phase formation and stability in TiOx and ZrOx thin films: Extremely sub-stoichiometric functional oxides for electrical and TCO applications, Zeitschrift fur Krist. - Cryst. Mater. 232 (1–3) (2017) 161–183, https://doi.org/10.1515/zkri-2016-1981.
[24] S.P.S. Porto, P.A. Fleury, T.C. Damen, Raman Spectra of TiO2, MgF2, ZnF2, FeF2, and MnF2, Phys. Rev. 154 (2) (1967) 522.
[25] U. Balachandran, N.G. Eror, Raman Spectra of Titanium Dioxide, J. Solid State Chem. 42 (1982) 276–282.
[26] R.W. Parker, J.C. Siegel, Raman microprobe study of nanophase TiO2 and oxidation-induced spectral changes, J. Mater. Res. 5 (1990) 1246, doi: https://doi.org/10.1557/JMR.1990.1246.
[27] K.I. Katsumata, Y. Kameshima, K. Okada, A. Yasumori, Preparation of phase-separated textures and crystalline phases from two-liquid immiscible melts in the TiO2-SiO2 system, Mater. Res. Bull. 39 (7–8) (2004) 1131–1139, https://doi.org/10.1016/j.materresbull.2004.02.011.
[28] W. Jiang, X.Z. Xie, X. Wei, W. Hu, Q.L. Ren, Z.S. Zou, High contrast patterning on glass substrates by 1064 nm pulsed laser irradiation, Opt. Mater. Express 7 (5) (2017) 1565, https://doi.org/10.1364/ome.7.001565.

UV laser generated micro structured black surface on commercial TiO_2-containing glass

Lukas Janos Richter, Clemens M. Beckmann, Jürgen Ihlemann

Institut für Nanophotonik Göttingen e.V., Göttingen, Germany

Supplementary material

300 mJ/cm2 | N-SF11 | SF11 | N-F2

30 pulses

50 pulses

100 pulses

200 pulses

500 pulses

1000 pulses

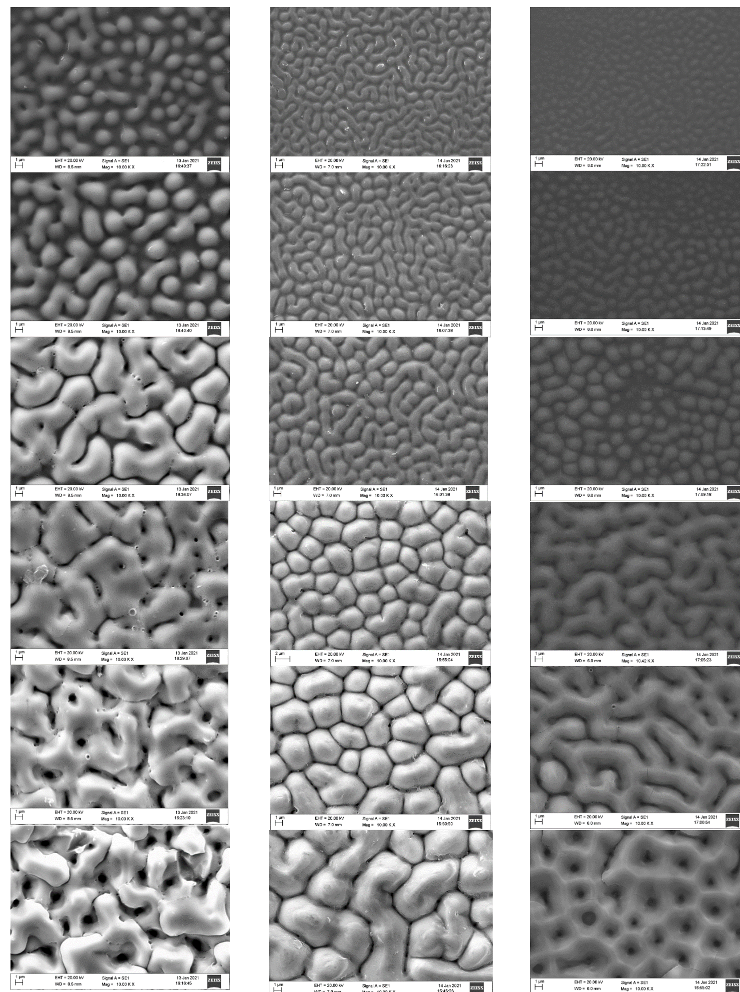

Fig. S1: Scanning electron microscope images of laser generated surface patterns on various glasses after increasing number of pulses at a fluence of 300 mJ/cm².

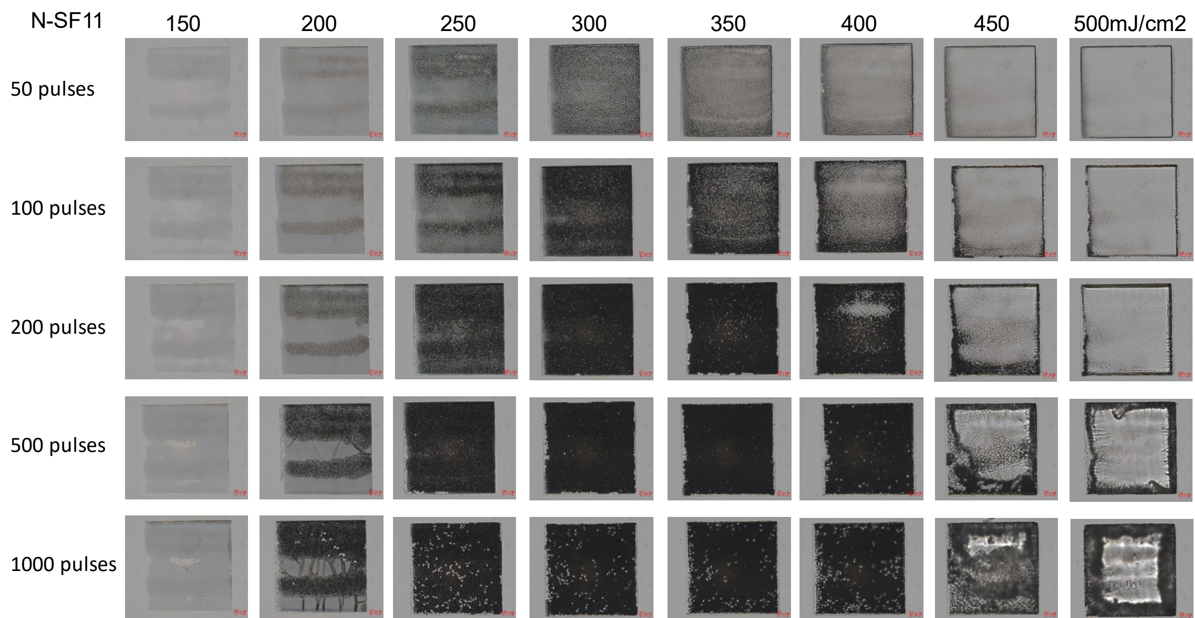

Fig. S2: Optical microscope images of laser generated spots on N-SF11 glass for various fluences and numbers of pulses. (Transmitted light, 50x, NA = 0.95.)

Table S2: Optical transmission data of laser irradiated spots on N-SF11 before (as prepared) and after thermal processing in air. Laser fluence: 300 mJ/cm². Measurement in an optical microscope in transmission mode with objective 50x, NA = 0.95 against a reference sample without laser treatment. Note that in case of strong scattering due to the micro-structure, 100% transmission cannot be reached.

Transmission [%]	As prepared	72 h at 500 °C	144 h at 500 °C
10 pulses	87	98	100
50 pulses	64	85	88
200 pulses	6	39	36

2.2 Photoluminescence enhancement of silicon nanocrystals by excimer laser implanted gold nanoparticles

This manuscript was published by the authors Lukas Janos Richter and Jürgen Ihlemann under the title "*Photoluminescence enhancement of silicon nanocrystals by excimer laser implanted gold nanoparticles*" in the journal *Applied Physics A* (Volume 128) by the publisher *Springer Nature* in August 2022. It is available on the website https://link.springer.com/article/10.1007/s00339-022-05906-1 or under the digital object identifier (DOI) *10.1007/s00339-022-05906-1*. The article is licensed by Springer Nature.

Enhancement of photoluminescence of silicon nanocrystals by implantation of gold nanoparticles into silicon suboxide is demonstrated. In this process, gold nanoparticles are introduced into silicon suboxide by UV-excimer-laser irradiation of a thin gold layer. Silicon nanocrystals are generated in the silicon suboxide by thermally induced phase separation. Coupling to gold nanoparticles significantly increases the photoluminescence of the silicon nanocrystals without the need for laborious lithographic processes. SEM-measurements, Raman-measurements, transmission measurements, AFM measurements and photoluminescence measurements are presented to investigate this effect and the causes.

The share of the authors work in the preparation of the manuscript is as follows: The planning of the experiments was done by Lukas Janos Richter (LJR) and Jürgen Ihlemann (JI). LJR carried out the experiments and performed the processing of the data and the preparation of the figures. LJR and JI discussed the measurement results. LJR wrote the original draft. Revision and correction of the final manuscript was done by LJR and JI.

The authors have no competing interests to declare that are relevant to the content of this article.

Applied Physics A (2022) 128: 764
https://doi.org/10.1007/s00339-022-05906-1

Applied Physics A
Materials Science & Processing

S.I. : COLA 2021/2022

Photoluminescence enhancement of silicon nanocrystals by excimer laser implanted gold nanoparticles

Lukas Janos Richter[1] · Jürgen Ihlemann[1]

Received: 2 June 2022 / Accepted: 28 July 2022 / Published online: 10 August 2022
© The Author(s), under exclusive licence to Springer-Verlag GmbH, DE part of Springer Nature 2022

Abstract
To enhance the photoluminescence of silicon nanocrystals, gold nanoparticles are incorporated into a silicon oxide matrix by excimer laser-based implantation. By this simple method, the gold nanoparticles are placed under the surface in a scratch resistant manner. Optical absorption measurements and SEM analyses show the essential properties of the gold implantation. The silicon nanocrystals are characterized by Raman and photoluminescence measurements. A more than twofold enhancement of the photoluminescence of the silicon nanocrystals, depending on the number of applied laser pulses during gold implantation, is achieved.

Keywords Si-Nanocrystal · Gold · Silicon · Excimer laser · Plasmonic nanoparticles · Photoluminescence

1 Introduction

Silicon in crystalline form is the standard material for our microelectronics today. The availability of all-silicon photonics would be desirable for the unification of microelectronics and photonics. However, due to the indirect band gap, efficient silicon light emitters are not yet available [1, 2]. Size reduction of silicon crystals could offer a solution to this problem. It enables effective photoluminescence (PL) of silicon at room temperature [3–5]. Therefore, a great amount of research has been done in this area since the discovery of the strong PL of nano-sized silicon [3–10].

Various methods for the production of silicon nanocrystals (Si-Nc, Si quantum dots) have been developed. Implantation of silicon ions into various materials has been demonstrated as a fabrication method [1, 11–13]. By varying the parameters of a plasma-enhanced chemical vapor deposition process, properties, such as the size, of the Si-Nc can be selectively achieved [1, 14–16]. Si-Nc can be formed by evaporation of silicon rich silicon oxide layers and subsequent thermal driven phase separation [1, 5, 17] or locally resolved by laser irradiation [18]. The size of the Si-Nc can be selectively adjusted, for example, by means of a multilayer system [1, 5]. Other generation methods use, for example, magnetron cosputtering [1, 19] or laser-induced decomposition of gas precursors [1, 20].

The occurrence of PL in Si-Nc cannot be attributed to a single effect. The band structure of silicon changes dramatically on small size scales (~5 nm), creating a quasi-direct band gap. Furthermore, defect centers contribute to PL [1, 21–23].

To make the PL of Si-Nc useful in practical applications, an increase in efficiency is needed [1]. Metal nanoparticles can increase PL of quantum dots through various effects. One effect most often mentioned in the literature is the change of the optical density of states in the quantum dots due to the presence of metal nanoparticles. Metal nanoparticles can concentrate strong electric fields in their environment, creating an enhanced local field. Quantum dots in this enhanced local field have a different optical density of states. This altered optical density of states affects the spontaneous emission rate, which is directly related to the PL intensity [1, 11, 17, 24, 25]. Another effect that can enhance the PL is the interaction of the metal nanoparticles with the incident light. This can lead to an enhanced interaction of the quantum dots with the excitation light and thus to an increased PL [1, 24]. Furthermore, the presence of metal nanoparticles offers the possibility that non-radiative emission energy from the quantum dots can be coupled out in the radiation field by energy transfer to surface plasmons at metal nanoparticle interfaces [1, 11, 24].

✉ Lukas Janos Richter
Lukas.richter@ifnano.de

[1] Institut für Nanophotonik Göttingen e.V., Hans-Adolf-Krebs-Weg 1, 37077 Göttingen, Germany

For Si-Nc this has already been demonstrated using a wide variety of methods. Silver particles fabricated by electron beam lithography cause PL enhancement of silicon quantum dots [26]. Authors of the same group have also shown the enhancement of PL on Si-Nc using nanoporous gold in dependence of a spacer layer [11]. Gold nanodiscs fabricated by electron beam lithography can increase the PL of Si-Nc by a factor of 5 [17]. In addition to these methods, many other approaches have been studied.

A new approach for PL enhancement is presented here: Gold nanoparticles (Au-Np) are easily and stably introduced into SiO_x (x ≈ 1) containing Si-Nc by excimer laser-based implantation of gold. Such laser implantation in SiO_x and commercial glasses has been previously investigated and used for other purposes, such as glass labeling [27, 28].

2 Methods

The Si-Nc were prepared by thermally induced phase separation of SiO_x. For this purpose, polished fused silica substrates were coated with silicon monoxide by vapor deposition. Thermal evaporation of SiO pellets with a size of 3–6 mm at a purity of 99.99% was performed through a baffled box in a commercially available Univex 350 chamber. The evaporation rate was fixed at 1 nm/s at a pressure of typically $3 * 10^{-6}$ mbar. For better layer adhesion, the substrates were heated to 300 °C during the entire process and surface sputtered for 30 s using argon ions before the evaporation process. We denote these coatings with the indeterminate oxidation state SiO_x, since a slight change of the oxygen content takes place during the coating process. The exact value of the "x" is therefore indeterminate, but close to $x = 1$. The layer thickness and transmission data were measured using a Filmetrics F20-UV optical layer thickness measurement device with a LS-DT2 light source.

The high temperature heating step required for the formation of Si-Nc was carried out by a Nabertherm R 50/250/13 furnace with a quartz tube controlled by a P330 controller. The quartz tube was continuously flushed with a nitrogen flow of 70 l/h, which corresponds to a purging factor of approximately 1.5/min. The samples were hydrogen passivated after thermal phase separation. A temperature of 540 °C was maintained for 2 h at a gas flow of 70 l/h. A forming gas (95% N_2/ 5% H_2) was used. During the heating ramps, purging was performed with 70 l/h N_2. This process can reduce dangling bonds and increase the radiative recombination rate and thus the PL of the Si-Nc [21, 29].

The analysis of the samples was carried out by scanning electron microscopy (SEM; Zeiss EVO MA10) and atomic force microscopy (AFM; Park Systems, XE-150). Material analysis was performed by Raman microscopy (Raman Horiba Xplora Plus, $\lambda = 532$ nm). The PL excitation was performed by a continuous-wave diode laser (Coherent OBIS 405 nm LX 100mW) on a homogeneously irradiated spot of about 150 µm diameter with a typical power of 0.77 mW on the sample surface. The PL light was measured in reflection, as it is shown in (Fig. 1). A dichroic mirror and a longpass filter suppress the excitation light. The detection was executed by two customized fiber coupled grating spectrometers (Ocean Optics HDX and NirQuest + 1.7). The spectrometers were calibrated using a calibration lamp (HL-2000-LL Ocean Optics) with a fiber output placed in the sample position. By this calibration method, all the components used in the PL-setup were included in the calibration. The measurement data of the two different spectrometers were multiplied by a numeric factor to ensure a smooth transition of the curves. The power of the excitation light was measured by a photo diode (Ophir PD300-3 W-V1).

Gold coatings were prepared by a sputter chamber (Emitech K550). These gold-layers were implanted into the silicon suboxide by excimer laser irradiation using an ArF-excimer ($\lambda = 193$ nm; $f = 10$ Hz; LPX-Pro, Coherent) with a pulse length of typically 20 ns. A mask projection with a demagnification of 5.4:1 was used for the irradiation. A homogenous part of the laser beam was chosen using a chrome mask with a transparent aperture of 3×3 mm^2. Spots of about 550×550 μm^2 are irradiated. For fluence variation,

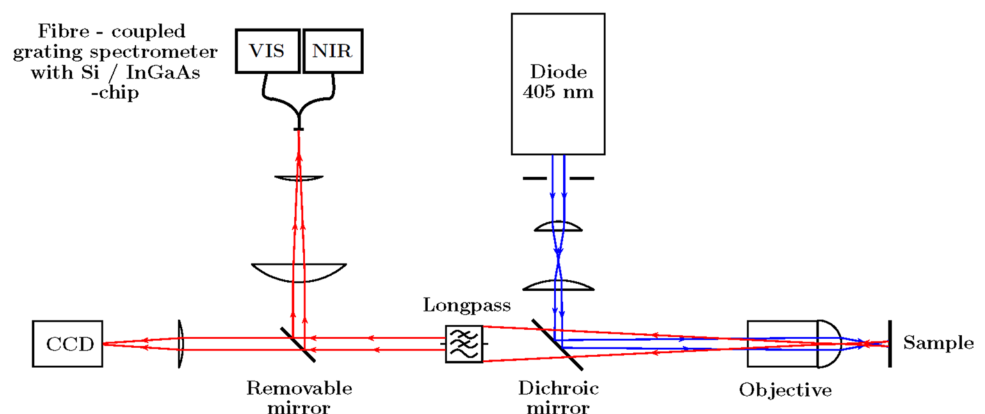

Fig. 1 Setup for PL measurement. The PL light is excited by a diode laser at $\lambda = 405$ nm. Through a dichroic mirror the excitation light is projected by an objective on the sample. The luminescence light is measured by two fibre coupled grating spectrometers in reflection. The dichroic mirror and the longpass filter suppress the excitation light. A CCD-camera is used for specimen positioning

a variable attenuator was added into the beam path. The setup is schematically sketched in (Fig. 2). A pyroelectric sensor (Ophir PE25BF-C) was used for energy measurements. After irradiation, the gold remaining on the surface was wiped away using a paper towel and ethanol. The entire sample preparation process is shown in (Fig. 3). In a first step, a quartz substrate is coated with SiO_x. A thin gold layer is deposited on this coating, which is then implanted by the laser. During this process, the gold layer and the top layer of silicon suboxide heat up, which leads to an incorporation of gold into the SiO_x. After cleaning the surface from non-implanted gold, the sample is thermally treated. This leads to the formation of Si-Nc and Au-Np.

3 Experimental results

Figure 4 shows Raman measurements of 750 nm SiO_x layers after the heating and passivation process. The measurements were corrected for the substrate background signal. The samples were heated to different temperatures to induce the phase separation, each indicated in the plot. It can be clearly seen that a peak at around 516 cm^{-1} is formed for temperatures of 976 °C and higher. This peak can be assigned to crystalline silicon and is in good agreement with literature

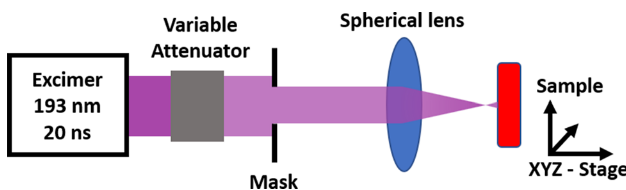

Fig. 2 The laser irradiation setup is based on an ArF-Excimer laser with a wavelength of 193 nm. The pulse length is typically 20 ns and the frequency is 10 Hz. For imaging, a chrome mask with a $3 \times 3\ mm^2$ transparent area and a spherical lens with a 5.4:1 demagnification are used. The applied energy is varied by a variable attenuator between the laser and the mask. The sample is mounted on an XYZ-stage

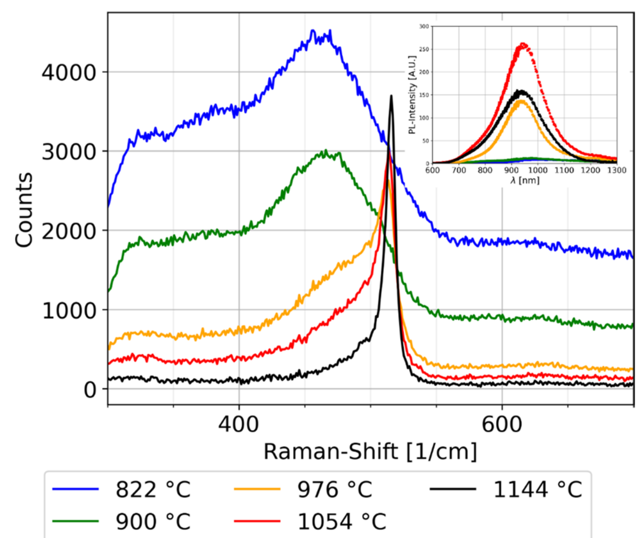

Fig. 4 Raman measurements on 750 nm SiO_x layers heated to different temperatures for one hour in nitrogen atmosphere. The inset shows the corresponding PL measurements. The Raman measurements are corrected for the SiO_2 substrate background signal

[1, 30]. With increasing temperature, the peak shifts slightly to larger Raman shifts (512.7 cm^{-1} for 976 °C; 513.7 cm^{-1} for 1054 °C and 515.9 cm^{-1} for 1144 °C). On the one hand, this indicates larger Si-Nc [1, 31]. This can also be seen in the corresponding PL measurement in the inset. For higher temperatures, a slight redshift in the PL spectrum can be measured. This can be explained by larger crystals [1, 32–34]. Furthermore, the shifted Raman shift can also be caused by stress in the sample [35, 36]. The literature shows that thermal phase separation in SiO_x leads to local strain effects in the layer and therefore an incomplete phase separation [37]. For temperatures of 900 °C and lower, no Raman peak for crystalline silicon is evident. Instead, a peak around 480 cm^{-1} is observed, which can be assigned to amorphous silicon [38]. Based on this temperature variation,

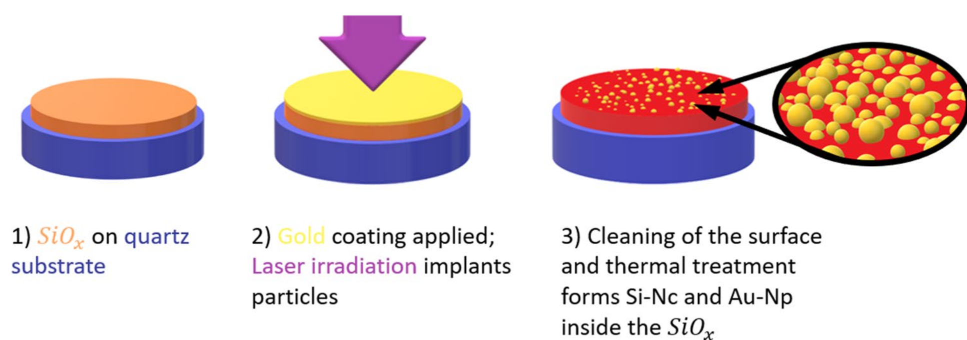

Fig. 3 Process scheme. (1) First, a quartz substrate was coated with SiO_x. (2) The sample is then coated with a thin gold layer and irradiated with an excimer laser. This leads to an implantation of gold into the SiO_x layer. (3) Subsequently, the surface is cleaned and a heating step induces the formation of Si-Nc and Au-Np, resulting in Au-Np implanted in the surface layer of Si-Nc consisting SiO_x

a temperature of 1050 °C was selected for further experiments, since the highest PL signal is measurable at this temperature.

During the oven processes, a thin SiO_2 layer is formed on the specimen due to an imperfect nitrogen atmosphere. The thickness depends on the selected oven temperature and the duration of the oven process. For the temperature of about 1050 °C used later, a SiO_2 layer thickness of about 25 nm is formed after one hour. There are no Si-Nc in this layer because all the silicon is oxidized.

The result of the gold implantation is visible in plasmonically active nanoparticles, which are introduced into the silicon suboxide. This can be detected by means of an absorption measurement, as can be seen in (Fig. 5). Here, gold from a 20 nm thick layer was introduced with different pulse numbers into a 100 nm SiO_x layer using excimer laser irradiation at 200 $\frac{mJ}{cm^2}$. A comparatively thin SiO_x layer was used here, so that absorption by the SiO_x and thin film interference effects that could disturb the measurement of the plasmon resonance are minimized. The choice of fluence was made after experimental optimization with respect to the PL enhancement in the range of 100 $\frac{mJ}{cm^2}$ to 400 $\frac{mJ}{cm^2}$ with 50 $\frac{mJ}{cm^2}$ increments. The data were calculated from the transmission data using $A = -1 * log_{10}(T)$. The measurement was corrected for the SiO_2 substrate as background. A peak around 530 nm is present, which is characteristic for spherical Au-Np. It is visible that the height of the peak differs for different pulse numbers. For one applied laser pulse, the highest absorption contrast from the plasmon resonance to the background is measured. After 10 laser pulses, the total absorption increased. This can be explained by an increased number of implanted particles and an increased surface roughness. For higher pulse numbers, the total absorption drops sharply, since a large part of the SiO_x layer together with the implanted nanoparticles was removed by the increased number of laser pulses.

The Au-Np are also clearly visible in SEM images. Figure 6 shows four SEM images of the SiO_x layer with implanted Au-Np, the used pulse number is indicated individually. The process parameters were a fluence of 200 $\frac{mJ}{cm^2}$ and a temperature of 1054 °C for 1 h for the heating process. The images were taken at an angle of 60° to the surface to demonstrate the depth of implantation of the particles. In the SEM image for 1 pulse, bright spheres can be identified as Au-Np. It can be seen that the size of the Au-Np varies. In addition, the Au-Np are implanted to different depths. Some of the particles are only very slightly embedded in the material, others disappear almost completely in the SiO_x. This suggests that some Au-Np are not visible at all because they have been completely incorporated into the material. Pits are also visible in the SiO_x, from which the Au-Np have been wiped out by cleaning the surface. Therefore, some of the gold particles sit only loosely in the material. After 10 pulses the density of the Au-Np has increased significantly. It can also be seen that the Au-Np are embedded deeper in the SiO_x. The increased number of pulses therefore also leads to deeper implantation. Also, the roughness of the surface increased significantly. This can be seen after 100 and 1000 laser pulses. It is confirmed by AFM measurements. For 1; 10; 100 and 1000 pulses roughness values of R_q = 27;55;102 and 187 nm are measured respectively.

The Si-Nc show significant PL. This can be seen in (Fig. 5). The black data shows the PL of a 507 nm thick SiO_x layer after a heating process of 1054 °C for 1 h and subsequent passivation. A broad PL peak around 950 nm can be seen, indicating a range of different crystals sizes.

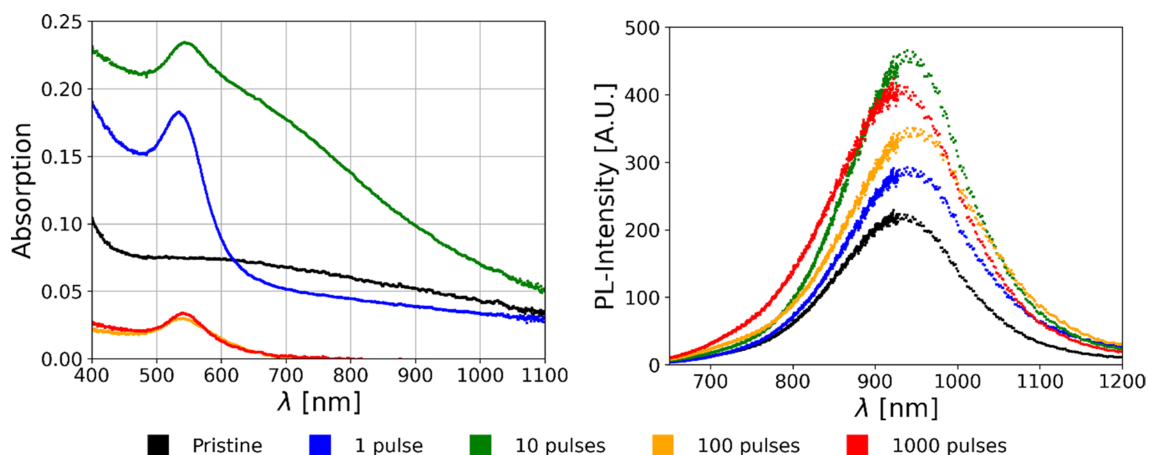

Fig. 5 Absorption (left side) and PL (right side) measurements of SiO_x layers with implanted Au-Np after the thermal treatment. The applied laser pulse number is indicated in the label. The absorption measurements were corrected for the SiO_2 substrate. The layer thickness is 100 nm for the absorption measurements and 507 nm for the PL measurements. The process parameters are: λ = 193 nm, 200 $\frac{mJ}{cm^2}$, 20 nm Au layer, 1054 °C for 1 h in nitrogen atmosphere

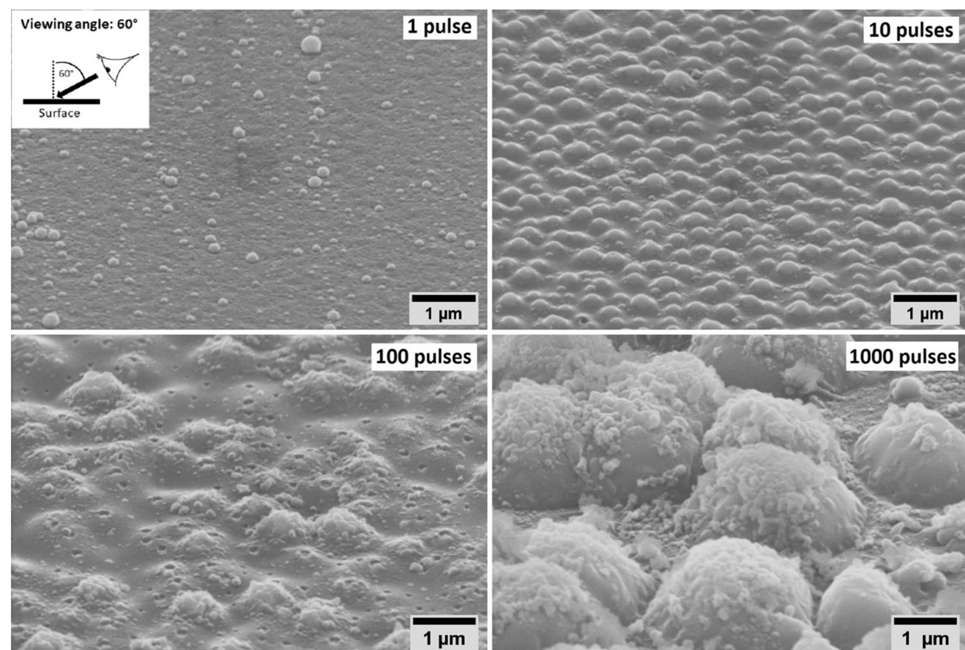

Fig. 6 SEM images of the SiO_x surface with implanted Au-Np after the heating treatment (1054 °C for 1 h). The images are taken at an angle of 60° to the surface normal, as schematically indicated. The laser parameters are: $\lambda = 193$ nm, 200 $\frac{mJ}{cm^2}$, 20 nm Au layer, the pulse number is indicated individually

Due to the introduced Au-Np, a clear enhancement of the PL is visible. The corresponding measurement curves can be recognized by the colored measurement data. Already after the application of one laser pulse for gold implantation, an enhancement of the PL by a factor of 1.3 can be seen. An enhancement by a factor of 2.1 results for 10 pulses. With a further increase in the number of pulses, however, the PL intensity decreases again, as can be seen after 100 and 1000 pulses. Based on the PL measurements, a red shift of the PL with increasing pulse number by the implanted Au-Np can also be observed. This may be caused by a stronger enhancement of the PL in the near-infrared region.

Several aspects were investigated to rule out the possibility of the measurements being disturbed by other effects. No PL was detectable when gold was implanted into the pure substrate material without Si-Nc containing SiO_x coating. The SiO_x surface was also irradiated with an excimer laser without a gold coating for testing purposes. No increase in PL was detected by this process. Also, no PL was measurable with implanted gold particles in SiO_x without the heating processes.

4 Discussion

The absorption measurements prove the formation of plasmonically active Au-Np. On the basis of the SEM measurements, implantation into the silicon suboxide coating can be demonstrated. The gold particles have been scratch-resistantly incorporated into the silicon suboxide layer. The increased density of Au-Np at increased laser pulse number can be explained by a larger amount of gold material introduced into the SiO_x layer during implantation. Therefore, less non-implanted gold is wiped away from the sample surface during cleaning.

The enhancement of PL by the gold particles may be due to several causes. As reported in the literature, the optical density of states of a matrix is changed by the presence of metal-nanoparticles [39, 40]. Since the emission rate of Si-Nc is proportional to the local density of states, the presence of Au-Np alters the emission rate. [11, 17]. A shorter decay time of the excited states in the Si-Nc increases the optical recombination rate, which is apparent from an increased PL.

Furthermore, the presence of a wide range of gold nanoparticle shapes and sizes, which results also in high surface roughness due to the implantation process, will favor coupling of silicon nanocrystal emission energy into the radiative field by a surface plasmon at the Au-Np–SiO_2 interface [11].

As another effect, the Au-Np can increase the interaction of the Si-Nc with the excitation laser, which also increases the PL. Since there is little overlap of the plasmon resonance with the wavelength of the excitation laser, this effect is likely to be small.

Last, it should be noted that the enhancement of PL by metal nanoparticles depends on the distance of the metal particles from the nanocrystals. This has been demonstrated theoretically and experimentally [11, 17, 25, 26, 41–43]. Since a broad distribution of distances between the Au-Np and the Si-Nc is expected in this case, amplification and quenching effects average out to some extent, resulting in

the measurable enhancement. A specific adjustment of the SiO_2 layer thickness at the surface could further enhance the PL enhancement.

The different strengths in the PL enhancement can be explained on the one hand by an increased density of gold particles. It is evident from the SEM images that after 10 pulses significantly more gold was introduced into the material. According to the SEM images, the depth of gold implantation also increased from 1 to 10 laser pulses. The Au-Np are thus implanted closer to the Si-Nc, as the oxide layer that forms during the heating process could otherwise form a too large spacer layer. This could explain the difference between the PL enhancement between 1 and 10 laser pulses. There are several reasons for the PL-signal drop after 100 and 1000 laser pulses. Firstly, at such a high number of laser pulses, a significant part of the material is removed. This is due to the fluence required for gold implantation. The used fluence of 200 $\frac{mJ}{cm^2}$ is above the multipulse ablation threshold for SiO_x at this wavelength, according to literature [44]. This can also be seen in the absorption measurements in (Fig. 5). Thus, the overall number of Si-Nc decreases and the PL signal is weakened. The second reason could be found in a size increase of the Au-Np with increasing pulse number. The increase in size can be observed to some extent in the SEM images. However, this is also known in the literature [28]. The plasmon resonance of the gold particles depends on their size. For big particles (size comparable to wavelength of the incident light) multipole absorption takes place [45]. This could lead to a weaker enhancement of the PL. A third cause may be the increasing silicon dioxide layer thickness, which can be further formed by many laser pulses. It is described in the literature that irradiation with many excimer laser pulses in air leads to oxidation of the silicon suboxide layer [46]. A thicker silicon dioxide layer, which does not contain Si-Nc, thus increases the distance between Si-Nc and Au-Np and can therefore lead to weaker amplification by the gold particles.

5 Conclusion

The enhancement of PL of Si-Nc by Au-Np was demonstrated. The Au-Np were introduced into a silicon suboxide layer by a fast and simple method based on excimer laser irradiation. In contrast to other methods, no complicated and costly electron lithography is required. Furthermore, the gold particles are embedded in the material in a scratch-resistant manner. Continued refinement of the parameters could further increase the PL enhancement. Further studies, such as transmission electron microscopy, could help to explain the processes involved in gold implantation and the resulting PL amplification.

Funding We acknowledge the financial support of the Deutsche Forschungsgemeinschaft, project IH 17/27-1.

Declarations

Conflict of interest The authors have no competing interests to declare that are relevant to the content of this article.

References

1. L. Pavesi, R. Turan, Silicon Nanocrystals Fundamentals, Synthesis and Applications, 1st edn. (Wiley-VCH, Weinheim, 2010), pp. 1–447
2. A.D. Yoffe, Adv. Phys. **42**, 173 (1993). https://doi.org/10.1080/00018739300101484
3. L.T. Canham, Appl. Phys. Lett. **57**, 1046 (1990). https://doi.org/10.1063/1.103561
4. A.G. Cullis, L.T. Canham, Nature **353**, 335 (1991). https://doi.org/10.1038/353335a0
5. M. Zacharias, J. Heitmann, R. Scholz, U. Kahler, M. Schmidt, J. Bläsing, Appl. Phys. Lett. **80**, 661 (2002). https://doi.org/10.1063/1.1433906
6. S. Tiwari, F. Rana, H. Hanafi, A. Hartstein, E.F. Crabbé, K. Chan, Appl. Phys. Lett. **68**, 1377 (1996). https://doi.org/10.1063/1.116085
7. L. Pavesi, L.D. Negro, C. Mazzoleni, G. Franzò, F. Priolo, Nature **408**, 440 (2000). https://doi.org/10.1038/35044012
8. G. Ledoux, O. Guillois, D. Porterat, C. Reynaud, F. Huisken, B. Kohn, V. Paillard, Phys. Rev. B **62**, 15942 (2000). https://doi.org/10.1103/PhysRevB.62.15942
9. R.J. Walters, G.I. Bourianoff, H.A. Atwater, Nature. Mater. **4**, 143 (2005). https://doi.org/10.1038/nmat1307
10 D. Jurbergs, E. Rogojina, Appl. Phys. Lett. **88**, 233116 (2006). https://doi.org/10.1063/1.2210788
11 J.S. Biteen, D. Pacifici, N.S. Lewis, H.A. Atwater, Nano. Lett. **5**, 9 (2005). https://doi.org/10.1021/nl051207z
12 Y. Kanemitsu, N. Shimizu, T. Komoda, P.L.F. Hemment, B.J. Sealy, Phys. Rev. B. (1996). https://doi.org/10.1103/PhysRevB.54.R14329
13 T. Shimizu-Iwayama, K. Fujita, J. Appl. Phys **75**, 7779 (1994). https://doi.org/10.1063/1.357031
14 A.J. Kenyon, P.F. Trwoga, C.W. Pitt, J. Appl. Phys. **79**, 9291 (1996). https://doi.org/10.1063/1.362605
15 X.L. Wu, Appl. Phys. Lett. **69**, 523 (1996). https://doi.org/10.1063/1.117774
16. T.-W. Kim, C.-H. Cho, B.-H. Kim, S.-J. Park, Appl. Phys. Lett **88**, 123102 (2006). https://doi.org/10.1063/1.2187434
17 J. Goffard, D. Gérard, P. Miska, A.-L. Baudrion, R. Deturche, J. Plain, Sci. Rep **3**, 2672 (2013). https://doi.org/10.1038/srep02672
18 T. Fricke-Begemann, N. Wang, P. Peretzki, M. Seibt, J. Ihlemann, J. Appl. Phys. **118**, 124308 (2015). https://doi.org/10.1063/1.4931670
19 S. Charvet, R. Madelon, F. Gourbilleau, R. Rizk, J. Appl. Phys **85**, 4032 (1999). https://doi.org/10.1063/1.370307
20 S. Botti, R. Coppola, J. Appl. Phys. **88**, 3396 (2000). https://doi.org/10.1063/1.1288228
21 G. Ledoux, J. Gong, F. Huisken, Appl. Phys. Lett **79**, 4028 (2001). https://doi.org/10.1063/1.1426273
22 A.G. Cullis, J. Appl. Phys **82**, 909 (1997). https://doi.org/10.1063/1.366536
23 T. Schmidt, A.I. Chizhik, A.M. Chizhik, K. Potrick, A.J. Meixner, F. Huisken, Phys. Rev. B **86**, 125302 (2012). https://doi.org/10.1103/PhysRevB.86.125302

24 K.T. Shimizu, W.K. Woo, B.R. Fisher, H.J. Eisler, M.G. Bawendi, Phys. Rev. Lett. **89**, 117401 (2002). https://doi.org/10.1103/PhysRevLett.89.117401
25 O. Kulakovich, N. Strekal, A. Yaroshevich, S. Maskevich, S. Gaponenko, I. Nabiev, U. Woggon, M. Artemyev, Nano Lett. **2**, 1449 (2002). https://doi.org/10.1021/nl025819k
26 J.S. Biteen, N.S. Lewis, H.A. Atwater, Appl. Phys. Lett. **88**, 131109 (2006). https://doi.org/10.1063/1.2191411
27 H. Stolzenburg, P. Peretzki, N. Wang, M. Seibt, J. Ihlemann, Appl. Surf. Sci. **374**, 138 (2016). https://doi.org/10.1016/j.apsusc.2015.10.092
28 M. Heinz, V.V. Srabionyan, L.A. Avakyan, A.L. Bugaev, A.V. Skidanenko, V.V. Pryadchenko, J. Ihlemann, J. Meinertz, C. Patzig, M. Dubiel, L.A. Bugaev, J. Alloys Compd. **736**, 152 (2018). https://doi.org/10.1016/j.jallcom.2017.11.122
29 M. Lopez, B. Garrido, C. García, P. Pellegrino, A. Pérez-Rodríguez, J.R. Morante, C. Bonafos, M. Carrada, A. Claverie, Appl. Phys. Lett. **80**, 1637 (2002). https://doi.org/10.1063/1.1456970
30 J.H. Parker, D.W. Feldman, M. Ashkin, Phys. Rev. **155**, 3 (1967). https://doi.org/10.1103/PhysRev.155.712
31 J. Zi, H. Büscher, C. Falter, W. Ludwig, K. Zhang, X. Xie, Appl. Phys. Lett. **69**, 2 (1996). https://doi.org/10.1063/1.117371
32 Y. Kanzawa, T. Kageyama, S. Takeoka, M. Fujii, S. Hayashi, K. Yamamoto, Sol. St. Com. **102**, 7 (1997). https://doi.org/10.1016/S0038-1098(96)00774-0
33 S. Takeoka, M. Fujii, S. Hayashi, Phys. Rev. B **62**, 24 (2000). https://doi.org/10.1103/PhysRevB.62.16820
34. Y. Yu, G. Fan, A. Fermi, R. Mazzaro, V. Morandi, P. Ceroni, D.-M. Smilgies, B.A. Korgel, J. Phys. Chem. C **121**, 23240 (2017). https://doi.org/10.1021/acs.jpcc.7b08054
35. I.D. Wolf, J. Raman Spectrosc. **30**, 877 (1999)
36 L. Khriachtchev, M. Räsänen, S. Novikov, Appl. Phys. Lett. **88**, 013102 (2006). https://doi.org/10.1063/1.2161399
37 A. La Magna, G. Nicotra, C. Bongiorno, C. Spinella, M.G. Grimaldi, E. Rimini, L. Caristia, S. Coffa, Appl. Phys. Lett. **90**, 183101 (2007). https://doi.org/10.1063/1.2734398
38 A.T. Voutsas, M.K. Hatalis, J. Boyce, A. Chiang, J. Appl. Phys. **78**, 6999 (1995). https://doi.org/10.1063/1.360468
39 E.M. Purcell, NSSB. (1946). https://doi.org/10.1007/978-1-4615-1963-8_40
40 J. Gersten, A.J. Nitzan, Chem. Phys. **75**, 1139 (1981). https://doi.org/10.1063/1.442161
41 A.L. Muñoz-Rosas, A. Rodríguez-Gómez, J.A. Arenas-Alatorre, J.C. Alonso-Huitrón, RSC Advances **5**, 92923 (2015). https://doi.org/10.1039/C5RA19114A
42 A.L. Tchebotareva, M.J.A. de Dood, J.S. Biteen, H.A. Atwater, A. Polman, J. Lumin. **114**, 137–144 (2005). https://doi.org/10.1016/j.jlumin.2004.12.014
43 J.S. Biteen, L.A. Sweatlock, H. Mertens, N.S. Lewis, A. Polman, H.A. Atwater, J. Phys. Chem. C **111**, 13372–13377 (2007). https://doi.org/10.1021/jp074160+
44 J. Ihlemann, J. Meinertz, G. Danev, Appl. Phys. Lett. **101**, 091901 (2012). https://doi.org/10.1063/1.4748127
45. U. Kreibig, M. Vollmer, Optical Properties of Metal Clusters, 1st edn. (Springer-Verlag Berlin Heidelberg New York, 1995), pp. 42–53
46 J. Richter, J. Meinertz, J. Ihlemann, Appl. Phys. A **104**, 759 (2011). https://doi.org/10.1007/s00339-011-6451-8

Publisher's Note Springer Nature remains neutral with regard to jurisdictional claims in published maps and institutional affiliations.

Springer Nature or its licensor holds exclusive rights to this article under a publishing agreement with the author(s) or other rightsholder(s); author self-archiving of the accepted manuscript version of this article is solely governed by the terms of such publishing agreement and applicable law.

2.3 Excimer laser surface patterning for photoluminescence enhancement of silicon nanocrystals

This manuscript was submitted to the journal *Photonics* by the publisher *MDPI* under the title "*Excimer laser surface patterning for photoluminescence enhancement of silicon nanocrystals"* by the authors Lukas Janos Richter, Ulrich Ross, Michael Seibt and Jürgen Ihlemann. At the time of submission of the dissertation, the review process could not be completed. At the time of publication of the dissertation, the review process was successfully completed. In this dissertation, the version of the manuscript at the time of submission is presented. The final version of the manuscript is available from the journal *Photonics* (Volume 10) of the publisher MDPI on the website https://www.mdpi.com/2304-6732/10/4/358 or under the digital object identifier (DOI) *10.3390/photonics10040358*. The article is published as an open access publication.

An enhancement of the photoluminescence signal dependent on the excimer laser irradiation of the silicon suboxide is demonstrated. By surface analysis (AFM and SEM) and structural analysis (Raman and TEM) we identify two causes for the photoluminescence enhancement. One minor part can be attributed to a different nucleation process of silicon nanocrystals during the thermally induced phase separation of silicon suboxide. A larger part can be attributed to an optical effect, caused by periodic patterning of the surface. The enhancement results from reduced losses due to total internal reflection in the highly refractive silicon suboxide layer.

The share of the authors work in the preparation of the manuscript is as follows: The planning of the experiments was done by Lukas Janos Richter (LJR) and Jürgen Ihlemann (JI). LJR carried out the coating processes and the laser experiments. LJR carried out the photoluminescence, AFM, SEM, Raman and optical layer thickness measurements and performed the processing of the respective data and the preparation of the figures. Ulrich Ross (UR) carried out the TEM preparation and TEM analysis and performed the processing of the respective data. LJR, UR, Michael Seibt (MS) and JI discussed the measurement results. LJR wrote the original draft. Revision and correction of the final manuscript was done by LJR, UR, MS and JI.

The authors have no competing interests to declare that are relevant to the content of this article.

photonics MDPI

Article 1

Excimer laser surface patterning for photoluminescence en- 2
hancement of silicon nanocrystals 3

Lukas Janos Richter [1,]*, Ulrich Ross [2], Michael Seibt [2] and Jürgen Ihlemann[1] 4

[1] Institut für Nanophotonik Göttingen e.V.; Hans-Adolf-Krebs-Weg 1, 37077 Göttingen, Germany 5
[2] University of Göttingen, IV. Physical Institute; Friedrich-Hund-Platz 1, 37077 Göttingen, Germany 6
* Correspondence: Lukas.richter@ifnano.de 7

Abstract: A method for enhancing the photoluminescence of silicon nanocrystals in a silicon oxide 8
matrix by fabrication of periodic surface structures through laser irradiation is demonstrated. ArF- 9
excimer lasers are used to produce periodic line structures by material ablation. Photoluminescence, 10
Raman and transmission electron microscope measurements consistently show the formation of 11
crystalline silicon after high-temperature annealing. A 2.6-fold enhancement of photoluminescence 12
signal is measured for a periodic line structure with 600 nm period. The influence of a surface struc- 13
ture on the photoluminescence from the silicon oxide layer is discussed in terms of a simple model 14
describing the main effect. 15

Keywords: Si-Nanocrystal, Silicon, Excimer laser, Photoluminescence, TEM 16
17

1. Introduction 18

The development of a pure silicon-based light emitting device would not only elimi- 19
nate the need for more expensive and toxic III-V compound semiconductors, but would 20
also enable the integration of photonics into silicon-based microelectronics. Therefore, the 21
research on efficient light emission from silicon has become an important subject in the last 22
years [1] [2] [3] [4] [5] [6] [7] [8] [9], which is a challenging task due to the indirect band 23
gap of bulk silicon. Modifying the band structure of silicon can increase the efficiency of 24
light emission as exemplified by silicon nanocrystals (Si-Nc) exhibiting a much higher light 25
emission efficiency compared to bulk silicon [2] [3] [4]. Although details of processes un- 26
derlying the Si-Nc photoluminescence are still under debate, it can be attributed, at least 27
in part, to the quasi-direct band gap of Si-Nc due to confinement effects at a size of or 28
below about 5 nm [2] [10] [11] [12] [13]. Details to be considered involve the effect of the 29
Si-Nc surrounding matrix and size-related strain effects [14] [15] as well as interaction be- 30
tween densely packed Si-Nc [16]. Finally, defect centers at the crystal surface also have a 31
crucial impact on the efficiency of photoluminescence [10] [13] [14] [17] [18]. 32

The increase in efficiency, however, is still too small for practical applications. Hence, 33
there have been different approaches to enhance the light emission efficiency of silicon 34
nanocrystals. Many approaches aim at the reduction of non-radiative recombination chan- 35
nels and a number of strategies are possible depending on the particular non-radiative 36
channel under consideration. 37

First of all, the production method of the nanocrystalline silicon plays a major role. 38
The chosen method not only determines the size of the crystals, which affects the optical 39
band gap, but also the configuration of the surrounding matrix [19] [20]. Canham discov- 40
ered room temperature photoluminescence of nanoporous silicon produced by electro- 41
chemical dissolution of silicon wafers [2]. With the following growth in research interest 42
about nanocrystalline silicon, other methods evolved for their generation. A simple 43
method is a thermally driven phase separation of substoichiometric silica, e. g. SiO, into 44
SiO_2 and Si [19] [20] [21]. Further control on the size of silicon nanocrystals has been 45

achieved by thermal annealing of multilayer systems of alternating SiO_2 and SiO [13] [4]. Additionally, locally resolved nanocrystal production is possible by laser induced phase separation [22]. Other manufacturing methods include plasma-enhanced chemical vapor deposition [23] [24] [25], sputtering [1] [26] and implantation of silicon ions into a host matrix [27] [28] [29].

Further focus has been put on the interface between silicon nanocrystals and the surrounding matrix, which may strongly affect the efficiency of light emission. Defect states at the interface of the nanocrystals potentially add non-radiative recombination channels and therefore lower light emission efficiency. Hence, defect engineering of such states has been extensively studied proving hydrogen passivation, e. g. by heating in a hydrogen atmosphere [30], to be beneficial. Besides hydrogen passivation, also oxygen, nitrogen or carbon-based passivation has been reported [31]. A positive aspect common to these methods is their mostly negligible effect on the core of the nanocrystals [31]. Moreover, doping with other elements like phosphorus or boron can increase the efficiency of light emission [1] [31].

Finally, plasmonic nanoparticles, like gold nanoparticles, lead to efficiency enhancement of the nanocrystals´ light emission. Placing these nanoparticles in close proximity to the nanocrystals can lead to an efficiency increasing coupling effect [32] [33] [34].

A fundamentally different approach used in many light emitting devices aims at an improved coupling out of emitted light from a highly refractive layer, e. g. by the periodic structuring of surfaces. As an example, enhanced PL was measured on GaN nanostructures in this way [35]. These improvements in emission efficiency are due to a reduction in losses due to total internal reflection in highly refractive layers.

The influence of surface structures on the PL of Si-Nc containing samples has barely been studied so far or just in combination with other parameters. The correlation between PL and surface roughness was investigated. In this study, however, the roughness was varied by different growths temperatures during sample preparation. This not only changed the roughness, but also other properties, such as the oxygen content [36]. Periodic platinum arrays were also used to increase the PL. In this case, plasmonic effects also play a role [37]. The effect by surface structures on the PL of Si-Nc, without plasmonic or other influences, was studied by surface structuring in the form of a two-dimensional photonic crystal. In this study PL light propagating in a layer is Bragg-diffracted out of the samples, leading to an increase in light extraction efficiency in a small spectral range [38].

In this work, the enhancement of photoluminescence of silicon nanocrystals inside a substoichiometric silicon oxide matrix (SiO_x, $x \approx 1$) by surface structuring is presented. It is shown that modifying the surface topography by irradiation of SiO_x with commercially available argon-fluoride (ArF) excimer laser irradiation (λ = 193 nm) leads to a significant increase of the PL signal over the whole spectral range. Since laser irradiation potentially affects the Si-Nc [39] [40], the strategy of our experiments is, besides merely proving enhanced PL, to elucidate nanostructural changes by means of Raman spectroscopy and transmission electron microscopy. Following this concept, such changes can be ruled out as the source of enhanced PL emission. Hence, periodic surface structuring is identified as its underlying mechanism, which is substantiated by model calculations.

The paper is structured as follows. First, the methods for sample preparation, processing and analysis are presented. Subsequently, as the main observation, the enhanced PL emission is described and related to surface topography using scanning electron microscopy (SEM) and atomic force microscopy (AFM). Laser-induced structural modifications are described in Sec. 3.3 and 3.4. Finally, results are summarized and discussed in the light of model calculations.

2. Materials and Methods

2.1. Sample preparation

The preparation of the samples is identical to the methods described in a previous work [32]. In summary, SiO_x coatings were prepared by thermal evaporation of SiO on polished fused silica substrates. During a heating step in nitrogen atmosphere at 1050 °C for one hour, silicon nanocrystals (Si-Nc) were prepared by thermally induced partial phase separation. An inert nitrogen atmosphere was ensured by nitrogen flow with 99.999 % N_2. The volume of the furnace is purged approximately 1.5 times per minute. A subsequent hydrogen passivation at 540 °C for two hours was performed to reduce surface-interface non-radiative recombination at defect states at the crystals surface. For this process, a forming gas with 5 % H_2 and 95 % N_2 was used at the same flow rate. Nitrogen purging was performed during the heating ramps. Heating was conducted in a quartz tube with a Nabertherm R50/250/13 furnace.

2.2 Laser irradiation

Laser irradiation was performed with pulsed ArF-excimer lasers (λ = 193 nm) with a pulse length of typically 20 ns. Three setups were used. One for areal irradiation with a homogeneous fluence profile and two setups for structured irradiation with an inhomogeneous fluence profile to generate line gratings with different periods. The parameters for all three laser treatments are shown in table 1. A more detailed description of the setup for homogeneous irradiation is also described in [32]. The processes for structured laser irradiation are similar, except for the imaging lens and the mask, and are schematically sketched in Figure 1. A homogeneous part of the laser beam traverses a rectangular chrome mask and fused silica phase mask (refractive index n = 1.56) with a binary height profile in form of a line grating of certain periodicity [41]. As the height "d" of lines is chosen for destructive interference at a wavelength of λ = 193 nm ($d = \lambda/(2*(n-1))$ = 173 nm), the beam mainly splits up into the +/- first orders. The first orders of the laser beam are then united on the sample surface by the imaging lens and produce a sinusoidal interference pattern of period "P". To suppress any superstructure, the zeroth order, the 2nd and higher orders are blocked in front of the imaging lens for the setups using a fused silica phase mask. In all three setups a variable attenuator in the beam path enables fluence variation. The energy deposited on the sample is measured with a pyroelectric sensor (Ophir, PE10BF-C). Subsequent to the laser irradiation, a cleaning step is performed to remove any debris from the sample surface. A KOH-based cleaning agent (Deconex 15PF-x) is mixed with deionized water at a ratio of 1:2. The samples were cleaned with this mixture for 10 minutes in an ultrasonic bath. To remove any residual detergent, the samples were then sonicated in deionized water for 10 minutes. Subsequently, the samples were dried by nitrogen flow without contact to avoid any contamination.

In order to precisely assign the samples to the respective treatments, a process diagram for all samples is shown in Figure 2. A letter is assigned to each individual sample as its name ("A" to "I"). In the following, a description of the processing procedure is given for each sample in addition to the process diagram. The thickness of the SiO_x coating is always 1050 nm. Sample "A" is as-coated. Sample "B" is hydrogen passivated after the coating process. Sample "C" is high-temperature annealed after the coating process. Sample "D" is high-temperature annealed after the coating process and subsequently hydrogen passivated. Sample "E" is laser-irradiated with a homogeneous fluence after the coating process and subsequently high-temperature annealed and hydrogen passivated. Sample "F" is laser-irradiated with the objective lens setup (line grating with P = 1000 nm) after the coating process and subsequently high-temperature annealed and hydrogen passivated. Sample "G" is laser-irradiated with the Schwarzschild-objective setup (line grating with P = 600 nm) after the coating process and subsequently high-temperature annealed. Sample "H" went through the same process as sample "G" with subsequent hydrogen passivation. Sample "I" was laser-irradiated with the Schwarzschild-objective setup (line grating with P = 600 nm) after the coating process.

154

155

Setup	Homogeneous irradiation	Grating irradiation P = 600 nm	Grating irradiation P = 1000 nm
Laser system	LPX-Pro, Coherent	Novatex, Coherent	LPX-Pro, Coherent
Demagnification	5.4:1	25:1	10:1
Mask aperture	3 x 3 mm^2	2 x 2 mm^2	1 x 1 mm^2
Phase mask period	Not used	30 µm	20 µm
Imaging lens	Spherical lens f = 100 mm	Schwarzschild-Objective; NA = 0.4	Imaging-Objective (Thorlabs LMU-10x-193); NA = 0.27
Resulting spot size	550 x 550 µm^2	78 x 78 µm^2	102 x 102 µm^2
Treated samples	E	G, H, I	F

Table 1. Crucial parameters of the three different laser setups used for sample irradiation. 156

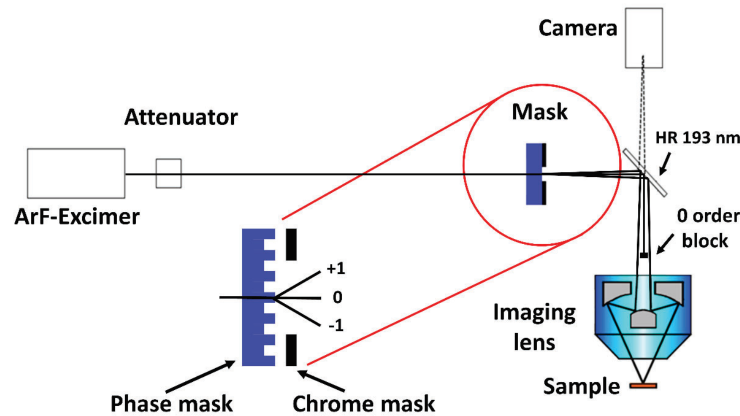

157

Figure 1. Optical setup to produce a line grating by ArF-excimer laser irradiation of the samples. An attenuator offers fluence adjustment. A binary fused silica phase mask in contact with a transparent chromium mask is used. The structure of the mask, as well as the first diffraction orders, are shown enlarged, indicated by the red marking. A lens is used to recombine the first orders of the split up beam on the sample surface (the Schwarzschild-objective is shown here as an example). The sizes are not to scale. Crucial details of the setups are shown in table 1. 158 159 160 161 162 163

164

165

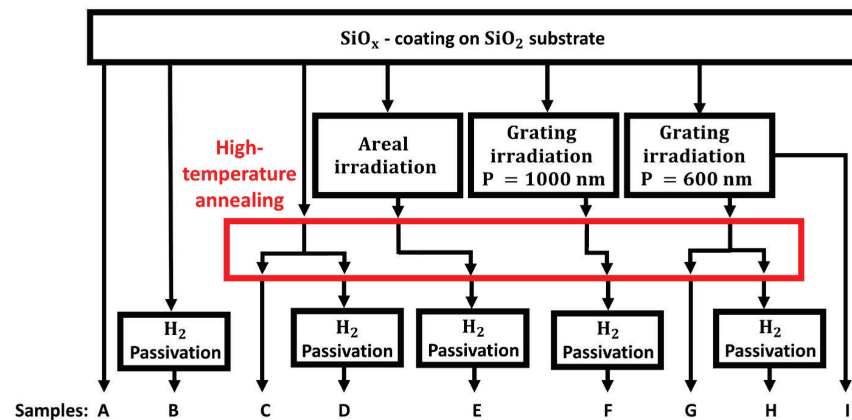

Figure 2. Process diagram for the production of the samples. All samples are SiO_x coated on a SiO_2 substrate and subsequently experience either no or different laser irradiation and thermal treatment processes. The letter on the bottom denotes the designation of the individual samples.

2.3 Sample analysis

The photoluminescence (PL) of the samples was analyzed with two customized fiber coupled grating spectrometers (Ocean Optics HDX and NirQuest+ 1.7) at room temperature. The photoluminescence setup was calibrated using a fiber-coupled calibration lamp (HL-2000-LL, Ocean Optics) in the sample position to include all optical components in the calibration. A smooth transition of the data of the two spectrometers was ensured by multiplying the data of the NIR-spectrometer by a numeric factor. Excitation of the samples was performed with a continuous laser diode (λ = 405nm, Coherent OBIS 405 nm LX 100mW) on a homogeneous irradiated spot size of 220 µm diameter with a power of 0.85 mW resulting in a power density of approximately 2240 mW/cm^2. The photoluminescence light was measured in reflection while the excitation light was blocked by a dichroic mirror and a longpass filter. The numerical aperture of the lens was 0.6. A more detailed description of the PL-setup can be found in our previous work [32]. Even though the intensity units are given in arbitrary units, the intensity scale is comparable between individual measurements.

The formation of silicon nanocrystals was analyzed by transmission electron microscopy (TEM) using a 300 kV FEI Titan G2 ETEM equipped with an image Cs-corrector (CEOS CETCOR) and Gatan Imaging Filter (GIF). Samples were prepared by focused ion beam thinning (FEI Helios FIB) of cross-section lamellas, and thus coated with polycrystalline Pt in order to protect the surface during milling. High-resolution phase-contrast imaging (information limit $d_{info} \approx 0.1$ nm) reveals the local crystallinity of selected sample regions. Annular dark-field scanning transmission electron microscopy (STEM, 10 mrad beam convergence) reveals mass-thickness and diffraction contrast features across the entire layer thickness. The chemical composition of the samples, in particular the Si:O ratio, was measured to within +/- 3 % from energy-dispersive X-ray spectroscopy (EDX) measurements in scanning mode, using the SiO_2 substrate as an internal reference [42]. In addition, STEM energy loss spectroscopy data was recorded from the low-loss region of the spectra (0-100 eV). In this region, plasmon excitations generate strong peaks around 17 eV and 23 eV which can be correlated with silicon-rich clusters and SiO_x, respectively [43]. These peaks were fitted by Lorentzians of fixed position and variable width/height in order to enhance the contrast of the nanocrystalline Si-rich clusters. A surface analysis of the samples was performed by scanning electron microscopy (SEM; Zeiss EVO MA10). Material analysis was performed by Raman microscopy (Raman Horiba Xplora Plus, λ = 532 nm). Surface topography of the samples was measured by atomic force microscopy (AFM;

Park Systems, XE-150). Film thickness and transmission data were measured with an optical layer thickness measurement device (Filmetrics F20-UV with LS-DT2 light source).

3. Experimental results

This section starts out from describing the enhanced PL resulting from laser-induced surface structuring and subsequent furnace annealing and hydrogen passivation (Sec. 3.1) followed by a thorough characterization of surface topographies deduced from SEM and AFM (Sec. 3.2). Subsequently, structural changes of Si-Nc related to laser irradiation are investigated by Raman spectroscopy (Sec. 3.3) and TEM-based techniques (Sec. 3.4).

3.1 Photoluminescence Measurements

First, the results of the PL measurements of all samples are presented. No sample shows measurable PL without the high-temperature annealing. Therefore, the PL data of these samples ("A","B" and "I") are not presented.

After high temperature heating, a PL signal is measurable as is shown in Figure 3 for samples without the final hydrogen passivation, i. e. samples "C" (no laser irradiation) and "G" (600nm line grating). It is noteworthy, that unlike PL enhancement due to plasmonic effects, the laser treatment of the surface increases the PL across the whole spectrum. The increase in intensity is shown in table 2. It is labeled "area fraction" and was calculated by integrating the PL spectra.

Since the shape of the PL signals indicates at least contributions from three individual bands, both data sets are fitted with three individual Gaussian functions (fits not shown in graph). The resulting positions of the Gaussian functions (λ_i; i=1,2,3) and their relative area fractions (f_i) are listed in table 2. As it can be seen from the positions of the Gaussian functions, the PL peaks undergo a blue shift when comparing the data of the laser-treated sample with the data of the non-laser treated sample. The blueshift of the main-peak amounts to 19 nm.

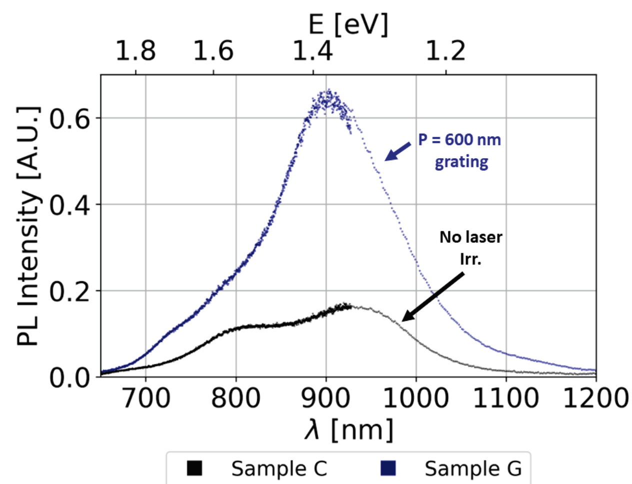

Figure 3. PL spectra of SiO_x samples after high-temperature annealing without hydrogen passivation. A significant enhancement of the PL due to the periodic structuring is measurable. The PL intensity is shown in uncalibrated units but scaled identically in all measurements.

A further PL signal enhancement is obtained if a final hydrogen passivation is added to the processing scheme. This is shown in Figure 4 for those samples ("D", "E", "F" and "H") subjected to hydrogen passivation. The enhancement of the PL signal due to hydrogen passivation was calculated by integrating the PL spectra. The results are listed in table 2. Besides the signal increase, a redshift of the main peak of about 8 nm for the samples without laser processing (sample "C" and "D") and a redshift of about 20 nm for the samples with the grating structure with a period of 600 nm (samples "G" and "H") can be

measured. When comparing the shape of the PL spectra, it is also clear that the spectra are more symmetrical after hydrogen passivation than before hydrogen passivation. In detail, it can be seen that the increase in PL intensity mainly affects the main peak around 900 nm, while the side peaks around 700 nm to 800 nm are much less affected by the hydrogen passivation.

Furthermore, as before hydrogen passivation, the PL signal is dependent on the surface laser treatment. The enhancements are summarized in table 2.

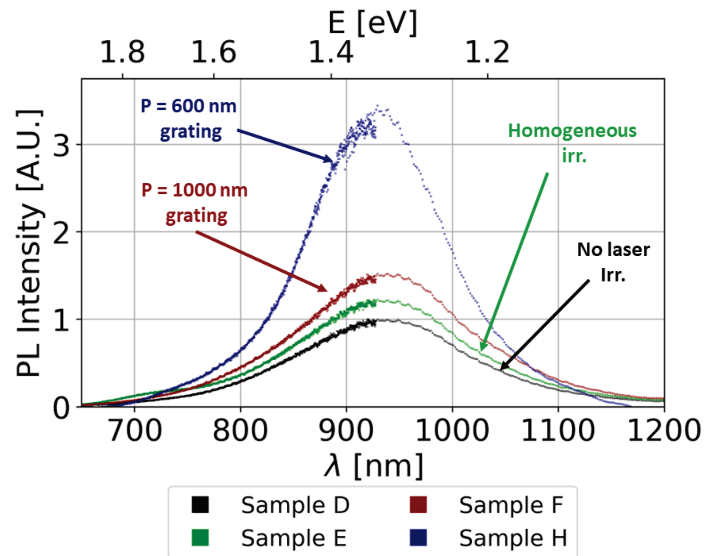

Figure 4. PL spectra of high-temperature annealed and hydrogen passivated SiO_x samples. Homogeneous laser irradiation of the SiO_x layer results in a slight increase in the PL signal. Periodic structuring of the SiO_x layer results in a significantly stronger enhancement of the PL signal. The enhancement depends on the period of the structure. PL intensity scaling identical to Figure 3.

Sample	Area fraction	λ_1 [nm]	f_1 [%]	λ_2 [nm]	f_2 [%]	λ_3 [nm]	f_3 [%]	Hydrogen passivation	Period [nm]
C	0.2	710	5.3	800	23.3	929	71.4	-	No Irr.
D	1	736	2.9	763	0	937	97.1	+	No Irr.
E	1.3	724	4.7	793	0.5	936	94.8	+	∞
F	1.5	732	2.4	793	1.2	939	96.4	+	1000
G	0.5	738	6.8	786	2.3	910	90.9	-	600
H	2.6	739	1.7	787	1.7	929	96.6	+	600

Table 2. Results of PL measurements: Area fraction denotes the integrated area relative to that of sample D. λ_i (i=1,2,3) denote positions of three Gaussians fitted to each spectrum and f_i their relative area fraction. For each sample it is indicated whether hydrogen passivation was performed. The structure period resulting from laser irradiation is indicated for each sample. "No Irr." means that no laser irradiation was carried out.

In summary, no PL is measurable without high-temperature annealing. High-temperature annealing results in measurable PL, which can be enhanced by subsequent hydrogen passivation. Specific laser structuring of the surface results in enhanced PL. In the following chapters, the individual studies of the samples for identifying the causes of the PL enhancement are presented.

3.2 AFM and SEM measurements of the laser irradiated samples

In this section, analyses of surface structures by AFM and SEM measurements of the laser irradiated SiO_x surfaces are shown (samples "E", "F", "G", "H" and "I"). The laser irradiation with homogeneous fluence (500 mJ/cm², one laser pulse, sample "E") across the area results in a rather smoothly ablated area with a depth of about 100 nm. Results of such experiments, concerning the ablation behavior, can be found in the literature [44].

The structured irradiation results in a line grating on the surface formed by SiO_x ablation. Results regarding the ablation process can also be found in literature and are therefore only briefly discussed here [45]. The height profile corresponds to the fluence distribution on the sample during ablation and is sinusoidal in shape. The period of the line grating generated with the Schwarzschild-objective is about 594 ± 16 nm and the period of the grating generated with the objective lens is about 1020 ± 20 nm. In both cases, one laser pulse was used at a fluence of 640 mJ/cm² (averaged over the entire area). An SEM image of the structured SiO_x surface with the grating produced with the Schwarzschild-objective (sample "H") can be seen in Figure 5. The line structure shows a uniform period and mostly smooth surfaces. Some defects, like pores, can be seen on the surface. Isolated surface impurities are also visible. AFM measurements show a variation in the height of the structures ranging from 80 nm to 140 nm, depending on the location in the laser irradiated spot. AFM measurements of the structured SiO_x surface with the grating produced with the objective lens (sample "F") show a structure height of 90 nm to 150 nm.

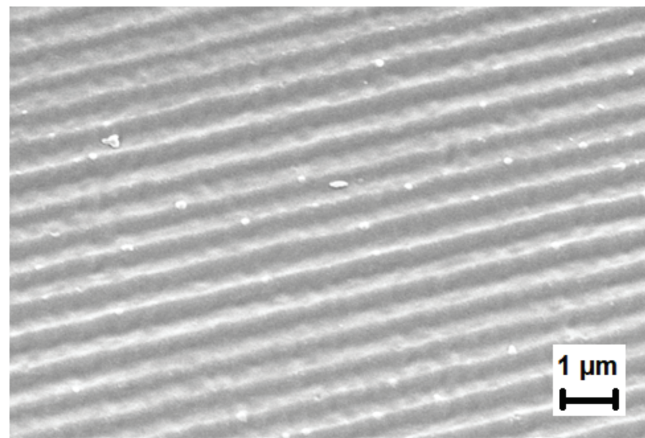

Figure 5. SEM image of the cleaned SiO_x surface of sample "H". To avoid charging during SEM inspection, the sample was homogeneously coated with 20 nm of gold. The laser irradiation results in a sine-shape line grating with a period of 594 ± 16 nm. Laser parameters: λ=193 nm, 1 pulse, 640 mJ/cm² (fluence averaged over entire area). SEM parameters: 0° observation angle; 20 kV; 5.5 mm Working Distance.

3.3 Raman measurements

Raman measurements were carried out to investigate structural effects on the SiO_x layers due to the furnace processes and laser processing. Prior to the high-temperature annealing, Raman measurements show an unspecific signal (Figure 6). Only a slight difference between the sample with the 600 nm grating (sample "I") and the sample without laser processing (sample "A") is visible around 470 cm^{-1} as a broad and non-intense peak. This peak could indicate amorphous silicon with a significant amount of (non-radiative) heterogeneous defect states [22] [46]. Heating at low temperature for the purpose of passivation (540 °C, sample "B") does not change the signal significantly (data not shown). High-temperature annealing changes the Raman signal significantly. Measurements of a SiO_x sample without laser processing (sample "D") and with a 600 nm grating structure (sample "H") are shown. The sharp peak at 515 cm^{-1} can be attributed to crystalline silicon [47]. This indicates the thermally induced phase separation producing crystalline silicon. No clear difference is measurable between the Raman signals of the heated samples with

and without laser irradiation. All Raman measurements have been corrected for a measurement of the SiO_2 substrate. These structural studies are complemented by TEM analyses in the following chapter.

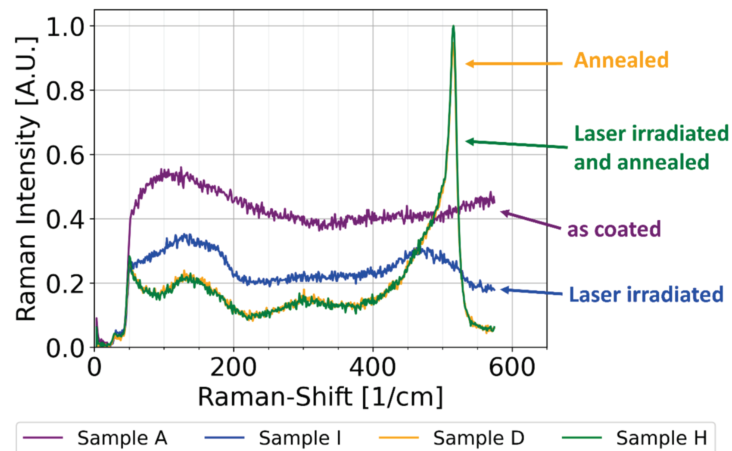

Figure 6. Raman measurements of different SiO_x samples. Prior to the high-temperature annealing an unspecific signal is present (sample "A"). Laser treatment causes a shallow, broad peak around 470 cm^{-1} (sample "I"). The high-temperature annealing (1050 °C) results in a sharp peak at 515 cm^{-1}, while there is no difference in Raman-signals between laser processed and unprocessed samples (samples "D" and "H"). The measurements of the substrate have been subtracted.

3.4 TEM measurements

TEM measurements were performed to investigate the structural properties of the as-coated SiO_x layer (sample "A") and the influence of the furnace (sample "H") and laser processes (sample "I").

Without further processing, the SiO_x coatings (sample "A") show no indications of silicon nanoparticles. Therefore, the TEM images are not shown. A native oxide layer SiO_2 of 3 nm thickness is measurable on the surface. This is also confirmed by measurements with the optical layer thickness measurement device.

STEM-EDX measurements show a constant ratio of silicon to oxygen throughout the SiO_x layer with an average composition of $SiO_{1.08 \pm 0.02}$ prior to the high-temperature annealing and $SiO_{1.02 \pm 0.02}$ after the high-temperature annealing. These minor differences in oxygen content may have occurred during production or processing and should not be attributed to the annealing process. Partial inhomogeneities inside the SiO_x with a cluster size below 1 nm indicate the presence of amorphous silicon clusters.

Laser structuring produces surface structures as visible in the TEM cross-sections in Figure 7 a) and b). Figure 7 a) shows a periodic surface profile with a peak height of 80 nm of the sample, which was laser structured with a grating with a period of 600 nm without subsequent furnace processes (sample "I"). This part will be discussed in more detail first. An overview of the cross section is shown in the left part. The entire SiO_x layer with the interface to the substrate in the lower part is visible. Part of the image was replaced with the energy filtered image for 17 eV (silicon plasmonic energy loss highlighting nanoparticles) to get an overview of the entire SiO_x layer. It is evident that silicon nanoparticles are present near the surface. This can be deduced from the region marked green, which is shown as enlarged energy filtered STEM images for energy losses of 17 eV and 23 eV corresponding to plasmonic losses in silicon and silicon oxide, respectively. Here, the occurrence of silicon nanoparticles near the surface is clearly visible. It is supported by HRTEM measurements close to the surface (Figure 7 c)). An important observation is a distinct size gradient with the size of the silicon nanoparticles decreasing with distance from the surface. The depth of the silicon nanoparticles layer is measured to be 110 nm

under the hills and 75 nm under the valleys and therefore roughly follows a 'dampened' profile of the surface topography as shown by the dashed blue line. Below these depths, no silicon nanoparticles are detectable. A relation of the depth of silicon nanoparticles to the thermal diffusion length of SiO_x for 20 ns laser pulses is suggestive, since the depth of the silicon nanoparticles corresponds to this diffusion length [48]. In summary, laser irradiation, even without heating processes, produces silicon nanoparticles in a near-surface region with a distinct size gradient. The depth of the silicon nanoparticles corresponds to the thermal diffusion of the laser used for structure production. Note, however, that no PL signal within the detection limit is measurable for this sample. 350 351 352 353 354 355 356 357 358

For comparison, Figure 7 b) shows analogous data for sample 'H', which – in addition to the laser irradiation (sample 'I' shown in Fig. 7a)) – has been subjected to furnace annealing and final hydrogen passivation. As a result, silicon nanoparticles are obtained in the entire SiO_x layer. The energy filtered inset for 17 eV in the left part clearly shows two regions separated by a rather abrupt boundary with silicon nanoparticles, which differ in particle size. The boundary is indicated by the dashed blue line in the energy filtered image for 23 eV. The top area again roughly follows a dampened profile of the surface topography. It is called "laser-affected-region" and has a different depth below the valley (43 nm) and peak (150 nm). This corresponds roughly to the thermal diffusion length of SiO_x for 20ns laser pulses [48]. The SiO_x layer below this boundary is called "bulk-SiO_x" in the following. The typical sizes of the Si-Nc in the regions were determined using HRTEM measurements. Si-Nc diameters ranging from 3 nm to 5.3 nm in the "laser-affected-region" and 3.8 nm to 11.5 nm in the "bulk-SiO_x" were measured (Figure 7 d) and e)). The "bulk-SiO_x" region shows the same Si-Nc size distribution as a sample that was not laser structured prior to the heating processes (sample "D", not shown). In both cases the energy loss measurements show a homogeneous distribution of amorphous silicon and silicon nanoparticles over the whole bulk SiO_x region. However, an increase of the Si-Nc size in close vicinity to the substrate interface is shown, which we attribute to inhomogeneities in the initial SiO_x deposition process. 359 360 361 362 363 364 365 366 367 368 369 370 371 372 373 374 375 376 377

Comparing the TEM measurements before and after the heating process (sample "I" and "H" respectively), some aspects are striking. First, each region, the "laser-affected-region" and the "bulk-SiO_x", exhibit a homogeneous size distribution of Si-Nc after the heating process. The size gradient of silicon nanoparticles, which had been formed by the laser irradiation, was erased by the heating process. Instead of the area with the size gradient of silicon nanoparticles, an area with smaller Si-Nc has formed as a result of the heating process. It is striking here that a clear boundary appears before and after the heating process. In addition, the TEM measurements show a significantly thicker SiO_2 layer on the surface of the heated sample ("H") with 16 nm - 30 nm than the unheated sample ("I"). The largest oxide thickness occurs in the valleys, while the hills show a smaller oxide layer. The optical layer thickness measurement device measures a similar value with 20 nm, although no spatially resolved measurement is possible. The high-temperature annealing thus leads to a partial oxidation of the surface, despite the nitrogen atmosphere. Finally, we note that the apparently different amplitude of the surface gratings in Fig. 7a) (sample 'I') and 7b) (sample 'H') has to be attributed to a non-homogeneous fluence distribution in the laser spot during ablation since AFM measurements show that the heating process leaves the surface line grating unaffected. 378 379 380 381 382 383 384 385 386 387 388 389 390 391 392 393 394

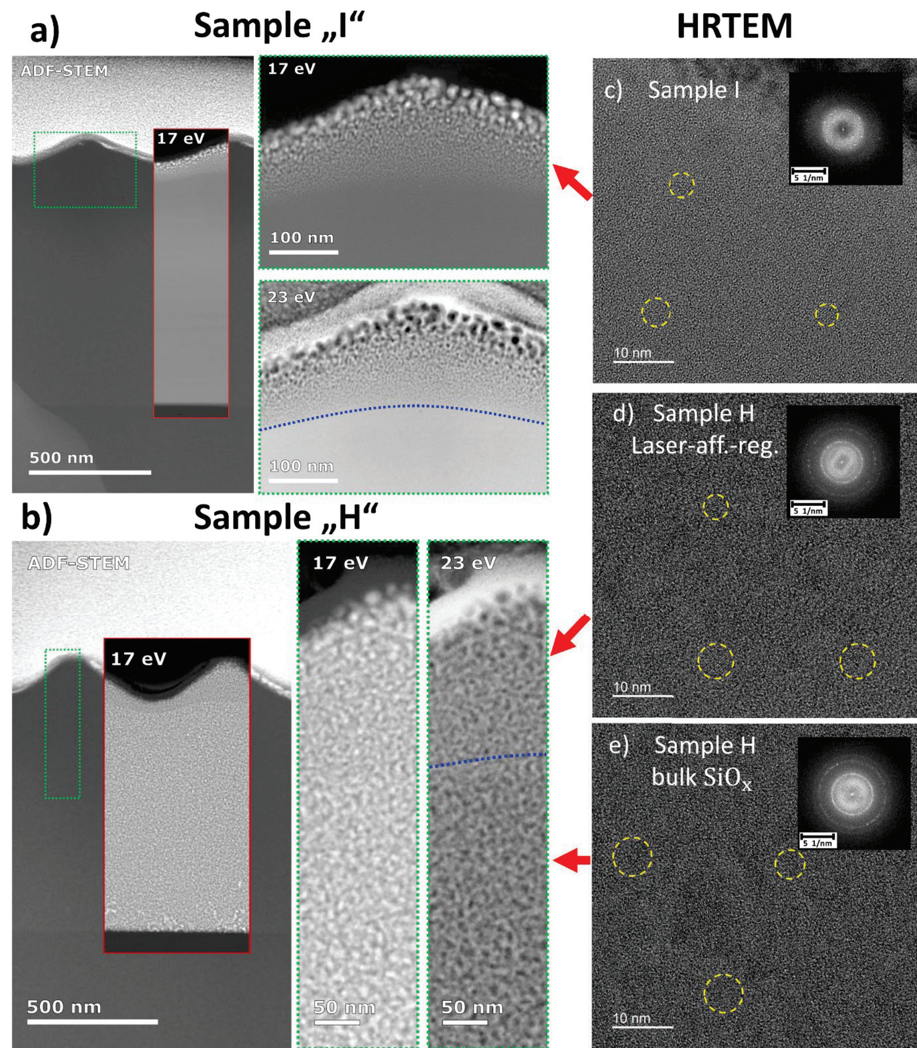

Figure 7. Selected results of the TEM/STEM analysis. (a) ADF-STEM overview of sample "I", laser-structured with a period of 600 nm and a peak height of 80 nm. The sample is coated with a poly-crystalline/amorphous Pt-C layer for the FIB preparation. Inset on the left shows the EELS fit amplitude map of the 17 eV plasmon peak, with higher intensity corresponding to regions containing more Si-rich clusters. Enlarged panels in the middle correspond to higher-resolution STEM-EELS results for a region indicated by the dashed rectangle in the ADF image. The 17 eV fit amplitude map shows the presence of large Si-Nc at the surface, with gradually decreasing cluster size following the surface topography, and roughly corresponding to the thermal diffusion length of 20 ns laser pulses in SiO_x. The 23 eV fit amplitude map correlates with the amorphous SiO_x content within the sample, consequently creating a roughly contrast-inverted image of the 17 eV map and showing highest intensity within the SiO_2 surface layer. The dashed blue line indicates the boundary of the area containing Si-Nc. Panel (c) on the right displays the HRTEM structure at the top of the irradiated layer in (a), with selected Si-Nc visible by their lattice planes highlighted by dashed yellow circles. These irregularly-shaped crystallites can possess a wide range of sizes, typically between 3 nm and 5.3 nm. Crystallinity within the HRTEM image is further highlighted by Bragg spot intensity in the Fourier-transformed (FT) of the image (inset in (c)). Panel (b) is organized similarly, showing an ADF overview and STEM-EELS results from the laser irradiated, high-temperature annealed and hydrogen passivated sample "H" with a period of 600 nm and increased peak height (140 nm). The 17 eV STEM-EELS results in particular reveal the presence of two crystalline domains of different average Si-Nc size, corresponding to the laser-crystallized and the bulk-annealed regions of the sample. The interface between the two regions is approximately indicated by the dashed blue line. This map also shows an increase in the thickness of the SiO_2 surface layer. The HRTEM images in (d) and (e) demonstrate representative examples of the crystalline structures in the top (d) and bottom domain (e), and their corresponding FTs displaying diffraction rings from the Si-Nc. Crystallite

sizes in the annealed bulk are significantly larger than in the laser-affected region, ranging from 3.8 to 11.5 nm. Si-Nc in both layers are closely packed, so that a more precise determination of sizes is not possible due to overlap between neighboring particles. Laser parameters: λ=193 nm, 1 pulse, 640 mJ/cm^2 (fluence averaged over entire area).

4. Discussion

4.1 Si-Nc size, PL and hydrogen passivation

The main PL peak originates from Si-Nc with a broad size distribution. TEM measurements show mainly sizes between 3 nm and 6 nm. Similar spectra are also observed in literature, although the PL peak position heavily depends on the host matrix, the measurement temperature and the surface chemistry beside the diameter of the crystals. A range of Si-Nc sizes and corresponding PL peak positions have been reported in literature as summarized in Sec. 1. The PL peak position with respect to the Si-Nc size is in the range of values reported in the literature, especially for SiO_x host matrix (see Refs. [4] [19] [20] [49] [50]).

The PL redshift due to hydrogen passivation has also been measured in literature [51]. It is known that large Si-Nc (producing low energy PL) have longer PL lifetimes compared to smaller Si-Nc [52]. As a result, hydrogen passivation, which reduces non-radiative processes, has a greater effect on the low energy PL spectrum. This results in a redshift of the PL spectrum. Other authors suggest another explanation for the PL redshift induced by hydrogen passivation: Si-Nc with larger diameters have a larger surface area. These then statistically have more nonradiative defects, which are suppressed by the hydrogen passivation. Thus, the hydrogen passivation has a stronger effect on larger Si-Nc, which has been attributed to a redshift in the PL spectrum [51]. The increase in PL signal due to the hydrogen passivation is in good agreement with similar experiments in the literature [13] [30] [51].

The minor PL peaks around 700 nm to 800 nm are almost unaffected by hydrogen passivation. In the literature, formation of defect related PL due to oxygen vacancies and defects, such as non-bridging oxygen hole centers (NBOHC) and oxygen-deficiency center (ODC) causing PL signals below 900 nm, is mentioned [1] [53] [54] [55]. Also, amorphous silicon nanoclusters with broad band PL in the range of 650 nm to 775 nm is reported [1] [53]. In our STEM experiments such nanoclusters should show up in the energy-filtered images (17 eV) in the absence of crystalline diffraction spots, which is not observed experimentally. Hence, there is no indication for amorphous silicon clusters leaving defect related PL as the most likely explanation for these PL bands.

4.2 Influence of the surface grating on the PL

Regarding the topography, an increase in the PL signal is measurable for all samples with surface gratings compared to samples with flat surfaces. Firstly, the laser irradiation leads to structural changes in the material, as shown by the TEM analysis. The blue shift of the PL peaks and the PL enhancement could be due to the smaller Si-Nc size in the laser-affected-region resulting from an enhanced nucleation rate for Si-Nc there as mentioned without further explanation in [39]. However, the PL enhancement cannot be explained by this effect alone. This is due to the fact that the samples irradiated with the laser with homogeneous fluence over a large area do not show such a strong increase of the PL signal as the samples with a surface grating. Meanwhile, the introduction of nucleation sites by the laser irradiation should occur similarly in both cases. Therefore, this can at best explain only a small portion of the PL signal enhancement and points to another effect. The dependence of the PL enhancement on the period of the gratings (samples "F" and "H") suggests an optical effect.

The influence of the grating on the PL in connection with the excitation light can be neglected. A grating coupling of the PL excitation light into the SiO_x layer, as known from grating couplers to planar waveguides, would be possible. However, due to the period of 600 nm and 1000 nm present here, only parts of higher orders can couple into the SiO_x

layer. Since the contributions of these high orders are very small, this effect can be neglected (a more detailed discussion of this point can be found in the supplementary material).

We now discuss the effect of the grating on PL light emission. To analyze this behavior, finite element simulations were performed. A unit cell (size corresponding to the period of the surface grating) was simulated with the refractive indices n_{SiOx} =1.9 and n_{SiO2} =1.45, neglecting any absorption [56] [57]. Scattering boundary conditions with perfectly matched layers and periodic boundary conditions are assumed. The radiation of the PL from the Si-Nc is assumed to be isotropic. For simplification, a plane wave traveling in the direction of the sample surface with different angles (ψ) is assumed in the simulations (a schematic sketch is shown in the supplementary material: Figure Sup.2). A wavelength of 950 nm is assumed and the periodic surface structure is assumed to be sinusoidal in shape with an amplitude of 100 nm. This model is used to calculate the angular spectrum for total internal reflection. A "cutoff-angle" (denoted θ) was defined. For angles higher than θ, less than 1 % of the PL light leaves the SiO_x layer (meaning 99 % of the PL light is reflected back into the substrate). The cutoff-angle is plotted against the structure period in Figure 8 as the red data points (left axis). A clear decline in the cutoff-angle for increasing period is observed, meaning less light can exit the SiO_x layer for larger structure periods. The dashed line shows the angle of total reflection for a flat surface (θ_{fl} = 28 deg). Assuming isotropic PL emission from the Si-Nc, the PL enhancement due to the grating is estimated. The fraction of PL light that can leave the SiO_x layer is approximated by the solid angle of a given period. Divided by the solid angle for a flat surface, this gives the enhancement (ε) of the PL by the structure period:

$$\varepsilon = \sin\left(\frac{\theta}{2}\right)^2 / \sin\left(\frac{\theta_{fl}}{2}\right)^2 \quad (1)$$

This calculation yields the blue data points in Figure 8 (right axis). Since this calculation assumes an isotropic solid angle, while the grating has a preferred direction, this is only an estimate for the PL enhancement. Another simplification is made because a linear increase of the PL light output with the solid angle is assumed. Since we do not expect a linear intensity distribution of the PL light for the solid angles, this estimate shows an upper limit for the increase in PL light. Nevertheless, this method provides a quantitative estimate of the PL enhancement. The PL enhancements measured experimentally are below the calculated values and thus confirm the assumption of an upper limit. On the other hand, the PL measurement data are limited by the numerical aperture of the objective in the PL setup. Therefore, the PL measurement data should be considered as a lower limit, since not the entirety of the angular spectrum can be measured. These results finally lead to the conclusion, that the enhancement of the PL can be explained by the periodic surface gratings. The PL losses due to total internal reflection in the SiO_x layer with high refractive index are reduced by the periodic structures. Thereby the light extraction efficiency is increased.

The values measured here for the PL enhancement by increased extraction efficiency are in agreement with observed values from the literature for periodic structures. It should be noted, however, that the experiments performed here differ from the literature in important respects, since the periodic structure is introduced here into the host matrix without extrinsic elements. For the use of periodic GaN nanorods, an enhancement by a factor of 2.5, compared to a flat GaN layer, was measured [35]. In the case of the two-dimensional photonic crystal leading to an enhanced PL extraction efficiency enhancements of up to 8 was measured. However, enhancement only occurs in a small spectral range [38].

In summary, the underlying mechanisms for the increased PL signal are to a small extent structural changes induced by homogeneous or structured laser irradiation and to a major extent an increased light extraction efficiency due to the laser induced structures from the highly refractive SiO_x layer.

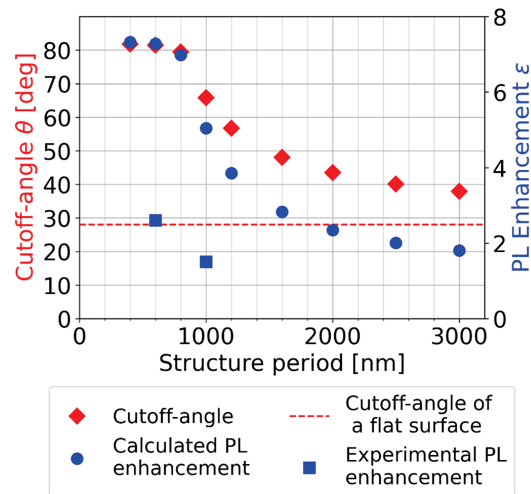

Figure 8. Comparison of calculated cutoff-angles and PL enhancement for varying structure period at fixed sinusoidal amplitude of 100 nm for a wavelength of 950 nm. The cutoff-angle (red data, left axis) is defined as the emission angle at which less than 1% of PL light can exit the SiO_x layer. The dashed line shows the cutoff-angle for a flat sample (28 deg). The blue data shows the calculated and measured PL enhancement (right axis) due to the periodic surface grating compared to a flat surface.

5. Conclusions

An increase in the PL intensity of Si-Nc inside a SiO_x layer can be observed due to irradiation with an ArF-excimer laser. In the case of homogeneous fluence, a slight increase in PL occurs. Structuring the surface with a periodic grating results in a significantly stronger enhancement of the PL. The enhancement depends on the period of the structure. Part of the PL increase is due to the Si-Nc crystallization behavior due to laser irradiation of the SiO_x layer. However, a large part of the PL increase is unrelated to this. The reduction in the loss of PL light due to total internal reflection by the periodic surface structure can explain the enhancements. A simple and inexpensive method for increasing the PL intensity of Si-Nc inside a SiO_x layer has been demonstrated.

6. Declarations

Funding

We acknowledge the financial support of the Deutsche Forschungsgemeinschaft, project IH 17/27-1 and 217133147/SFB 1073, project Z02.

Conflicts of interests

The authors have no competing interests to declare that are relevant to the content of this article.

7. Supplementary materials

7.1 Interaction of the grating with the PL excitation light

The influence of the surface grating on the optical excitation of the PL was investigated. It is known that optical gratings in combination with thin layers can lead to the coupling of light into the layer, which then guides the light. These sometimes called "resonant-grating-waveguide-structures" exhibit a strong enhanced electric field inside the layer and can potentially increase the PL of luminescent particles inside the layer [58] [59]. Waveguide coupling of light (wavelength λ) incident at an angle φ on a thin layer (of refractive index n_{SiOx}) with a surface grating of period P is satisfied for [59]:

$$n_{SiO_2} \leq \left|\sin\varphi - m\,\frac{\lambda}{p}\right| < n_{SiO_x} \quad (2)$$

With m denoting the diffraction order and n_{SiO2} the refractive index of the substrate. The angles of incidence satisfying this condition are plotted against the structure period in Figure Sup1. A refractive index of n_{SiOx} = 2.14 and n_{SiO2} = 1.47 and wavelength of λ = 405 nm was assumed [56] [57]. The dashed line shows the maximum angle of incidence, limited by the numerical aperture of the objective in the PL setup (NA = 0.6). For a period of 600 nm there is only a coupling of parts of the ±3 and +2 diffraction order. For a period of 1000, nm there is only a coupling of parts of the +3-diffraction order. The diffraction efficiency η_m of the individual diffraction orders can be estimated by the Bessel-function of first kind J_m in dependence on the structure height "h" [60]:

$$\eta_m = \left|J_m\left(\frac{\pi(n_{SiO_x}-1)h}{\lambda}\right)\right|^2 \quad (3)$$

Calculations show a share of 0.3 % to 2.8 % for the ±2 order and less than 0.1 % for the ±3 order for the structure heights occurring in the experiments. Since these fractions are very small, compared to the non-coupling fractions, the influence of the grating on the excitation mechanism and any resulting enhancement of the PL signal is considered insignificant.

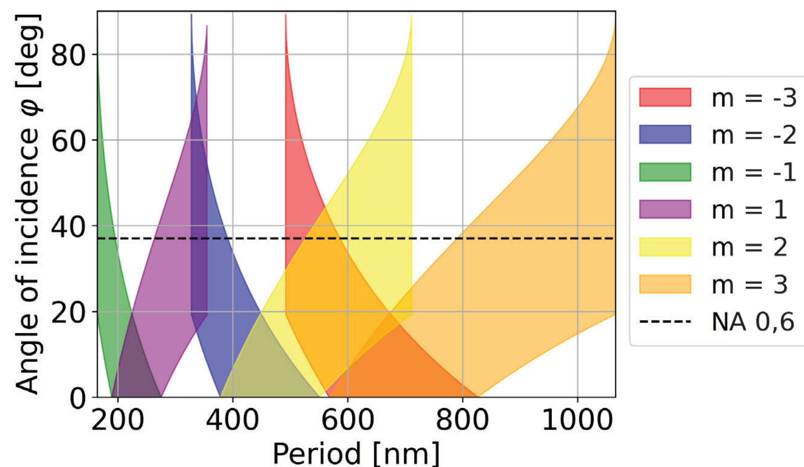

Figure Sup1. Simulation results of guided-mode resonance according to equation 2 for orders m = -3 to m = 3. The dashed line represents the maximum angle of incidence of the excitation light due to the numerical aperture of the lens (NA = 0.6).

7.2 Finite element simulation model 580

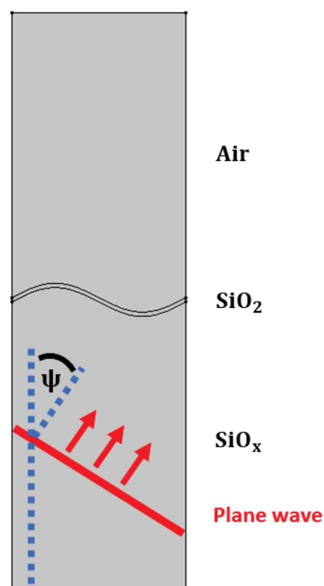

581

Figure Sup2. Model of the finite element simulations regarding the "cutoff-angle" of the PL light. Plane waves propagating at variable angles (ψ) towards the substrate surface are assumed for the isotropic PL light of the Si-Nc. The dashed blue line is drawn only to mark the angle. 582 583 584

585

8. References 586

1. Pavesi, L.; Turan, L. **2010**, *Silicon Nanocrystals Fundamentals, Synthesis and Applications* Wiley-VCH, ISBN: 978-3-527-32160-5. 587 588

2. L. T. Canham. Silicon quantum wire array fabrication by electrochemical and chemical dissolution of wafers. *Appl. Phys. Lett.* **1990**, *57*, pp. 1046 – DOI: https://doi.org/10.1063/1.103561. 589 590 591

3. Cullis, A. G.; Canham, L. T. Visible light emission due to quantum size effects in highly porous crystalline silicon. *Nature* **1991**, *353*, pp. 335-338 - DOI: https://www.nature.com/articles/353335a0. 592 593 594

4. Zacharias, M.; Heitmann, J.; Scholz, R.; Kahler, U.; Schmidt, M.; Bläsing, J. Size-controlled highly luminescent silicon nanocrystals: A SiO/SiO_2 superlattice approach. *Appl. Phys. Lett.* **2002**, *80*, pp. 661 – DOI: https://doi.org/10.1063/1.1433906. 595 596 597

5. Tiwari, S.; Rana, F.; Hanafi, H.; Hartstein, A.; Crabbé, E. F.; Chan, K. A silicon nanocrystals based memory. *Appl. Phys. Lett.* **1996**, 68, pp. 1377 – DOI: https://doi.org/10.1063/1.116085. 598 599 600

6. Pavesi, L; Dal Negro, L; Mazzoleni,C; Priolo, F. Optical gain in silicon nanocrystals. *Nature* **2000**, 408, pp. 440 – DOI: https://doi.org/10.1038/35044012. 601 602

7. Ledoux, G.; Guillois, O.; Porterat, D.; Reynaud, C.; Huisken, F.; Kohn, B.; Paillard, V. Photoluminescence properties of silicon nanocrystals as a function of their size. *Phys. Rev. B* **2000**, 62, pp. 15942 – DOI: https://doi.org/10.1103/PhysRevB.62.15942. 603 604 605

8. Walters, R. J.; Bourianoff, G. I.; Atwater, H. A. Field-effect electroluminescence in silicon nanocrystals. *Nat. Mater.* **2005**, 4, pp. 143 – DOI: https://doi.org/10.1038/nmat1307. 606 607

9. Jurbergs, D.; Rogojina, E. Silicon nanocrystals with ensemble quantum yields exceeding 60%. *Appl. Phys. Lett.* **2006**, 88, pp. 233116 – DOI: https://doi.org/10.1063/1.2210788. 608 609

10. Sinelnikov, R.; Dasog, M.; Beamish, J.; Meldrum, A.; Veinot, J. G. C. Revisiting an Ongoing Debate: What Role Do Surface Groups Play in Silicon Nanocrystal Photoluminescence? *ACS Photonics* **2017**, 4, pp. 1920 – DOI: https://doi.org/10.1021/acsphotonics.7b00102. 610 611 612 613

11. Ledoux, G.; Gong, J.; Huisken, F. Effect of passivation and aging on the photoluminescence of silicon nanocrystals. *Appl. Phys. Lett.* **2001**, 79, pp. 4028 – DOI: https://doi.org/10.1063/1.1426273. 614 615 616

12. Wilson, W. L.; Szajowski, P. F.; Brus, L. E. Quantum Confinement in Size-Selected, Surface-Oxidized Silicon Nanocrystals. *Science* **1993**, 262, pp. 1242-1244 – DOI: https://doi.org/10.1126/science.262.5137.1242. 617 618 619

13. Godefroo, S.;Hayne, M.; Jivanescu, M.; Stesmans, A.; Zacharias, M.; Lebedev, O. I.; Van Tendeloo, G.; Moshchalkov, V. V. Classification and control of the origin of photoluminescence from Si nanocrystals. *Nat. Nanotechnol.* **2008**, 3, pp. 174 – DOI: https://doi.org/10.1038/nnano.2008.7. 620 621 622 623

14. Lee, B.G.; Hiller, D.; Luo, J.-W.; Semonin, O.E.; Beard, M.C.; Zacharias, M.; Stradins, P. Strained Interface Defects in Silicon Nanocrystals. *Adv. Funct. Mater.* **2012**, 22, pp. 3223 – DOI: https://doi.org/10.1002/adfm.201200572. 624 625 626

15. Hadjisavvas, G. and Jelire, P. C. Structure and Energetics of Si Nanocrystals Embedded in a−SiO_2. *Phys. Rev. Lett.* **2004**, 93, pp. 226104 – DOI: https://doi.org/10.1103/physrevlett.93.226104. 627 628 629

16. Belyakov, V. A.; Burdov, V. A.; Lockwood, R.; Meldrum, A. Silicon Nanocrystals: Fundamental Theory and Implications for Stimulated Emission. *Advances in Optical Technologies* **2008**, 32, pp. 279502 – DOI: https://doi.org/10.1155/2008/279502. 630 631 632

17. Schmidt, T.; Chizhik, A. I.; Chizhik, A. M.; Potrick, K.; Meixner, A. J.; Huisken, F. Radiative exciton recombination and defect luminescence observed in single silicon nanocrystals. *Phys. Rev. B* **2012**, 86, pp. 125302 – DOI: https://doi.org/10.1103/PhysRevB.86.125302. 633 634 635 636

18. Wang, L.; Li, Q.; Wang, HY.; Huang, J.-C.; Zhang, R.; Chen, Q.-D.; Xu, H.-L.; Han, W.; Shao, Z.-Z.; Sun, H.-B. Ultrafast optical spectroscopy of surface-modified silicon quantum dots: unraveling the underlying mechanism of the ultrabright and color-tunable photoluminescence. *Light Sci. Appl.* **2015**, 4, pp. 245 – DOI: https://doi.org/10.1038/lsa.2015.18. 637 638 639 640

19. Kahler, U.; Hofmeister, H. Size evolution and photoluminescence of silicon nanocrystallites in evaporated SiO_x thin films upon thermal processing. *Appl. Phys. A* **2002**, 74, pp. 13-17 – DOI: https://doi.org/10.1007/s003390100993. 641 642 643

20. Iacona, F., Franzò, G.; Spinella, C. Correlation between luminescence and structural properties of Si nanocrystals. *Appl. Phys.* **1999**, 87, pp. 1295 – DOI: https://doi.org/10.1063/1.372013. 644 645 646

21. Kahler, U.; Hofmeister, H. Visible light emission from Si nanocrystalline composites via reactive evaporation of SiO. *Opt. Mater.* **2001**, 17, pp. 83 – DOI: https://doi.org/10.1016/S0925-3467(01)00024-6. 647 648 649

22. Fricke-Begemann, T.; Wang, N.; Peretzki, P; Seibt, M.; Ihlemann, J. Generation of silicon nanocrystals by damage free continuous wave laser annealing of substrate-bound SiO_x films. *J. Appl. Phys.* **2015**, 118, pp. 124308 – DOI: http://dx.doi.org/10.1063/1.4931670. 650 651 652

23. Kenyon, A. J.; Trwoga, P. F.; Pitt, C. W.; Rehm, G. The origin of photoluminescence from thin films of silicon-rich silica. *J. Appl. Phys.* **1996**, 79, pp. 9291 – DOI: https://doi.org/10.1063/1.362605. 653 654 655

24. Wu, X. L.; Siu, G. G.; Tong, S., Liu, X. N.; Yan, F.; Jiang, S. S.; Zhang, X. K.; Feng, D. Raman scattering of alternating nanocrystalline silicon/amorphous silicon multilayers. *Appl. Phys. Lett.* **1996**, 69, pp. 523 – DOI: https://doi.org/10.1063/1.117774. 656 657 658

25. Kim, T.-W.; Cho, C.-H.; Kim, B.-H.; Park, S.-J. Quantum confinement effect in crystalline silicon quantum dots in silicon nitride grown using SiH_4 and NH_3. *Appl. Phys. Lett.* **2006**, 88, pp. 123102 - DOI: https://doi.org/10.1063/1.2187434. 659 660 661

26. Charvet, S.; Madelon, R.; Gourbilleau, F.; Rizk, R. Spectroscopic ellipsometry analyses of sputtered Si/SiO_2 nanostructures. *J. Appl. Phys.* **1999**, 85, pp. 4032 – DOI: https://doi.org/10.1063/1.370307. 662 663 664

27. Biteen, J. S.; Pacifici, D.; Lewis, N. S.; Atwater, H. A. Enhanced Radiative Emission Rate and Quantum Efficiency in Coupled Silicon Nanocrystal-Nanostructured Gold Emitters., *Nano Lett.* **2005**, 5, pp. 1768 - DOI: https://doi.org/10.1021/nl051207z. 665 666 667

28. Kanemitsu, Y.; Shimizu, N.; Komoda, T.; Hemment, P. L. F.; Sealy, B. J. Photoluminescent spectrum and dynamics of Si+-ion-implanted and thermally annealed SiO_2 glasses. *Phys. Rev. B* **1996**, 54, pp. R14329(R) – DOI: https://doi.org/10.1103/PhysRevB.54.R14329. 668 669 670

29. Shimizu-Iwayama, T.; Fujita, K.; Nakao, S.; Saitoh, K.; Fujita, T.; Itoh, N. Visible photoluminescence in Si+-implanted silica glass. *J. Appl. Phys.* **1994**, 75, pp. 7779 – DOI: https://doi.org/10.1063/1.357031. 671 672 673

30. López, M.; Garrido, B.; García, C.; Pellegrino, P.; Pérez-Rodíguez, A.; Morante, J. R.; Bonagos, C.; Carrada, M.; Claverie, A. Elucidation of the surface passivation role on the photoluminescence emission yield of silicon nanocrystals embedded in SiO_2. *Appl. Phys. Lett.* **2002**, 80, pp. 1637 – DOI: https://doi.org/10.1063/1.1456970. 674 675 676 677

31. Mangolini, L. Synthesis, properties, and applications of silicon nanocrystals. *J. Vac. Sci. Technol. B* **2013**, 31, pp. 020801 – DOI: https://doi.org/10.1116/1.4794789. 678 679

32. Richter, L. J., Ihlemann, J. Photoluminescence enhancement of silicon nanocrystals by excimer laser implanted gold nanoparticles. *Appl. Phys. A* **2022**, 128, pp. 764 – DOI: https://doi.org/10.1007/s00339-022-05906-1. 680 681 682

33. Shimizu, K. T.; Woo, W. K.; Fisher, B. R.; Eisler, H. J.; Bawendi, M. G. Surface-Enhanced Emission from Single Semiconductor Nanocrystals. *Phys. Rev. Lett.* **2002**, 89, pp. 117401 – DOI: https://doi.org/10.1103/PhysRevLett.89.117401. 683 684 685

34. Köthemann, R.; Golla, C.; Qu, H.; Meier, C. Influence of Gold Nanoantennas on the Photoluminescence of Silicon Nanocrystals. *Photonics* **2022**, 9, pp. 985 - DOI: https://doi.org/10.3390/photonics9120985. 686 687 688

35. Zhuang, Z.; Guo, X.; Zhang, G.; Liu B.; Zhang, R.; Zhi, T.; Tao, T.; Ge, H.; Ren, F.; Xie, Z.; Zheng, Y. Large-scale fabrication and luminescence properties of GaN nanostructures by a soft UV-curing nanoimprint lithography. *Nanotechnology* **2013**, 24, pp. 405303 – DOI: https://doi.org/10.1088/0957-4484/24/40/405303. 689 690 691 692

36. López, J. A. L.; López, J. C.; Valerdi, D. E.; Salgado, G. G; Díaz-Becerril, T.; Pedraza, A. P.; Gracia, F. J. F. Morphological, compositional, structural, and optical properties of Si-nc embedded in SiO_x films. *Nanoscale Res. Lett.* **2012**, 7, pp. 604 – DOI: https://doi.org/10.1186/1556-276X-7-604. 693 694 695 696

37. Li, W.; Wang, S.; Hu, M.; He, S.; Ge, P.; Wang, J.; Guo, Y. Y., Zhaowei, L. Enhancement of electroluminescence from embedded Si quantum dots/SiO_2multilayers film by localized-surface-plasmon and surface roughening. *Sci. Rep.* **2015**, 5, pp. 11881 – DOI: https://doi.org/10.1038/srep11881. 697 698 699 700

38. Ondic, L.; Varga, M.; Hruska, K.; Kromka, A.; Herynkova, K.; Hönerlage, B.; Pelant, I. Two-dimensional photonic crystal slab with embedded silicon nanocrystals: Efficient photoluminescence extraction. *Appl. Phys. Lett.* **2013**, 102, pp. 251111 – DOI: http://dx.doi.org/10.1063/1.4812477. 701 702 703 704

39. Chen, Y.-B.; Ren, Y.; Xiong, R.-L.; Zhao, Y.-Y.; Lu, M. Modulation of the photoluminescence of Si quantum dots by means of CO_2 laser pre-annealing. *Appl. Surf. Sci.* **2010**, 256, pp. 5116 – DOI: https://doi.org/10.1016/j.apsusc.2010.03.080. 705 706 707

40. Cha, D.; Shin, J. H.; Song, I.-H.; Han, M.-K. Enhanced formation of luminescent nanocrystal Si embedded in Si/SiO_2 superlattice by excimer laser irradiation. *Appl. Phys. Lett.* **2004**, 84, pp. 1287 – DOI: https://doi.org/10.1063/1.1650037. 708 709 710

41. Rodríguez-de Marcos, L. V.; Larruquert, J. I.; Méndez, J. A.; Aznárez, J. A. Self-consistent optical constants of SiO_2 and Ta_2O_5 films. *Opt. Mater. Express* **2016**, 6, pp. 3622 – DOI: https://doi.org/10.1364/OME.6.003622. 711 712 713

42. Wang, N.; Fricke-Begemann, T.; Peretzki, P., Ihlemann, J.; Seibt, M. Formation of porous silicon oxide from substrate-bound silicon rich silicon oxide layers by continuous-wave laser irradiation. *J. Appl. Phys.* **2018**, 123, pp. 093104 – DOI: https://doi.org/10.1063/1.5019404. 714 715 716 717

43. Schamm, S. Bonafos, C.; Coffin, H.; Cherkashin, N.; Carrada, M.; Assayag, G. B.; Claverie, A.; Tencé, M.; Colliex, C. Imaging Si nanoparticles embedded in SiO_2 layers by (S)TEM-EELS. *Ultramicroscopy* **2008**, 108, pp. 346 – DOI: https://doi.org/10.1016/j.ultramic.2007.05.008. 718 719 720 721

44. Jahn, M.; Richter, J.; Weichenhain-Schriever, R.; Meinertz, J.; Ihlemann, J. Ablation of silicon suboxide thin layers. *Appl. Phys. A* **2010**, 101, pp. 533 – DOI: https://doi.org/10.1007/s00339-010-5892-9. 722 723 724

45. Karstens, R.; Gödecke, A.; Prießner, A. Ihlemann, J. Fabrication of 250-nm-hole arrays in glass and fused silica by UV laser ablation. *Optics & Laser Technology* **2016**, 83, pp. 16 – DOI: https://doi.org/10.1016/j.optlastec.2016.03.020. 725 726 727

46. Voutsas, A. T.; Hatalis, M. K.; Boyce, J.; Chiang, A. Raman spectroscopy of amorphous and microcrystalline silicon films deposited by low-pressure chemical vapor deposition. *J. Appl. Phys.* **1995**, 78, pp. 6999 – DOI: https://doi.org/10.1063/1.360468. 728 729 730

47. Parker, J. H.; Feldman, J. D. W.; Ashkin, M. Raman Scattering by Silicon and Germanium. *Phys. Rev.* **1967**, 155, pp. 712 – DOI: https://doi.org/10.1103/PhysRev.155.712. 731 732

48. Ihlemann, J.; Meinertz, J.; Danev, G. Excimer laser ablation of thick SiO_x-films: Etch rate measurements and simulation of the ablation threshold. *Appl. Phys. Lett.* **2012**, 101, pp. 091901 – DOI: https://doi.org/10.1063/1.4748127. 733 734 735

49. Takeoka, S., Fuji, M.; Hayashi, S. Size-dependent photoluminescence from surface-oxidized Si nanocrystals in a weak confinement regime. *Phys. Rev. B* **2000**, 62, pp. 16820 – DOI: https://doi.org/10.1103/PhysRevB.62.16820. 736 737 738

50. Ledoux, G.; Gong, J.; Huisken, F.; Guillois, O.; Reynaud, C. Photoluminescence of size-separated silicon nanocrystals: Confirmation of quantum confinement. *Appl. Phys. Lett.* **2002**, 80, pp. 25 – DOI: Photoluminescence of size-separat. 739 740 741

51. Cheylan, S.; Elliman, R.G. Effect of hydrogen on the photoluminescence of Si nanocrystals embedded in a SiO_2 matrix. *Appl. Phys. Lett.* **2001**, 78, pp. 1225 – DOI: https://doi.org/10.1063/1.1338492. 742 743 744

52. Garcia, C., Garrido, B.; Pellegrino, P.; Ferre, R.; Moreno, J. A.; Morante, J. R.; Pavesi, L.; Cazzanelli, M. Size dependence of lifetime and absorption cross section of Si nanocrystals embedded in SiO_2. *Appl. Phys. Lett.* **2003**, 82, pp. 1595 – DOI: https://doi.org/10.1063/1.1558894. 745 746 747 748

53. Yi, L. X.; Heitmann, J.; Scholz, R.; Zacharias, M. Si rings, Si clusters, and Si nanocrystals—different states of ultrathin SiO_x layers. *Appl. Phys. Lett.* **2002**, 81, pp. 22 – DOI: https://doi.org/10.1063/1.1525051. 749 750 751

54. Sakruai, Y. Oxygen-related red photoluminescence bands in silica glasses. *J. Non-Cryst. Solids* **2003**, 316, pp. 389 – DOI: https://doi.org/10.1016/S0022-3093(02)01961-0. 752 753

55. Lau, H. W.; Tan, O. K.; Liu, Y.; Ng, C. Y.; Chen, T. P.; Pita, K.; Lu, D. Defect-induced photoluminescence from tetraethylorthosilicate thin films containing mechanically milled silicon nanocrystals. *J. Appl. Phys.* **2005**, 97, pp. 104307 – DOI: https://doi.org/10.1063/1.1899244. 754 755 756 757

56. Hass, G.; Salzberg, C. D. Optical Properties of Silicon Monoxide in the Wavelength Region from 0.24 to 14.0 Microns. *J. Opt. Soc. Am.* **1954**, 44, pp. 181 – DOI: https://doi.org/10.1364/JOSA.44.000181. 758 759 760

57. Malitson, I. H. Interspecimen Comparison of the Refractive Index of Fused Silica. *J. Opt. Soc. Am.* **1965**, 55, pp. 1205 –DOI: https://doi.org/10.1364/JOSA.55.001205. 761 762

58. Lin, J. H.; Liou, H. Y.; Wang, C.-D.; Tseng, C.-Y.; Lee, C.-T.; Ting, C.-C.; Kan, H.-C.; Hsu, C. C. Giant Enhancement of Upconversion Fluorescence of $NaYF_4:Yb^{3+},Tm^{3+}$ Nanocrystals with Resonant Waveguide Grating Substrate. *ACS Photonics* **2015**, 2, pp. 530 – DOI: https://doi.org/10.1021/ph500427k. 763 764 765 766

59. Selle, A., Dissertation „Dielektrische Wellenleitergitter in Resonanz: Theorie, Charakterisierung und Anwendung", Georg-August-Universität Göttingen **2009** – DOI: http://dx.doi.org/10.53846/goediss-2822. 767 768 769

60. Colier, R. J.; Burckhardt, C. B.; Lin, L. H., **1971**, *Optical Holography* Academic Press, ISBN: 978-0-12-181050-4. 770 771

772

773

774

Author Contributions: Conceptualization, L.J. Richter (LJR), U. Ross (UR), M. Seibt (MS) and J. Ihlemann (JI); methodology, LJR and JI.; software, LJR and UR; validation, LJR and UR; formal analysis, LJR, UR and MS; investigation, LJR and UR; resources, LJR and JI; data curation, LJR and UR; writing—original draft preparation, LJR; writing—review and editing, LJR, UR, MS and JI; visualization, LJR and UR; supervision, MS and JI; project administration, MS and JI; funding acquisition, MS and JI. 775 776 777 778 779 780

3 Summary & Discussion

3.1 Laser marking of TiO_2 containing glass

In the manuscript "UV laser generated micro structured black surface on commercial TiO_2-containing glass", a method for generating an optically visible black marking on a glass surface was presented. The marking is achieved, on the one hand, by generating a microstructure on the surface through a laser-induced phase separation into a titanium-rich and a silicon-rich phase. The microstructure causes light scattering at the surface. The marking is enhanced by the increase in absorption due to an oxygen reduction of the TiO_2. For both processes, it is therefore necessary that a certain amount of TiO_2 is contained in the glass.

An explanation for the microstructure formation in the glass could be the different properties for evaporation between alkali oxide, SiO_2 and TiO_2, similar as stated by Narazaki et al. and described in the manuscript (c. f. section 2.1) [1]. A laser irradiation near the ablation threshold induces evaporation of the alkali oxides and shifts the glass composition to a binary SiO_2 - TiO_2 system. An immiscibility of this binary system at high temperatures leads to a rutile crystal phase of TiO_2 and a silicon-rich phase during the cooldown. During the cooldown SiO_2 preferentially evaporates, creating TiO_2-rich bumps. Repeated laser induced heating results in larger structure periods and greater structure depths, as shown in the manuscript. Therefore, the bumpy structure connects to a micronetwork, leading to a strong scattering of the surface. A simultaneous laser-induced oxygen reduction of the TiO_2 to TiO_x (x < 2) by laser-induced oxygen vacancies amplifies the marking due to the increased absorption of TiO_x compared to TiO_2. The oxygen reduction was indicated by Raman measurements and also reported in the literature for similar experiments [2].

Compared to other marking methods, this process exhibits a strong contrast. Due to the combination of scattering effect and increased absorption, the markings appear deep black. Markings caused by pure scattering effects on the surface, such as markings produced by CO_2 lasers, appear grayish with low contrast. The contrast effect of the marking can be varied by the choice of observation optics, i. e. the numerical aperture. Optics with a high numerical aperture make the markings appear more blackish-greyish. Informative marking of glass surfaces in a production line is thus possible. But decorative marking of glass is also possible with this method. In addition to the strong contrast effect of the marking, the high spatial resolution of the structures is a decisive advantage. Due to their wavelength, the CO_2 lasers frequently used in industry do not achieve the resolution of the markings presented here. Therefore, this method also offers the possibility of producing significantly smaller marking features with high edge precision. Thus, both large-area markings that can be recognized by the eye but also significantly smaller and more detailed markings are possible. Another advantage is the low complexity of the process. No special gas atmosphere is required, the process works in air. Also, no addition of another substance is necessary. Thus, this process can also be used in applications where the addition of foreign materials must be avoided, for example medical packaging.

In addition to the generation of markings, other applications of this process are also conceivable. The laser irradiation generates a unique microstructure on the surface. This means that the laser irradiation of another sample with identical parameters generates a marking that is optically identically perceptible, but the exact microstructure is unique in each case, like a fingerprint. Thus, applications as a security feature would also be conceivable. Since the microstructure is in the size range of a few µm, the evaluation of the structure is, however, relatively demanding. A further application of the process could be in fluidics. It is known that microstructures on surfaces change the wetting behavior of liquids. Therefore, a change in the wetting behavior of liquids can also be expected for the structures shown here. However, no experiments have yet been carried out regarding the wetting behavior.

The main disadvantage of the method is the requirement of the TiO_2 concentration in the glass. In order to achieve the increased absorption, a certain amount of TiO_2 must be present. This is especially true for highly refractive glasses. Thus, the presented method only allows the marking of a few glass types. In addition to these glasses, the marking of coatings containing TiO_2 is also conceivable.

In summary, the process offers a high-contrast and high-resolution marking method. The use of excimer lasers makes industrial implementation possible. However, due to the requirements to the glass material, the process is limited to the niche of TiO_2 containing highly refractive glasses.

3.2 Photoluminescence enhancement of silicon nanocrystals

In the manuscripts “Photoluminescence enhancement of silicon nanocrystals by excimer laser implanted gold nanoparticles” and “Excimer laser surface patterning for photoluminescence enhancement of silicon nanocrystals”, two different laser-based methods for enhancing the photoluminescence (PL) of silicon nanocrystals (Si-Nc) in a silicon suboxide (SiO_x) matrix were presented. In both manuscripts Si-Nc were prepared by thermally induced phase separation of SiO_x layers on SiO_2 substrates. Transmission electron microscopy (TEM) measurements revealed an amorphous structure of the SiO_x coatings with a homogeneous oxygen content throughout the SiO_x layer slightly exceeding the oxygen content of SiO. Raman measurements confirmed the presence of amorphous silicon in the SiO_x layers prior to the annealing. After annealing at temperatures up to 900 °C Raman measurements showed no indication for crystallization of the amorphous silicon. Annealing at higher temperatures resulted in Raman shifts characteristic for crystalline silicon, indicating formation of silicon nanocrystals. TEM measurements confirmed the formation of Si-Nc throughout the SiO_x layer. The photoluminescence (PL) spectra of the Si-Nc show a broad PL signal, peaking around 930 nm. This indicates a broad range of Si-Nc sizes, as confirmed by TEM measurements. Minor PL contributions below 900 nm might arise from oxygen defects.

To increase the PL of the Si-Nc, two methods were demonstrated. In the first method, gold nanoparticles (Au-Np) were incorporated in the SiO_x layer. Laser irradiation of the gold-coated SiO_x surface with an UV excimer laser results in softening of the gold and SiO_x surface. This leads to an incorporation of Au-Np into the SiO_x, e. g. Au-Np implantation. The plasmon resonance of the Au-Np results in an absorbance peak around 530 nm. This is expected for spherical Au-Np, as shown in Figure 5 (section 1.2.2). The PL signal of the Si-Nc is enhanced by

the Au-Np implantation by more than twofold. An increased amount of implanted Au-Np resulted in a greater PL enhancement. The cause for the PL enhancement cannot be attributed to a single effect. First, the density of states and therefore the radiative recombination rate of the Si-Nc is altered by the presence of the Au-Np [3]. Other effects are an increased PL excitation by the interaction of the excitation light with the Au-Np and the outcoupling of non-radiative emission energies from the Si-Nc by surface plasmons [4] [5].

In the second method, the influence of homogeneous or structured excimer laser irradiation of a SiO_x layer on the PL of Si-Nc in the SiO_x layer was investigated. UV laser irradiation of the SiO_x layer results in formation of crystalline silicon close to the surface. TEM measurements reveal the depth of the crystal formation, which is approximately 100 nm. This depth corresponds to the thermal diffusion length of nanosecond laser pulses in SiO_x [6]. Laser-induced crystallization has already been observed in the literature, e. g. [7]. In our measurements a distinct size gradient of the crystalline silicon particles is observed, with the particle size decreasing with depth. High-temperature annealing of the laser irradiated SiO_x layers in a furnace process induces Si-Nc formation by phase separation in the entire layer. The size gradient of the crystalline particles was erased by the high-temperature annealing. Instead, an area close to the surface exhibits Si-Nc at smaller sizes, compared to Si-Nc at greater depths. This indicates an enhanced nucleation rate of Si-Nc in the laser-affected region. As a result, a slight enhancement and a blueshift of the PL signal is measured for a homogenous laser irradiated sample. PL measurements of laser structured samples, i. e. samples with line gratings produced by laser ablation, show a significant higher PL signal. The enhancement depends on the period of the structure, suggesting an optical effect. An explanation could be a reduced loss of PL light by total internal reflection in the highly refractive SiO_x layer, i. e. an increased outcoupling efficiency of the PL light due to the structures. An enhancement of the PL is therefore attributable to both effects, but the enhancement is significantly greater with a surface structure. It is therefore concluded that a large part of the enhancement results from the reduction of losses due to total internal reflection.

Both methods show possibilities to increase the PL of Si-Nc in the frequently used SiO_x matrix. By using excimer lasers, the methods can easily be scaled up to larger dimensions. Both methods are also characterized by uncomplicated process steps. Whereas in the literature complex processes, such as electron lithography, have to be used for the production of Au-Np, these methods can achieve an increase in PL with just a few process steps. This means that the processes are also suitable for mass applications.

However, the practical application of Si-Nc as a light emitter does not seem to be possible with these methods. If the internal quantum efficiency is compared on the basis of the radiative and non-radiative lifetimes (cf. equation (11), section 1.3.1), values close to 100 % are achieved for materials with direct bandgaps. For Si-Nc, the radiative lifetime can be reduced by a factor of 10^3 compared to bulk silicon. But the radiative lifetime in the µs-range is still significantly larger than for materials with direct bandgaps, such as GaAs (cf. section 1.3.1). An additional reduction of the radiative lifetime by a factor of 10^3 - 10^6, or a significant increase in the non-radiative lifetime, would therefore be needed for a practical application of Si-Nc as active light emitters.

However, it has been shown in the literature that the choice of experimental parameters can have a great influence on the enhancement of the PL. Thus, an increase of the PL enhancement by adjustment of experimental parameters is conceivable. For example, when implanting the Au-Np into the SiO_x, the distance of the Au-Np to the Si-Nc can be varied by SiO_2 layers to achieve a stronger enhancement. As mentioned in the manuscript (section 2.2), a decline in PL enhancement for large laser pulse numbers during the Au-Np implantation process was measured. This could be caused by oxidation of the SiO_x surface by laser irradiation. A too thick SiO_2 separation layer between the Au-Np and the Si-Nc prevents a coupling. For the structuring of the SiO_x surface for the purpose of minimizing the PL losses due to total internal reflection, an improvement of PL enhancement by another kind of structure is likely possible. It has only been shown that depending on the choice of structure, an enhancement of the PL signal is possible. Therefore, a greater variation of the structure period and a variation of the structure type is reasonable for further investigations. It has also been shown in the literature that the introduction of scattering centers can increase the outcoupling efficiency of light [8]. An investigation of this effect on Si-Nc in a SiO_x layer has not yet been carried out. It is conceivable that this effect could also occur with implanted Au-Np. More detailed investigations would have to be carried out for this.

3.3 References of the Discussion

1. *Formation of a TiO_2 Micronetwork on a UV-Absorbing SiO_2-Based Glass Surface by Excimer Laser Irradiation.* **A. Narazaki, Y. Kawaguchi, H. Niino, M. Shojiya, H. Koyo and K. Tsunetomo** 2005, Chem. Mater., Vol. 17, pp. 6651, DOI: https://doi.org/10.1021/cm0518372.

2. *Ultraviolet laser irradiation induced chemical reactions of some metal oxides.* **C. Sol and R. J. D. Tilley** 2001, J. Mater. Chem., Vol. 11, pp. 815, DOI: https://doi.org/10.1039/B006787N.

3. *Spectroscopic properties of molecules interacting with small dielectric particles.* **J. Gersten and A. Nitzan** 1981, J. Chem. Phys., Vol. 75, pp. 1139, DOI: https://doi.org/10.1063/1.442161.

4. *Enhanced Radiative Emission Rate and Quantum Efficiency in Coupled Silicon Nanocrystal-Nanostructured Gold Emitters.* **J. S. Biteen, D. Pacifici, N. S. Lewis and H. Atwater** 2005, Nano Letters, Vol. 5, pp. 1768, DOI: https://doi.org/10.1021/nl051207z.

5. *Twenty-fold plasmon-induced enhancement of radiative emission rate in silicon nanocrystals embedded in silicon dioxide.* **S. Gardelis, V. Gianneta and A. G. Nassiopoulou** 2016, J. Lumin., Vol. 170, pp. 282, DOI: https://doi.org/10.1016/j.jlumin.2015.10.029.

6. *Excimer laser ablation of thick SiO_x-films: Etch rate measurements and simulation of the ablation threshold.* **J. Ihlemann, J. Meinertz and G. Danev** 2012, Appl. Phys. Lett., Vol. 101, pp. 091901, DOI: https://doi.org/10.1063/1.4748127.

7. *Light-induced modification of a-SiO_x II: Laser crystallization.* **A. Janotta, Y. Dikce, M. Schmidt, C. Eisele, M. Stutzmann, M. Luysberg and L. Houben** 2004, J. Appl. Phys., Vol. 95, pp. 4060, DOI: https://doi.org/10.1063/1.1667008.

8. *Organic light-emitting device with an ordered monolayer of silica microspheres as a scattering medium.* **T. Yamasaki, K. Sumioka and T. Tsutsui** 2000, Appl. Phys. Lett., Vol. 76, pp. 1243, DOI: https://doi.org/10.1063/1.125997.

Acknowledgements

I would like to thank all the people without whom this dissertation would not have been possible. First and foremost, I would like to thank my group leader and supervisor Jürgen Ihlemann. He always spent time for my questions and discussions with me and gave helpful advice. I would also like to thank him for proofreading the manuscripts and the dissertation. I would also like to take this opportunity to thank my other colleagues. Jörg Meinertz always listened to my questions and helped me find solutions. I would also like to thank the group members Clemens Beckmann, Max Buczek, Laura Fütterer and Andreas Röben for their numerous helps. I was always able to find help from other colleagues outside our working group as well. For this, I would like to thank Hendrik Wrigge, Frederick Kleinwort, Till Schröder, Jens Oltmanns and Peter Simon in particular. Despite the quality of the food, the meals together in the canteen were always entertaining.

In addition to my colleagues, I would also like to thank my thesis advisory committee. In addition to Jürgen Ihlemann, I would also like to thank Prof. Hans Hofsäss and Prof. Michael Seibt for their support. I would like to thank Michael Seibt for proofreading the collaborative manuscript and Hans Hofsäss to be the second member of the examination committee.

Besides work, I would also like to thank my family. Without them, I would not be where I am today. Special thanks to my mother Cornelia, who has always supported me. Throughout my studies I was supported by my fiancée Isabel - for this I would like to thank her in particular and look forward to our future together.

Publications

First Author:

“Fabrication of Multilevel Fused Silica Diffractive Phase Elements by Laser Processing of Silicon Suboxide “; L. J. Richter, C. Beckmann, J. Meinertz and J. Ihlemann; DGaO-Proceedings A32 (2019)

https://www.dgao-proceedings.de/download/120/120_a32.pdf

“Laser Processing of Silicon Suboxide for the Fabrication of Multilevel Fused Silica Diffractive Phase Elements “; L. J. Richter, C. M. Beckmann and J. Meinertz, J. Ihlemann; Journal of Laser Micro/Nanoengineering 13, 249 (2018)

http://dx.doi.org/10.2961/jlmn.2018.03.0018

"Photoluminescence enhancement of silicon nanocrystals by excimer laser implanted gold nanoparticles"; L. J. Richter and J. Ihlemann; Applied Physics A 128, 764 (2022)

https://doi.org/10.1007/s00339-022-05906-1

"UV laser generated micro structured black surface on commercial TiO_2-containing glass"; L. J. Richter, C. M. Beckmann and J. Ihlemann; Applied Surface Science 601, 154231 (2022)

https://doi.org/10.1016/j.apsusc.2022.154231

“Excimer laser surface patterning for photoluminescence enhancement of silicon nanocrystals”; L. J. Richter, U. Ross, M. Seibt and J. Ihlemann; Currently under review (Not published); Photonics

Co-Author:

"Fabrication of periodic nanostructures on silicon suboxide films with plasmonic near-field ablation induced by low-fluence femtosecond laser pulses"; T. Takaya, G. Miyaji, I. Takahashi, L. J. Richter and J. Ihlemann; Nanomaterials **10**, 1495 (2020)

https://doi.org/10.3390/nano10081495

"Freeform shaping of fused silica substrates via viscous deformation induced by a laser patterned, stressed film"; C. M. Beckmann, L. J. Richter and J. Ihlemann; Optics Express **30**, 5 (2022)

https://doi.org/10.1364/OE.450282

"Glas marking by laser transfer implantation (LTI) of plasmonic nanoparticles"; J. Ihlemann, L. J. Richter, J. Meinertz, J. Wunderlich, N. Schindler, A. Günther, B. Oberleiter and T. Rainer; Optics & Laser Technology **155**, 108371 (2022)

https://doi.org/10.1016/j.optlastec.2022.108371

"Fast fabrication of diffractive patterns on glass by excimer laser ablation"; J. Meinertz, A. Gödecke, L. J. Richter and J. Ihlemann; Optics & Laser Technology **152**, 108148 (2022)

https://doi.org/10.1016/j.optlastec.2022.108148

"Improvement of optical transmittance of SiO_2 surface by femtosecond-laser-induced homogeneous nanostructure formation"; M. Edakubo, L. J. Richter, Y. Haraguchi, H. Aruga-Katori, J. Ihlemann and G. Miyaji; Optical Materials Express **12**, 10 (2022)

https://doi.org/10.1364/OME.470510

First-Author presentation on conferences:

“Laser processing of silicon suboxide for the fabrication of diffractive phase elements”; L. J. Richter, C. M. Beckmann and J. Ihlemann; DPG Erlangen 2018 Fachverband Kurzzeit- und angewandte Laserphysik, Erlangen, Germany (03/2018)

„Fabrication of Multilevel Fused Silica Diffractive Phase Elements by Laser Processing of Silicon Suboxide“; L. J. Richter, C. Beckmann, J. Meinertz and J. Ihlemann; 120. Jahrestagung der Deutschen Gesellschaft für angewandte Optik (DGaO), Darmstadt, Germany (06/2019)

"Laser-based methods for luminescence enhancement of Si-Nanocrystals by couplding to plasmonics nanoparticles"; L. J. Richter and J. Ihlemann; Applied Photonics, Bad Honnef Physics School, Bad Honnef, Germany (09/2021)

„Laser implantation of gold nanoparticles for photoluminescence enhancement of silicon nanocrystals”; L. J. Richter and J. Ihlemann; Conference on Laser Ablation (COLA 2021/2022), Matsue, Japan (04/2022)

“Laser implantation of plasmonic nanoparticles for photoluminescence enhancement of silicon quantum dots”; L. J. Richter and J. Ihlemann; SPIE Photonics West, San Francisco, United States (01/2023)

Co-Author presentation on conferences:

"Nanostructure formation on Silicon suboxide with plasmonic near-field ablation induced by femtosecond laser pulses"; T. Takaya, G. Miyaji, L. J. Richter and J. Ihlemann; 2019 Conference on Lasers and Electro-Optics Europe and European Quantum Electronics Conference; (06/2019)

“Nanostructure formation on Silicon suboxide with plasmonic nearfield ablation induced by femtosecond laser pulses”; T. Takaya, G. Miyaji, L.J. Richter and J. Ihlemann; CLEO Europe München (06/2019)

“Homogeneous nanostructures on SiO_2 formed with femtosecond laser pulses and improvement of optical transmittance”; M. Edakubo, Y. Haraguchi, H. A. Katori, G. Miyaji, L. J. Richter and J. Ihlemann; Conference on Laser Ablation (COLA 2021/2022), Matsue, Japan (04/2022)

Magazines articles:

"Quarzphasenmasken für Mikroskopie und Lasermaterialbearbeitung"; J. Meinertz, L. J. Richter, C. M. Beckmann and J. Ihlemann; Photonik 1.2020, p. 49

“Fused Silica Phase Masks Enhance Laser Processing and Microscopy”; J. Meinertz, L. J. Richter, C.M. Beckmann and J. Ihlemann; Photonic-Spectra 07/2021

https://www.photonics.com/Articles/Fused_Silica_Phase_Masks_Enhance_Laser_Processing/a67034

"Precision marking of glass with excimer lasers" - Laser generated microstructures and material modifications serve as colored marks – PhotonicsViews 02/2023, DOI: 10.1002/phvs.202300011

Patent application:

„Verfahren zum Versehen von Glas-Targets mit einer optisch wahrnehmbaren Markierung, Glaserzeugnis und Verwendung eines Titan-Silizium-Glases“; L. J. Richter, C. M. Beckmann, J. Ihlemann; Institut für Nanophotonik Göttingen e.V. (currently under review)